EXPLORING POTENTIAL ENERGY SURFACES AND REACTION MECHANISMS OF

INORGANIC MOLECULES BY COMPUTATIONAL METHODS

Except where reference is made to the work of others, the work described in this dissertation is my own or was done in collaboration with my advisory committee. This dissertation does not include proprietary or classified information.

_____
Hyun Joo

Certificate of Approval:

_____ _____
William E. Hill   Michael L. McKee, Chair
Professor   Professor
Chemistry and Biochemistry   Chemistry and Biochemistry

_____ _____
Thomas R. Webb   German Mills
Associate Professor   Associate Professor
Chemistry and Biochemistry   Chemistry and Biochemistry

_____
Stephen L. McFarland
Acting Dean
Graduate School

EXPLORING POTENTIAL ENERGY SURFACES AND REACTION MECHANISMS OF

INORGANIC MOLECULES BY COMPUTATIONAL METHODS

Hyun Joo

A Dissertation

Submitted to

the Graduate Faculty of

Auburn University

in Partial Fulfillment of the

Requirements for the

Degree of

Doctor of Philosophy

Auburn, Alabama
December 16, 2005

EXPLORING POTENTIAL ENERGY SURFACES AND REACTION MECHANISMS OF

INORGANIC MOLECULES BY COMPUTATIONAL METHODS

Hyun Joo

_____

Signature of Author

_____

Date of Graduation

VITA

Hyun Joo, the first son of Sucheon Joo (father) and Soonyoung Yoo (mother), was born on February 10, 1971 in Yeosu, South Korea. He received his early education in his hometown, graduated from Suncheon high school and then went to college in Seoul. After graduating from Hanyang University with a B.S. in Chemistry, he entered the graduate program in the same University and obtained an M.S. degree in inorganic chemistry in February 1999. After graduation, he worked as a research scientist in Molecular Simulation Institute at Soongsil University for one year and then at Hanyang University until July 2001. In August 2001, he joined Dr. Michael L. McKee's research group at Auburn University and conducted research on potential energy surfaces and reaction mechanisms of inorganic and organic molecules. At Auburn, he met Geum Jhun Martha Lee, daughter of Young Ik Lee and Ok Hee Kim, and married on December 28, 2002. In October 2004, they had a son, Michael Lee Joo.

DISSERTATION ABSTRACT

EXPLORING POTENTIAL ENERGY SURFACES AND REACTION MECHANISMS OF

INORGANIC MOLECULES BY COMPUTATIONAL METHODS

Hyun Joo

Doctor of Philosophy, December 16, 2005
(M.S. Hanyang University-Seoul, Korea, 1999)
(B.S. Hanyang University-Seoul, Korea, 1997)

169 Typed Pages

Directed by Michael L. McKee

Various computational methods have been applied in order to explore potential energy surfaces (PES) and reaction mechanisms.   Theoretical background and computational methods are introduced in chapter 1. Chapters 2-5 report four different studies exploring potential energy surfaces of inorganic and organic molecules in order to understand reaction mechanisms.

Chapter 2 reports an investigation of the singlet and triplet potential energy surfaces of BCP isomers. From constructed PES, intramolecular rearrangment mechanisms are studied, possible dissociation pathways are discussed, a conical intersection is located, and Renner-Teller species are investigated.

Chapter 3 reports the dissociation mechanism of phosphorus-containing hyponitrites at the B3LYP level. The cis-hyponitrite, $XON=NOX$ ($X=PF_2$, OPF_2), is predicted to concertedly

decompose to N_2 plus phosphorus-containing radicals or to N_2O plus the μ-oxo phosphorus species. The *trans*-hyponitrite can only decompose to N_2 plus the phosphorus-containing radicals because there is a very high barrier for rearrangement to *cis*-hyponitrite. However, the silver cation is predicted to reverse the order of the two transition states through stronger interactions with the oxygen atoms in the transition state of the N_2O-producing pathway.

Chapter 4 explains the reactions mechanism of "stable" bis(amino)silylene with halomethanes and reports that the reactions occur via a radical mechanism. To explain the discrepancy of the theoretical model chemistry with experimental observations, substituent effects on the nitrogen atoms and halogen effects on the halomethanes are investigated which explain experimental observations.

In Chapter 5, the reaction of atomic carbon with formaldehyde is reported. The possible singlet excited carbene ($^1B_1$) formation pathways are investigated by analyzing the singlet and triplet potential energy surfaces of ketene. The production of $^1B_1$ methylene from deoxygenation by ^1D carbon and potential energy surface crossing along the C-C and C-O bond stretching are considered.

ACKNOWLEDGMENTS

I would like to express my most sincere gratitude to Dr. Michael L. McKee for his guidance and encouragement over four years. He has been more than a mentor for his generosity, patience, help and understanding toward me during my graduate life in Auburn.

I am deeply indebted to all my committee (Dr. Hill, Dr. Mills, and Dr. Webb) for their careful examination, helpful comments and advice on the dissertation. I am deeply grateful to Dr. Philip B. Shevlin for his guidance and mentorship. I would like to thank all the faculty of the Department of Chemistry and Biochemistry for their hospitality and encouragement on my graduate study.

I would also like to thank Dr. Nida McKee for her help and generosity through my living in Auburn. Sincere appreciation is extended to Dr. Younghi Kwon for his help and encouragement, and to Nick, Lauren, Tyler, and Ohyun Kwon for their friendship and sharing valuable time in Auburn. All my friends, whom I cannot mention one by one, would be given my appreciation from my heart.

Special great thanks are expressed to my mother who provided me with generous support and endless love through my life, and to my sisters and brother for their support. I also express sincere appreciation to my parents-in-law, and sister-in-law for their support and encouragement. Finally, I would like to dedicate this dissertation to my beloved wife, who supports me most to meet this challenge, and to my son who has given me the greatest pleasure and hope in my life.

Style manual or journal manual used: <u>Journal of the American Chemical Society</u>

Computer software used: <u>Mac-MS word 2001, CS ChemDraw Std. 7.0 for Mac</u>

TABLE OF CONTENTS

LIST OF FIGURES

CHAPTER 5

LIST OF TABLES

CHAPTER 3

CHAPTER 4

CHAPTER 1

GENERAL INTRODUCTION

The concept of a potential energy surface (PES) comes from the Born-Oppenheimer approximation which states that the motion of electrons is much faster than that of nuclei and that those motions can be separated.[1-3] We can think of the electrons as being subject to the electrostatic field of the stationary nuclei. The electronic wave function is obtained by solving the Schrödinger equation for a given nuclear configuration. On the other hand, the nuclei are subject to a potential which is the sum of the nuclear repulsion and the average field due to the electrons. The wave function for the nuclei is thus obtained by solving a Schrödinger equation in which the nuclei are subject to a potential which is the sum of the electronic energy and electrostatic potential of the nuclei. This potential, which is a function of the nuclear geometry, is called the potential energy function or potential energy surface for nuclear motion. For a non-linear (linear) molecule containing N atoms, the potential energy function is a function of 3N-6 (3N-5) variables. Such functions cannot be represented graphically except for diatomic molecules. It is possible to portray the potential energy function for a polyatomic molecule only by constraining some of the variables. Because the potential energy function for a polyatomic molecule cannot be fully represented graphically, it is often referred to as a potential energy hypersurface.

The potential energy surface plays a central role in our understanding of the dynamics of chemical reactions. For example, the activation barrier can be understood in terms of the variation of potential energy along the reaction coordinate, and the dynamics of a chemical

reaction can be understood fully only in terms of motion of the nuclei on a potential energy surface. Any theoretical treatment of the dynamics, whether classical, semi-classical or quantum, requires some form of potential energy surface. A potential energy surface can be obtained experimentally from vibrational-rotational spectroscopy or theoretically from quantum mechanical calculations. It is extremely difficult to derive information about the potential energy surface for a polyatomic molecule where the potential is not a curve but a multidimensional surface. Therefore, quantum mechanical calculations are generally applied to obtain the potential energy surface of molecules.

Due to the rapid development of computer technology, computational chemistry has been one of the fastest growing fields of chemistry. Computational chemistry provides reliable information to help chemists not only analyze and interpret experimental data but also predict chemical and physical properties of molecules and design new molecules. The goal of this dissertation is to explore the potential energy surface of molecules and to explain reaction mechanisms by using various computational methods. This chapter presents the theoretical background and features of the potential energy surface and quantum mechanical methods which have been utilized in the study for this dissertation.

1.1 The Born-Oppenheimer approximation and potential energy surface

If one could solve the Schrödinger equation for a molecule, one would be able to obtain all the information about the molecule consistent with the postulates of quantum mechanics. However, the Schrödinger equation can be solved exactly for only a limited number of simple systems and the use of quantum mechanics to obtain a description of a molecule is based on a number of approximations. One of the most important approximations related to application of quantum mechanics to molecules is the Born-Oppenheimer approximation.[1-3] The basic idea behind this approximation is that the movements of electrons and nuclei are on different time

scales. Thus we expect the electrons to be able to move much faster than nuclei. This allows us to solve the Schrödinger equation by separating the motion of electrons from that of nuclei. The mathematical description of this separation follows.

The time-independent Schrödinger equation for the motion of the electrons and the nuclei in a molecule is of the form

$$[\hat{T}_{nuc}(R) + \hat{T}_{el}(r) + V_{nn}(R) + V_{ne}(R,r) + V_{ee}(r)]\Psi(R,r) = E\Psi(R,r). \tag{1}$$

$\hat{T}_{nuc}(R)$ is the kinetic energy operator for the nuclei at positions R, $\hat{T}_{el}(r)$ is the kinetic energy operator for the electrons at positions r, $V_{nn}(R)$ is the electrostatic potential energy of the nuclei, $V_{ne}(R,r)$ is the potential energy of the electrons in the field of the nuclei and $V_{ee}(r)$ is the inter-electron repulsion. Nuclei are much heavier than electrons and thus nuclear motion is very slow compared with electronic motion and a reasonable approximation is to separate the two types of motion. This is the Born-Oppenheimer separation in which the total wavefunction $\Psi(R,r)$ is written as the product of an electronic wave function $\Phi(R,r)$ and a nuclear wave function $\chi(R)$:

$$\Psi(R,r) = \Phi(R,r)\chi(R). \tag{2}$$

$$[\hat{T}_{nuc}(R) + \hat{T}_{el}(r) + V_{nn}(R) + V_{ne}(R,r) + V_{ee}(r)]\Phi(R,r)\chi(R) = E\Phi(R,r)\chi(R) \tag{3}$$

The electronic wavefunction $\Phi(R,r)$ is the solution to the electronic Schrödinger equation,

$$[\hat{T}_{el}(r) + V_{ne}(R,r) + V_{ee}(r)]\Phi(R,r) = W(R)\Phi(R,r), \tag{4}$$

with eigenvalue $W(R)$ which is the electronic energy depending on the nuclear coordinates R.

The rest of the Schrödinger equation can be written as

$$[\hat{T}_{nuc}(R) + V_{nn}(R) + W(R)]\Phi(R,r)\chi(R) = E\Phi(R,r)\chi(R). \tag{5}$$

The nuclear kinetic energy operator is of the form of

$$\hat{T}_{nuc}(R) = -\frac{h^2}{8\pi^2}\sum_k \frac{1}{M_k}\nabla_k^2 \tag{6}$$

where the summation k runs over the nuclei of mass M_k. Thus

$$\hat{T}_{nuc}(R)\Phi(R,r)\chi(R) = \Phi(R,r)\left[-\frac{h^2}{8\pi^2}\sum_k\frac{1}{M_k}\nabla_k^2\chi(R)\right]$$

$$+\chi(R)\left[-\frac{h^2}{8\pi^2}\sum_k\frac{1}{M_k}\nabla_k^2\Phi(R,r)\right] \tag{7}$$

$$-\frac{h^2}{8\pi^2}\sum_k\frac{2}{M_k}\{\nabla_k\Phi(R,r)\}\{\nabla_k\chi(R)\}$$

In equation (7), the second and third terms can be shown to be negligible. For example, in the second term, $\nabla_k^2\Phi(R,r)$ is a second order derivative of the electronic wave function with respect to the nuclear coordinates and will be of the same order of magnitude as the derivative with respect to electronic coordinates $\nabla_i^2\Phi(R,r)$. However $\frac{h^2}{8\pi^2 m}\nabla^2\Phi(R,r)$ is of the same order of magnitude as the energy of one of the electrons. The second term in equation (7) is thus of the order of m/M_k where m is mass of an electron and can be neglected. Similarly, the third term can be neglected. Therefore,

$$\hat{T}_{nuc}(R)\Phi(R,r)\chi(R) \approx \Phi(R,r)\hat{T}_{nuc}(R)\chi(R) \tag{8}$$

and finally we can rewrite equtation (5) as

$$[\hat{T}_{nuc}(R)+V_{nn}(R)+W(R)]\chi(R) = E\chi(R). \tag{9}$$

which is called the nuclear Schrödinger equation. The sum of two terms $U(R)=V_{nn}(R)+W(R)$ in equation (9) is known as the potential energy function or potential energy surface.

1.2 Potential energy surface crossing and non-crossing rule

When computing multiple potential energy surfaces for a system, it is possible to have points where two potential energy surfaces $U(R)$ have the same energy. What happens at this point is of great interest to chemists and will be discussed in this section. The non-crossing rule was put forward by Hund[4] and formulated by von Neumann and Wigner.[5] It states that in a

diatomic molecule for an infinitely slow change of internuclear distance, potential energy curves corresponding to electronic states of the same symmetry cannot cross. When two wave functions are mixed to form a better wave function, the new energies repel each other. As two potential energy surfaces come close together along the reaction coordinate, the two wave functions are mixed and they split apart. The point of nearest approach is called an avoided crossing point.

The avoided crossing points arise because the adiabatic electronic states around the avoided crossing point are often mixtures of molecular orbitals of two states. The mixing of the two molecular orbitals causes two states to repel each other and results in separation of two states. A surface where the actual intersections are substituted for the avoided crossing is called a diabatic surface. If the nuclei are assumed to move slowly, then they are likely to follow a single adiabatic surface. If the nuclei have sufficient velocity, however, then the Born-Oppenheimer approximation breaks down and the nuclei may effectively ignore the gap in the avoided crossing and simply cross over to the other adiabatic surface, adopting that configuration. This is termed non-adiabatic behavior. However two potential energy surfaces can cross if their symmetries are sufficiently different. Hund wrote that if two potential energy surfaces cross, the electronic state must be degenerate at the crossing point.[4]

1.3 Conical intersection

Conical intersections occur when two surfaces cross. At the point of intersection the two surfaces are degenerate, and it is at this point that a molecule can cross from one electronic state to another. Until recently conical intersections were thought to be very rare. However over the last 10 years, it has been established that conical intersections are ubiquitous.[6,7] In fact, many photochemical reactions have been shown to involve conical intersections.[7] A conical intersection is called "conical" because in a reduced space called the "branching space" the equations for the two surfaces look like the geometric equations for a cone. The branching space

is just two special normal modes from the total of 3N-6 (3N-5) allowed to a non-linear (linear) molecule. The branching space modes are special in that they break the degeneracy of the two intersecting surfaces, while in all other modes this degeneracy remains. Near a conical intersection we say that the two surfaces couple or mix and at a conical intersection the geometric change leads to a sign change of the adiabatic electronic wavefunction.[8] Although we can draw nice smooth lines, it is implicit that more complicated things are happening. This coupling of states about a conical intersection is highly quantum mechanical. The coupling of electronic surfaces at a conical intersection is facilitated by the interaction of the nuclei and electrons. This system is said to be non-adiabatic, and the breakdown of Born-Oppenheimer approximation at the conical intersection makes describing conical intersections very difficult. A Jahn-Teller (JT) effect is a special case of conical intersection. The Jahn-Teller theorem[9] states that "the nuclear configuration of non-linear polyatomic system in a degenerate electronic state is unstable with respect to nuclear displacements that lower the symmetry and remove the degeneracy". In other words, there is always at least one non-totally symmetric
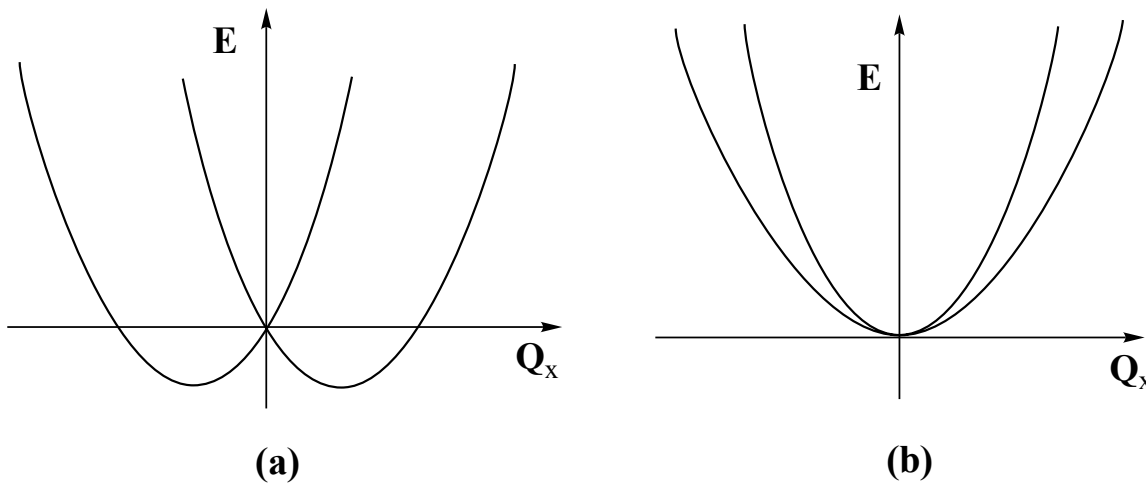
Figure 1.   (a) One-dimensional potential energy curves showing linear Jahn-Teller distortion. (b) Renner-Teller (Type A) potential energy surface curves. Both are adapted form reference 6(b).

normal coordinate for which the splitting results in two or more separate potential minima for non-zero values of the normal coordinate. It can be seen that for Q = 0 the two potential curves cross at a non-zero angle as illustrated in Figure 1 (a). This phenomenon is well known in transition metal chemistry where an octahedral structure for an ion containing, for example, nine d-electrons would have the electronically degenerate configuration $t_{2g}^6 e_g^3$. Because of the Jahn-Teller effect there will be a structure of lower symmetry which can be obtained by distorting the regular octahedral structure along one of the normal coordinates. When a molecule has a pseudo-degenerate electronic state, provided only that the difference in their energies is lower than the vibronic stabilization energy, a similar effect, called pseudo-Jahn-Teller effect, occurs. The pseudo-Jahn-Teller effect (PJT)[10] is the distortion of a high symmetry non-degenerate species to a lower symmetry geometry along a single non-totally symmetric vibrational coordinate. An energy stabilization occurs due to a mixing of the ground and excited states along this vibrational coordinate and the excited state energy increases. Geometries subject to the pseudo-Jahn-Teller distortion are saddle points on the adiabatic potential energy surface.

A linear molecule with a degenerate electronic state is subject to a distinct distortion termed the Renner-Teller effect.[11] The degeneracy of such electronic states is two-fold, but along the bending modes the degeneracy of electronic states is removed and the potential curve splits into two curves as shown in Figure 1 (b). However, in a Renner-Teller active molecule the degeneracy of electronic states is not lifted to first order in nuclear displacements, and there is no conical intersection. Rather, there is a 'glancing' or 'touching' of the two surfaces. Herzberg suggested that Renner-Teller geometries should be referred to as 'glancing intersections'.[6(b),11(b)] Although a Renner-Teller geometry is not a conical intersection, it provides useful information about the frequency analysis of the intersection space at a conical intersection. Renner-Teller species are stationary points so that they can be optimized and characterized using standard analytical derivative techniques. Five distinct types of Renner-Teller potential energy surfaces

classified by Schaefer[12] are given below.

(A) The total energies of both electronic components of a degenerate state increase as the molecule is bent, and the harmonic bending frequencies (no imaginary frequencies) for the two states are different.

(B) Same as A except that the two bending frequencies are identical. Thus larger displacement from linearity is required to distinguish two curves than type A.

(C) One potential curve is attractive and the other is repulsive with respect to the bending coordinate (one imaginary frequency).

(D) Both curves are attractive (2 imaginary frequencies), but there are two distinct harmonic bending frequencies.

(E) Same as type D, but the two harmonic bending frequencies are identical.

1.4 Molecular Orbital (MO) Theory

Molecular orbital theory[13] is another approximation in quantum mechanics which is based on an independent-particle model for the molecular electronic wavefunction. A form of wavefunction can be chosen which would be appropriate if we could ignore the interelectronic repulsion. If this were the case then the electronic Schrödinger equation for n electrons would be separable into a set of n one-electron Schrödinger equations which could be solved to obtain a set of one electron functions which is often called spin orbitals $\phi_i(r)$, where $i=1,2,,\ldots,n$.

$$\Phi(R,r) = \phi_1(r_1)\phi_2(r_2)\cdots\phi_n(r_n) \tag{10}$$

Each spin orbital can be written as the product of a spatial function $\psi_i(r_i)$, which depends on the coordinates r_i of electron i, and a spin function α or β, depending on whether the spin is up or down. This product is called a Hartree product. Each spatial function can hold two electrons: one with α-spin and one with β-spin. Assuming a closed-shell system where all spatial functions are doubly occupied, we can rewrite the electronic wavefunction $\Phi(R,r)$ as

$$\Phi(R,r) = \psi_1(r_1)\alpha\psi_1(r_2)\beta\psi_2(r_3)\alpha\cdots\psi_{n/2}(r_{n-1})\alpha\psi_{n/2}(r_n)\beta \tag{11}$$

However, it is necessary to take into account the indistinguishability of the electrons by recognizing that we can permute the electron labels among the orbitals. At the same time we have to ensure that the wave function satisfies the Pauli principle by being antisymmetric with respect to the interchange of two electrons by taking the appropriate linear combination of all permutations. To satisfy both requirements, the electronic wavefunction (9) can be written in a determinantal form called a Slater determinant.

$$\Phi(R,r) = \frac{1}{\sqrt{n!}}\begin{vmatrix} \psi_1(r_1)\alpha & \psi_1(r_1)\beta & \cdots & \psi_{n/2}(r_n)\beta \\ \psi_1(r_2)\alpha & \psi_1(r_2)\beta & \cdots & \psi_{n/2}(r_2)\beta \\ \vdots & \vdots & \vdots & \vdots \\ \psi_1(r_n)\alpha & \psi_1(r_n)\beta & \cdots & \psi_{n/2}(r_n)\beta \end{vmatrix} \tag{12}$$

An interchange of two electrons is equivalent to interchanging the labels for the electronic coordinates r_i with r_j resulting in the swapping the rows corresponding to r_i and r_j. This results in a change of sign, as required by the Pauli principle. The Slater determinant is sometimes represented by more compact notation

$$\Phi = |\psi_1\alpha\psi_1\beta\psi_2\alpha\psi_2\beta\cdots\psi_{n/2}\alpha\psi_{n/2}\beta|. \tag{13}$$

Spin orbitals spread throughout the molecule, and their exact form is determined by the variational principle, which states that any approximate wave function has an energy above or equal to the exact energy. The variational theorem allows us to calculate an upper limit for the system's ground state energy. Consequently, the better the wavefunction, the lower the energy and the best wavefunction is obtained when the energy is lowest.

1.5 Hartree-Fock (HF) method

The Hartree-Fock approximation[4] is equivalent to the MO approximation in quantum chemistry. It is based on a simple approximation of the true many-electron wave function which is given by a single Slater determinant of spin orbitals. In the HF model, the electronic

Hamiltonian operator is replaced with an effective one-electron operator called the Fock operator. The HF molecular orbitals are eigenfunctions of the Fock operator, the eigenvalues being the orbital energies. The HF model takes into account electronic interactions only as an average effect of repulsion (central field approximation) but not the explicit electron-electron interaction. The HF model is the simplest method to use for chemical applications. Although the HF method is insufficient for accurate modeling due to the incomplete description of electron correlation, it plays a central role in quantum chemistry. The HF method provides a starting point for more accurate approximations which include electron correlations.

For molecular calculations, numerical integration of the HF equations proves impossible, and Roothaan introduced a linear combination of atomic orbital (LCAO) version of the self consistent field (SCF) theory.[14] The Roothaan-Hall equations are the Fock equations in the atomic orbital basis, and all the equations may be collected in a matrix notation.[13] The Roothaan-Hall equations must be solved iteratively since the Fock matrix depends on its own solutions. First, all one- and two-electron integrals are calculated and followed by generation of a suitable starting guess for the MO coefficients. Next, the initial density matrix is formed and then the formations of the Fock matrix, the core intergrals and the density matrix times two-electron integrals follow. In the next step, the Fock matrix is diagonalized where the eigenvectors contain the new MO coefficients. Finally the new density matrix is formed and if it is sufficiently close to the previous density matrix, then the self-consistency is achieved. If not, a new Fock matrix is formed and the same procedure is repeated until the density matrix converges.

The main deficiency of the HF model is its incomplete description of the correlation among electrons. Due to the neglect of electron correlation, even with a complete basis set, the HF method cannot give an exact solution. This is called the HF limit. In order to include electron correlation into HF calculations, post-HF methods for correction of electron correlations are introduced. Those methods will be discussed briefly in the electron correlation methods part.

10

1.6 Basis sets

A basis set[13,15] is the set of mathematical functions from which the wave function is constructed to describe the shape of the orbitals in an atom. In the practical quantum mechanical calculations, the molecular orbitals are expressed as linear combinations of a predefined set of one-electron wave functions known as basis functions.

An individual molecular orbital can be written as:

$$\psi_i = \sum_{\mu=1}^{N} c_{\mu i} \phi_\mu \tag{14}$$

where the coefficients $c_{\mu i}$ are known as the molecular orbital expansion coefficients. These coefficients provide the orbital description with some flexibility, and can be determined so that the electronic energy calculated from the molecular orbital ψ_i is minimized and is as close as possible to the energy corresponding to the exact solution of the Schrödinger equation by the variational principle. There are two types of basis functions commonly used in quantum mechanics calculations: Slater-type orbitals (STO) and Gaussian-type orbitals (GTO).[13,15] The STOs have the functional form:

$$\phi_{\varsigma,n,l,m}(r,\theta,\varphi) = N Y_{l,m}(\theta,\varphi) r^{n-1} e^{-\varsigma r} \tag{15}$$

where N is a normalization constant and $Y_{l,m}$ are the typical spherical harmonic functions. The parameter ζ is the orbital exponent determining the size of the orbitals. STOs provide reasonable representations of atomic orbitals with standard ζ values suggested by Slater.[16] A major deficiency of STOs is that they do not have radial nodes and hence are not mutually orthogonal. Also, they are not appropriate for numerical computations of multi-centered integrals while solving the Schrödinger equation due to the high cost in computer time, and their practical use in quantum-mechanical calculations is now limited. Most quantum mechanics programs use GTOs as basis functions, and the general form is:

$$\phi_{\varsigma,n,l,m}(r,\theta,\varphi) = N\, x^l y^m z^n e^{-\varsigma r^2} \tag{16}$$

where the sum of l, m, and n determines the type of orbital. The dependence of r^2 in the exponential makes GTOs inferior to STOs in two aspects: First, a GTO has zero slope at the nucleus while a STO has a cusp. The result is that GTOs have difficulty in describing the proper behavior near the nucleus. Secondly, GTOs fall off too rapidly far from the nucleus compared to STOs, and the whole wave function is consequently represented poorly, which indicates that more GTOs are required for achieving a certain accuracy compared to STOs. Nevertheless, GTOs have the important advantage over STOs that a GTO integral evaluation takes much less computer time. Therefore, GTOs are preferred and are generally used in computational calculations.

Most semiempirical methods use a predefined basis set from STOs. In ab initio and density functional theory calculations, basis sets are used in the form of linear combinations of GTOs. Although it is possible to create a basis set from basis functions in an arbitrary way, most calculations are done using existing basis sets which are already defined. Choosing a basis set significantly influences the accuracy of the calculation as much as the level of the theoretical method. The choice of a basis set also has a large effect on the computing cost. Generally, the cost of molecular calculations increases greatly with the number of functions in the basis set, N^4 for the integral computation and N^4-N^7 for the solution of the Schrödinger equation where N is the number of basis functions.[17] Use of disk storage for HF calculations scales as N^4 and the amount of memory required scales as N^2 for most program algorithms.[17] There are a lot of well-known basis sets available in the literature or built into computational programs. These basis sets are identified by one of a number of notation schemes. Some of the commonly available basis sets are introduced and described in the following section.

When a basis function is defined as a linear combination of Gaussians, it is referred as a contracted basis function, and the individual Gaussians are called primitive Gaussians. Thus, in a

basis set of contracted GTOs, each basis function is defined by the contraction coefficients and exponents of each primitive. The degree of contraction refers to the total number of primitives used to make all of the contracted functions. A contracted basis set is denoted with (primitives functions)/[contracted functions]. For example, (6s3p/3s)/[2s1p/1s] denote that 3 each of 1s primitives, 2s primitives and 2p primitives giving a total of 6s and 3p primitives are contracted to create single 1s, 2s, and 2p sets so that the contracted functions are 2s1p for first row atoms while for hydrogen 3s primitives are contracted to create a 1s function.

The smallest number of basis functions is called a minimal (or minimum) basis set,[13,15] which consists of one atomic basis function for each inner shell and valence shell atomic orbital (AO) of each atom. The most popular minimal basis set is called STO-3G which would be (6s3p/3s)/[2s1p/1s] in contracted basis set notation. Minimal basis sets are used for very large molecules in order to obtain qualitative results. Several methods exist so that the basis set can be made larger than a minimal basis set in order to get better descriptions of energies and geometries. The Dunning-Huzinaga basis set is one popular basis set. The double-zeta (DZ) basis sets[13,15,18] describe all molecular orbitals by using two sets of basis functions with different orbital exponents (ζ) for each core and valence orbital. A triple-zeta (TZ) basis set replaces each basis function of a minimal basis set by three sets of basis functions, each with a different orbital exponent.

Pople and co-workers[13,15,18] designed split-valence (SV) basis sets which use two or more basis functions for each valence shell AO and but only one basis function for each core shell AO. Split-valence sets are called valence double-zeta (VDZ) and valence triple-zeta (VTZ) according to the number of basis functions used for each valence AO. For instance, 3-21G and 6-31G basis sets have two sets of basis function for each valence AO, and a 6-311G basis set uses three sets of basis functions for each valence AO. In Pople-style basis sets, each basis function is expressed as a linear combination of primitive Gaussians rather than represented by a single primitive

Gaussian. For the 3-21G basis set, each core AO is represented by a basis function which is a linear combination of three primitive Gaussians , while each valence AO use two sets of basis functions, one of which is a contraction of two GTOs and the other of which is a single GTO that is (6s3p/3s)/[3s2p/2s] for first row elements. The 6-31G basis set uses six GTOs in each core AO's basis function and represent each valence AO by one basis function with three GTOs and one basis function with one GTO, which is (10s4p/4s)/[3s2p/2s] for first row elements. The number of basis functions for 3-21G and 6-31G basis sets are the same, but the 6-31G basis set has more GTOs than 3-21G. Therefore, the 6-31G basis set describes molecular properties better than the 3-21G basis set.

Split-valence basis sets allow orbitals to change size in the radial part, but not to change the shape of orbitals. Molecular orbitals are often distorted in shape and have their centers of charge shifted depending on molecular formation. By adding polarization functions such as *d*- and *f*-type functions to SV basis sets, the shape of AOs can vary, thereby shifting charge density away from the nuclei and into the bonding regions in the molecule.[13,15] For example, the 6-31G(d) basis set is a VDZ polarized basis set which adds six *d*-type functions to the 6-31G basis set on each of the atoms other than hydrogen. The 6-31G(d,p) basis set adds three *p*-type functions to the 6-31G(d) basis set on each hydrogen. The 6-31G(d) and 6-31G(d,p) basis sets are often denoted as 6-31G* and 6-31G**, respectively. These polarized basis sets are generally used because they often result in more accurate computed geometries and vibrational frequencies.[17,18]

Anions, molecules having electron lone pairs, and hydrogen-bonded complexes have significant electron density at large distances from the nuclei. To improve the accuracy of describing these problems, diffuse functions, *s*- and *p*-type functions with small orbital exponents, can be added.[13,15] The 6-31+G* basis set is formed from the 6-31G* basis set by adding four diffuse functions (s, p_x, p_y, p_z) on each non-hydrogen atom. The 6-31++G* set also

includes one diffuse *s*-type function on each hydrogen atom. However, diffuse functions on

hydrogen atoms do not usually increase the accuracy of a calculation. Nowadays, larger basis

sets including multiple polarization and diffuse functions are practical for many systems due to

the increased speed of computers and program algorithms. The largest Pople-style basis set is

6-311++G(3df,3pd) which is a triple split-valence with additional diffuse *s*- and *p*-type functions

and three sets of *d*-type functions and one set of *f*-type functions on heavy atoms and one diffuse

s-type function and three sets of *p*-type functions and one set of *d*-type functions on hydrogen

atoms. Such basis sets are useful for describing interactions between electrons using methods

that include electron correlation.

   The Pople and Dunning-Huzinaga basis sets are of the segmented-contraction type since

the primitives are partitioned into disjointed or almost disjointed sets.[19] Modern contracted basis

sets aimed at producing very accurate wave functions often employ a general contraction scheme.

The atomic natural orbital (ANO) and correlation-consistent (*cc*) basis sets are of the general

contraction type. ANO basis functions are obtained from the atomic natural orbitals obtained

from valence CISD calculations on the free atoms. The natural orbitals are obtained as the

eigenvectors of the first-order density matrix and their associated eigenvalues are referred to as

the orbital occupation numbers. The ANO contraction selects the important combinations of the

primitive GTOs from the magnitude of the occupation numbers. A large primitive basis may

generate several different contracted basis sets by gradually lowering the selection threshold for

the occupation number. The nice feature of the ANO contraction is that it automatically

generates balanced basis sets. Furthermore, in such a sequence the smaller ANO basis sets are

true subsets of the larger, since the same primitive set of functions is used. The primary

disadvantage of the ANO basis set is that there is a very large number of primitive GTOs.

Dunning's correlation consistent (*cc*) basis set is smaller than the ANO basis set but yields results

comparable to those of the ANO basis sets.[18,19] The name correlation consistent refers to the fact

that the basis sets are designed so that functions which contribute similar amounts of correlation energy are included at the same stage, independently of the function type. Several different sizes of cc basis sets are available. These are known by their acronyms: *cc-p*VDZ, *cc-p*VTZ, *cc-pVQZ*, *cc-p*V5Z and *cc-p*V6Z (*correlation-consistent polarized* Valence Double/Triple/Quadruple/Quintuple/Sextuple Zeta).

Basis set requirements for atoms beyond the third row of the periodic table are different from the elements with lower atomic number. For heavier metals, relativistic effects become important and core electrons must be treated differently from valence electrons. The effective core potential (ECP)[20,21] can be used to handle the core electrons of these heavier atoms effectively. The ECPs and associated basis sets of Hay-Wadt,[22] Stevens and co-workers,[23] and Stuttgart-Dresden ECP[24] are widely used and already implemented in many computational chemistry packages. The main advantage of using ECPs plus valence basis sets rather than all-electron basis sets is that the former consider relativistic effects effectively and require less computer time.

Commonly used basis sets for quantum mechanics program and literature references for them are available on the web site of the EMSL Gaussian Basis Set Order Form (http://www.emsl.pnl.gov/forms/basisform.html) at the Environmental Molecular Sciences laboratory of the Pacific Northwest laboratory.

1.7 Electron correlation methods

Since the HF method does not include a full consideration of electron correlation, many theoretical methods have been developed in order to consider electron correlation properly. There are two kinds of electron correlations. One is dynamic correlation which is mainly caused by the instantaneous repulsion of the electrons. In the HF scheme, electrons often get too close to each other, because the electrostatic interaction is treated in only an average manner. As a

consequence, the electron-electron repulsion term is too large resulting in higher energy. It is called dynamic electron correlation because it is related to the actual movements of the individual electron and is known to be a short-range effect. This dynamic correlation can be treated by perturbation theory,[13,15] coupled cluster (CC) theory,[13,15,25] and density functional theory (DFT).[26] The other is non-dynamical or static correlation. It is related to the fact that in certain circumstances a single Slater determinant is not a good approximation to the true ground state, because there are other Slater determinants with comparable energies. Two computational methods are available to treat non-dynamical correlation. Using a single Slater determinant, non-dynamic correlation can be treated by increasing the order of electronic excitations incorporated in dynamic correlation methods such as coupled cluster (CC) theory and configuration interaction (CI).[13,15] Non-dynamic correlation can be also corrected by the multi-configuration self-consistent field (MCSCF) method[27] via multi-configuration determinants. Generally, electron correlation methods are also referred as post-HF methods since the correlation correction terms are added to the basic HF methods in them.

Möller-Plesset (MP) perturbation theory is one of the most economical electron correlation methods.[15] MP methods treat the Hamiltonian operator as:

$$\boldsymbol{H} = \boldsymbol{H}_0 + \lambda \boldsymbol{V} \tag{17}$$

where $\boldsymbol{H}_0$ is the HF Hamiltonian and $\lambda \boldsymbol{V}$ is a perturbation applied to $\boldsymbol{H}_0$. The Rayleigh-Schrödinger perturbation theory[5] provides a description of the perturbed system as:

$$\boldsymbol{H}\Psi = (\boldsymbol{H}_0 + \lambda \boldsymbol{V})\Psi = E\Psi. \tag{18}$$

Here, wave function and energy obtained from eq. (18) can be expanded in powers of λ.

$$\Psi_\lambda = \Psi^{(0)} + \lambda^1 \Psi^{(1)} + \lambda^2 \Psi^{(2)} + \cdots \tag{19}$$

$$E_\lambda = E^{(0)} + \lambda^1 E^{(1)} + \lambda^2 E^{(2)} + \cdots \tag{20}$$

Practical MP methods may be formulated by truncating the series in eq. (19) and (20) to various orders. MP2 (truncation after 2nd-order), MP3, and MP4 are well known. The MP energy

correct to first-order (MP1) is the HF energy. MP2, MP3, and MP4 provide size extensive

energy correction systematically. The simplest approximation to the electron correlation is the

MP2 method. In practice, MP2 is the most popular among truncated MP methods due to the

reasonable computational cost with acceptable results.[17] Higher orders of MP methods such as

MP3 and MP4 are available in case MP2 is inadequate. However, MP4 is more often used

compared to MP3 because MP3 calculations are known to provide little improvement over MP2

results.[17,18]

If a single Slater determinant contains substantial multi-reference character (i.e. biradical

species), MP methods often produce absurd results. In order to correct this problem, the

multi-configuration self-consistent field (MCSCF) method[27] can be applied. MCSCF

calculations employ the molecular wave function as linear combinations of single Slater

determinants which is called configuration state function (CSF) and not only vary the expansion

coefficients but also optimize the forms of the molecular orbitals. The major problem with

MCSCF methods is selecting the necessary configurations. One of the most popular approaches

is the complete active space self-consistent field (CASSCF)[27] method which is also called full

optimized reaction space (FORS). The selection of configurations is done by partitioning the

MOs into active and inactive space. The active MOs will typically be some of the highest

occupied and some of the lowest unoccupied MOs. Within the active MOs a full CI is

performed. A common notation is CASSCF(n,m), indicating that n electrons are distributed over

m orbitals. CASSCF calculations provide a reasonable treatment of non-dynamic electron

correlation and some of dynamic correlation. The more configurations are included, the more

dynamic correlations are included. In general the number of singlet CSFs formed from the (n,m)

active space is determined by eq. (21).[28]

$$N = \frac{m!(m+1)!}{\left(\dfrac{n}{2}\right)\left(\dfrac{n}{2}+1\right)\left(m-\dfrac{n}{2}\right)\left(m-\dfrac{n}{2}+1\right)} \tag{21}$$

Therefore a high computational cost is required to correct dynamic correlation fully by CASSCF methods. For example, in the case of (6,6) active space, there are only 175 CSFs. If we consider twice as many electrons and orbitals, (12,12) active space, then total number of CSFs would be 226512. Indeed, CASSCF calculations having more than a million CSFs are extraordinarily demanding of computing resources and are rarely performed. Hence, application of CASPT2 method is a popular alternative, where the dynamic correlation is considered by MP2 method on the CASSCF MOs.

The full configuration interaction (CI) is the most complete treatment of the molecular system possible within the finite set of wave functions.[18] A CI wave function is a multiple Slater determinant. Practical CI methods are limited by truncating the CI expansion at some level of substitution because full CI is very expensive in terms of computer resources. CI calculations are classified by the number of excitations to make each determinant. For example, the CI single excitation (CIS) method adds single excitations to the single Slater determinant. CIS calculations provide a good estimate of the excited states and their properties. A disadvantage of these limited CI methods is in that they are not size-consistent. The Quadratic CI (QCI) method was designed to correct this problem. The Quadratic CISD (QCISD) method[15,18] is the most commonly used among CI methods. It is derived from CISD by including enough higher-order terms to make it size-consistent. Triple excitations are often included perturbatively into QCISD in order to obtain greater accuracy, which is called QCISD(T),[15] one of the most popular methods for high-level treatment of electron correlation.

Coupled cluster (CC) methods[13,15,25] treat electron correlation beyond MP4 with greater accuracy. CC methods include the effects of single and double excitation, effectively adding higher order excitation than MP4. CC calculations are similar to CI methods in that the CC wavefunction is expressed as an exponential of excitations operating on a single Slater determinant, which solves the size-consistency problem of CI methods. The cluster operator is a

sum of excitations of singles and doubles, etc. These excitations are commonly truncated at double excitations to give Coupled Cluster Singles and Doubles (CCSD).[15] The CCSD(T) method includes the same perturbative correction from triples as in QCISD(T), and QCISD(T) and CCSD(T) often gives similar quality in terms of accuracy of energies and geometries.[13,17] CC theory is also developed for treating excited states in a method called the equation-of-motion (EOM) CCSD and gives very good estimates of vertical excitation energies.[13,18]

Density functional theory (DFT) is based on the theorem by Hohenberg and Kohn[26] which states that the ground state molecular properties can be calculated from ground state electron probability density ρ. The ground state energy E is a functional of ρ and the total energy can be expressed as:

$$E[\rho] = T_s[\rho] + V_{ext}[\rho] + J[\rho] + E_{xc}[\rho]. \tag{22}$$

Here $T_s[\rho]$ is the kinetic energy of a set of n independent electrons, moving in an effective one-electron potential which leads to the density $\mathbf{\rho}(r)$, $V_{ext}[\rho]$ is the potential energy in the field of the nuclei plus any external perturbation, and $J[\rho]$ is the total Coulomb interaction. $E_{xc}[\rho]$ is usually described as the exchange-correlation energy. The one-electron Kohn-Sham operator is the same as the Fock operator in the HF equation except that the Kohn-Sham operator has an additional exchange-correlation term (E_{xc}). This term represents the key problem in DFT, since the exact expression of the E_{xc} is unknown, and approximations must be used. Various approximate functionals for E_{xc} are used in DFT calculations. However, there is no systematic way to improve electron correlation.

The simplest approach is the local spin density approximation (LDA), in which the function for the uniform electron gas density ρ_σ is integrated over the whole space:

$$E_{xc}^{LDA} = \sum_\sigma \int \varepsilon_{xc}^{unif}(\rho_\sigma) \rho_\sigma(r)^{4/3} dr \tag{23}$$

where $\varepsilon_{xc}^{unif}(\rho_\sigma)$ is the exchange-correlation energy distribution per unit volume, which depends

on the density only at the point where is evaluated. While this approximation is responsible for

the early success of DFT, it often provides unsatisfactory results in chemical applications.

Several corrections for the non-uniformity of atomic and molecular densities have been

proposed. In particular, those based on the gradient of the electron density ($\nabla \rho_\sigma$) have been

embraced due to their simplicity. These corrections, collectively referred to as generalized

gradient approximation (GGA), are usually expressed in terms of an enhancement factor over the

exchange energy of the uniform electron gas, so that the total exchange energy takes the form:

$$E_{xc}^{GGA} = E_{xc}^{LDA} - \sum_\sigma \int F_{xc}^{GGA}[\rho_\sigma, \nabla \rho_\sigma] \rho_\sigma(r)^{4/3} dr.$$ (24)

While $\varepsilon_{xc}^{unif}(\rho_\sigma)$ in equation (23) is uniquely defined, there is no unique function for F_{xc}^{GGA}, and

a number of GGA exchange-correlation functionals have been proposed. Roughly speaking, we

can consider two main classes: the first one is the functionals containing parameters, which are

fitted to some sets of experimental data, while the second class includes functionals which fulfill

a number of theoretical physical constraints. Although most existing functionals combine both

approaches, recently attention has shifted to the first aspect even at the expense of a fitting

process to introduce a huge number of parameters and of overemphasizing the thermochemistry

of organic molecules. In contrast with this tendency, functionals belonging to the second class

are particularly attractive to theoretical chemists, due to their strong theoretical background. In

the line of this trend, the non-empirical GGA functional of Perdew, Burke and Ernzerhof

(PBE),[29,30] can be considered as the most promising non-empirical functional. In particular, it

was constructed to retain a number of physical features in the correlation and in the exchange

parts.

The difference between DFT methods lies in the choice of the functional for the

exchange-correlation term (E_{xc}).[26,31] In practice, the functional for E_{xc} can be expressed as the

sum of an exchange functional (E_x) and a correlation functional (E_c) which only depend on the

electron density. These gradient-corrected functionals give better results in terms of geometries and relative energies than local density functionals. Some commonly used gradient-corrected exchange functionals are the PW86, B88, and PW91 functionals,[28,31] and gradient-corrected correlation functionals are the LYP and P86 functionals. PBE, a relatively new GGA functional, is gaining popularity. Any exchange functional can be combined together with any correlation functional. For example, the PW91LYP functional is defined as the PW91 exchange functional and the LYP correlation functional.

A further improvement can be achieved by hybridizing HF and DFT methods,[31] in which a HF exchange term and DFT exchange functionals are mixed in conjunction with a correlation functional. One of the most successful approaches is Becke's three-parameter model. This model rests on a linear combination of HF exchange with density functional exchange-correlation contributions, equation (25).

$$E_{xc}^{hybrid} = a_{x0}E_{xc}^{LDA} + (1 - a_{x0})E_x^{HF} + a_{x1}\Delta E_x^{GGA} + E_c^{LDA} + a_c\Delta E_c^{GGA}. \tag{25}$$

Three semiempirical parameters, a_{x0}, a_{x1} and a_c, have been determined by fitting the heats of formations of a standard set of molecules. The most popular implementation is the B3LYP method, which uses the Becke 88 exchange functional together with the Lee-Yang-Parr correlation functional.

$$E_{xc}^{B3LYP} = a_{x0}E_{xc}^{LDA} + (1 - a_{x0})E_x^{HF} + a_{x1}\Delta E_x^B + E_c^{VWN} + a_c\Delta E_c^{LYP} \tag{26}$$

Another hybrid functional gaining popularity is PBE1PBE, which can be expressed as equation (27).

$$E_{xc} = E_{xc}^{GGA} + \frac{1}{4}(E_x^{HF} - \Delta E_x^{GGA}) \tag{27}$$

The PBE1PBE hybrid functional gives excellent nonbonding interaction energies and equilibrium distances. In addition, it also gives accurate results for a large number of molecular properties, including EPR and NMR spectroscopic parameters, polarizabilities and vertical excitation

energies.[28,32] The quest for a better pure GGA functional has led to a new generation of DFT

methods, called meta-GGA. The ultimate goal is to construct a totally non-local density

functional, however the process is difficult. A more practical way is to construct a functional

containing additional semi-local information. This can be done by including the kinetic energy

density of the occupied Kohn-Sham (KS) orbitals:

$$\tau_\sigma(r) = \frac{1}{2} \sum_i^{occup} |\nabla \psi_{i\sigma}(r)|^2 \tag{28}$$

so that

$$E_{xc}^{m-GGA} = E_{xc}^{LDA} - \sum_\sigma \int F_{xc}^{GGA}[\rho_\sigma, \nabla\rho_\sigma, \tau]\rho_\sigma(r)^{4/3} dr. \tag{29}$$

These new functionals are called meta-GGA (mGGA).[33]

Time-dependent density functional theory (TDDFT)[34] has recently been introduced to

calculate excitation energies and oscillator strengths. TDDFT is derived from the time-dependent

Hartree-Fock (TDHF) equation; it includes electron correlation which is not present in TDHF.

TDDFT is roughly comparable to CI single excitation (CIS). Furthermore, excitation energies

computed by TDDFT are considerably improved as comparable to CIS.

DFT methods employ KS orbitals which allow the molecular ground state electron

density ρ to be calculated. The Kohn-Sham orbitals resemble HF MOs, and the KS orbitals can

be used in qualitative discussions of molecular properties and reactivities. DFT has a

computational cost similar to the HF model, but is faster and more efficient than conventional

electron correlation methods such as MP2. The advantage of DFT methods is that they include

electron correlation and take almost the same computer resources as HF calculations which

neglect electron correlation. It is known that B3LYP results are at least equal to MP2 in terms of

geometries and relative energetics and often better. However, DFT methods often fail to

reproduce excited state properties and non-bonded interactions such as hydrogen bonding and

London dispersion forces.[28,31] However better exchange correlation functionals have been

constructed recently and expected to lead to more applications and better results.

1.8 Compound models

A calculation at a very accurate level of theory requires a high computational cost. In an effort to achieve high accuracy at less computational cost, several new models have been suggested. A series of calculations are run and their results are systematically combined to predict a more accurate energy value for the molecule. Even though multiple calculations are run, their total computational cost is still significantly less than that of the single, high-level calculation.

Gaussian theory was introduced by Pople and co-workers[35] in order to compute thermodynamic properties such as heats of formation and atomization energies with chemical accuracy, meaning an error of less than 1-2 kcal/mol. Gaussian theory is an empirically defined energy correction scheme using several moderate size-correlated calculations to extrapolate to high accuracy. Three models, G1, G2 and G3, have been developed and the G3 model[32] is the most improved method. The G3 calculation scheme will be briefly discussed.

(1) HF/6-31G(d) geometry optimization followed by frequency calculation to obtain zero-point vibration energy which is scaled by 0.8929 to give a zero-point energy correction E(ZPE).

(2) MP2(full)/6-31G(d) geometry optimization.

(3) MP4/6-31G(d) single-point calculation on the MP2(full)/6-31G(d) geometry designated as MP4/6-31G(d)//MP2(full)/6-31G(d). This energy will be modified by the following series of corrections.

i. Correction for diffuse functions:

$$\Delta E(+) = E[\text{MP4/6-31+G(d)}] - E[\text{MP4/6-31G(d)}] \tag{22}$$

ii. Correction for polarization functions:

$$\Delta E(2df,p) = E[\text{MP4/6-31G(2df,p)}] - E[\text{MP4/6-31G(d)}] \tag{23}$$

24

iii. Correction for quadratic CI:

$$\Delta E(QCI) = E[QCID(T)/6\text{-}31G(d)]\text{-}E[MP4/6\text{-}31G(d)] \tag{24}$$

iv. Correction for larger basis set effects:

$$\Delta E(G3large) = E[MP2(full)/G3large]\text{-}E[MP2/6\text{-}31G(2df,p)]$$

$$- E[MP2/6\text{-}31\text{+}G(d)] + E[MP2/6\text{-}31G(d)] \tag{25}$$

where G3large basis set is 6-311+G with (2df,2p) for first row elements and hydrogen and (3d2f) for second row elements.

(4) The MP4/6-31G(d) energy and the four corrections from the steps above are combined along with a spin-orbit correction, $\Delta E(SO)$, which is taken from experiments if available and accurate calculations otherwise for atomic species only.

$$\Delta E(combined) = E[MP4]/6\text{-}31G(d)] + \Delta E(+) + \Delta E(2df,p) + \Delta E(QCI)$$

$$+ \Delta E(G3large) + \Delta E(SO) \tag{26}$$

(5) High level correction E(HLC) is added

$$E_e(G3) = E(combined) + E(HLC) \tag{27}$$

E(HLC) is an empirical correction to take into account remaining deficiencies and is defined by the number of α and β valence electrons.

(6) Total energy at 0K, $E_0(G3)$ is obtained by adding E(ZPE).

$$E_0(G3) = E_e(G3) + E(ZPE). \tag{28}$$

In order to test the accuracy of the G3 method, a reference set which is referred to as the G2/97 set was used. It includes 148 enthalpies of formation, 88 ionization potentials, 58 electron affinities, and 8 proton affinities. The overall average absolute deviation of the G3 method with experiment for this reference set is 1.02 kcal/mol.[36]

There are some other compound methods which achieve even better accuracy. The complete basis set (CBS) method is aimed at extrapolating finite basis set calculations at various levels of theory to obtain estimates of the CBS limit.[37] Wiezmann-1 (W1) and Wiezmann-2 (W2)

theories are developed to reach a better accuracy, 0.2-0.3kcal/mol.[38] This is very useful only

when the molecule under investigation is very small (up to 3-4 heavy atoms) and for benchmark

calculations.

1.9 References

1.   Born, M; Oppenheimer, J. R. *Ann. Phys. (Leipzig)* **1927**, *84*, 457.

2.   Hirst, D. M. *Potential Energy Surfaces: molecular structure and reaction dynamics*, Talyer & Fransis: London, 1985.

3.   (a) Lawley, K. P. Ed. *Adv. Chem. Phys.: Potential Energy Surface*; Wiley: New York, 1980. (b) *Faraday Discussions of the Chemical Society*, Chem. Soc.:London, **1977**, *62* .

4.   Hund, F. *Z. Phys.* **1927**, *40*, 742.

5.   Neumann, J. v.; Wigner, E. P. *Z. Phys*. 1929, 30. 467.

6.   For more comprehensive and theoretical discussion about conical intesections, please refer to (a) Domcke, W.; Yarkony, D. R.; Köppel, H. Ed. *Adv. Ser. Phys. Chem.: Conical Intersections: Electronic Stucture, Dynamics & Spectroscopy;* World Scientific: New Jersey, 2004. (b) Paterson, M. J.; Bearpark, M. J.; Robb, M. A.; Blancafort, L.; Worth, G. A. *Phys. Chem. Chem. Phys*. **2005**, *7*, 2100.

7.   Haas, Y.; Zilberg, S. "Conical Intersections in Molecular Photochemistry: The Phase-Change Approach" In Prigogine, I.; Rice, S. A. Ed. *Adv. Chem. Phys.: The Role of Degenerate States in Chemisry*; Wiley: New York, 2002.

8.   Longuet-Higgins, H. C. *Proc. Roy. Soc.* **1975**, *A344*, 147.

9.   Jahn, H. A.; Teller, E. *Proc. Roy. Soc. Lond. Ser. A*, **1937**, *161*, 220.

10.   Bersuker, I. B.; Polinger, V. Z. *Vibronic Interactions in Molecules and Crystals*, Springer Verlag: Heidelberg, 1989.

11.   (a) Renner, R. *Z. Phys*. **1934**, *92*, 172. (b) Herzberg, G. *Molecular Spectra and Molecular Structure III. Electronic Spectra and Electronic Structure of Polyatomic Molecules*; Van Nostrand: New York, 1967.

12.   Lee, T. J.; Fox, D. J.; Schaefer, H. F.; Pitzer, R. M. *J. Chem. Phys.* **1984**, *81*, 356.

13.   (a) Szabo, A.; Ostlund, N. S. *Modern Quantum Chemistry: Introduction to Advanced*

Electronic Structure Theory; McGraw-Hill:New York, 1989. (b) Levine, I. N. *Quantum Chemistry, Fifth Ed.*, Prentice-Hall, Inc.: New Jersey, 2000.

14.   Roothaan, C. C. J. *Rev. Mod. Phys.* **1951**, *23*, 69.

15.   Hehre, W. J.; Radom, L.; Schleyer, P. v. R.; Pople, J. A. *Ab Initio Molecular Orbital Theory*, Wiley and Sons: New York, 1986.

16.   Turner, A. G. *Methods in Molecular Orbital Theory*, Prentice-Hall, Inc.: New Jersey, 1974.

17.   Foresman, J. B.; Frisch, *A. Exploring Chemistry with Electronic Structure Methods, 2nd Ed.*, Gaussian Inc.: Pittsburgh, 1996.

18.   Jensen, F. *Introduction to Computational Chemistry*, Wiley: New York, 1999.

19.   Feller, D.; Davidson, E. R. In *Reviews in Computational Chemistry,* Lipkowitz, K. B.; Boyd, D. B. Ed. VCH: New York, 1990. pp 1-43.

20.   Frenking, G.; Antes, I.; Böhme, M.; Dapprich, S.; Ehlers, A. W.; Jonas, V.; Neuhaus, A.; Otto, M.; Stegmann, R.; Veldkamp, A.; Vyboishchikov, S. F. In *Reviews in Computational Chemistry Vol. 8*; Lipkowitz, K. B.; Boyd, D. B. Ed. VCH: New York, 1996, pp 63-144.

21.   Cundari, T. R.; Benson, M. T.; Lutz, M. L.; Sommerer, S. O. In *Reviews in Computational Chemistry Vol. 8*; Lipkowitz, K. B.; Boyd, D. B. Ed., VCH: New York, 1996, pp 145-202.

22.   Hay, P. J.; Wadt, W. R. *J. Chem. Phys*. **1985**, *82*, 270.

23.   Stevens, W. J.; Basch, H.; Krauss, M. *J. Chem. Phys*. **1984**, *81*, 6026.

24.   Dolg, M.; Wedig, U.; Stoll, H.; Preuss, H. *J. Chem. Phys*. **1987**, *86*, 866.

25.   Bartlett, R. J. *J. Phys. Chem*. **1989**, *93*, 1697.

26.   Parr, R. G.; Yang, W. *Density-Functional Theory of Atoms and Molecules*, Oxford Univ. Press: Oxford, 1989.

27. Lawley, K. P. Ed. *Adv. Chem. Phys.: Ab Initio Methods in Quantum Chemistry-II*, Wiley: New York, 1987.

28. Cramer, C. J. *Essentials of Computational Chemistry: Theories and Models*, Wiley: New York, 2004.

29. Perdew, J. P.; Burke, K.; Ernzerhof, M. *Phys. Rev. Lett.* **1997**, *78*, 1396.

30. Perdew, J. P.; Burke, K.; Ernzerhof, M. *Phys. Rev. Lett.* **1996**, *77*, 3865

31. Koch, W.; Holthausen, M. C. *A Chemist's Guide to Density Functional Theory,* Wiley-VCH: Weinheim, 2000.

32. Xu, Xin; Goddard, W. A. III, *J. Chem. Phys.* **2004**, *121*, 4068.

33. Tao, J.; Perdew, J. P.; Scuseria, G. E.; Staroverov, V. N. *Phys. Rev. Lett.* **2003**, *91*, 146401.

34. Gross, E. K. U.; Kohn, W. *Adv. Quantum Chem.* **1990**, *21*, 255.

35. Pople, J. A.; Head-Gordon, M.; Fox, D. J.; Raghavachari, K.; Curtiss, L. A. *J. Chem. Phys.* **1989**, *90*, 5622.

36. Curtiss, L. A.; Raghavachari, K.; Redfern, P. C.; Rassolov, V.; Pople, J. A. *J. Chem. Phys.* **1998**, *109*, 7764.

37. (a) Petersson, G. A.; Tensfeldt, T. G.; Montgomery, J. A. Jr. *J. Chem. Phys.* **1991**, *94*, 6091. (b) Montgomery, J. A. Jr.; Ochterski, J. W.; Petersson, G. A. *J. Chem. Phys.* **1994**, *101*, 5900.

38. Marin, J. M. L.; Oliveira, G. de, *J. Chem. Phys.* **1999**, *111*, 1843.

CHAPTER 2

AN INVESTIGATION OF THE BCP POTENTIAL ENERGY SURFACE

2.1 Introduction

The physical properties of nano-materials are affected by the nature of the constituting elements, their composition, and their crystalline structure. Great attention has been paid to group 13, 14 and 15 elements because they have the same number of valence electrons as materials that are already developed and widely used in industry. Furthermore, there has been a good deal of interest in materials composed of carbon, nitrogen and boron since they are expected to have useful properties as semiconductors, batteries, etc.[1-6] In addition, BCN compounds are known to possess tunable band gaps by changing the elemental composition and by adapting different synthetic methods which lead to different crystalline structures. Even though a number of theoretical studies of BCN are available,[7-10] to our knowledge no experimental or theoretical study of the BCP molecule, which is isoelectronic to C_3 and BCN, has been reported. Because of similarity of the electronic structure, BCP can be expected to possess similar physical properties to BCN, which piqued our interest.

BCP can be formed through the reaction of a diatomic with an atom such as BC + P, B + CP and C + BP. While both diatomic molecules BC and CP have been observed, boron carbide is best known both theoretically and experimentally.[11-20] By using mass spectrometry Drowart and co-workers determined that BC has a bond dissociation energy of 105 ± 10 kcal/mol.[11-12] Kuoba and Öhrn[13] established the ground state for BC as $^4\Sigma^-$ with the major configuration

$1\sigma^2 2\sigma^2 3\sigma^2 4\sigma^2 5\sigma 1\pi^2$. Fernando and co-workers obtained various spectroscopic parameters

including the equilibrium bond length $r_e = 1.491$ Å by studying gas phase emission spectra of

BC.[14] Recently, Tzeli and Mavridis reported MRCI calculations using a complete basis limit

extrapolation and argued that their value for D_e (102.2±0.1 kcal/mol) was more accurate than the

experimental value (108±7 kcal/mol).[20] Another interesting boron compound is boron phosphide,

BP, which is made into semiconducting thin films by chemical vapor deposition.[21] The electronic

structure and band gaps of BP polymers have been studied,[22-24] but investigations of monomeric

BP are rare. Interest in carbon phosphide has been sparked by the discovery of CP in the inner

layers of the carbon star envelope IRC+10216.[25] In addition, a serious deviation between the

calculated heat of formation of CP and the experimental values in the NIST webbook has been

discovered.[26-28] Now, it is accepted that the recommended value for ΔH_f (0K) of CP is about 124

kcal/mol rather than 106 kcal/mol.

We report herein a comprehensive study on the singlet and triplet potential energy surfaces of

the hypothetical BCP molecule using DFT, CASSCF and CASPT2 methods. Various

spectroscopic and thermodynamic parameters are also calculated at each level. For the linear

triatomic species which have degenerate electronic states ($^3\Pi$), Renner-Teller (RT) effects were

examined by harmonic vibrational frequency analysis. This work has been published in the

Journal of the Physical Chemistry A in 2004.[29]

2.2 Computational details

The Gaussian98 program[30] was used for density functional UB3LYP[31] calculations, the

GAMESS program[32] for Complete Active Space SCF (CASSCF)[33] calculations and the

MOLCAS 5.4[34] for CAS calculations with dynamic electron correlation introduced at the MP2

level (CASPT2).[35] All calculations were carried out on a cluster of linux computers. Geometry

optimizations for minima and transition states were carried out at the UB3LYP and full-valence

CASSCF(12,12) levels with the 6-311+G(2df) basis set.[36] Further stability tests and wave

function optimizations were performed to find spin-broken symmetry solutions at the UB3LYP

level. According to harmonic vibrational frequency analyses, each stationary structure was

characterized as a minimum (no imaginary frequencies) or as a transition state (one imaginary

frequency) at the UB3LYP/6-311+G(2df) level. Zero-point vibrational energies and heat capacity

corrections were obtained from UB3LYP/6-311+G(2df) frequency calculations. On the triplet

potential energy surface there were intruder state problems, which were solved by applying the

level shift (LS) technique.[37] Transition vectors of transition states were visualized and animated

by the MOLDEN program[38] to insure that the motions were as expected.

For triplet linear isomers vibrational frequencies at the CASSCF(12,12)/6-311+G(2df)

level were also calculated to investigate the Renner-Teller effect.[39] Dynamic electron correlation

was considered by utilizing single-point full-valence CASPT2 calculations for every stationary

point calculated at the CASSCF(12,12)/6-311+G(2df) level with the ANO-L basis set[40] which is a

[7s7p5d4f] contraction of the [17s12p5d4f] primitive set for the phosphorus atom and a

[7s7p4d3f] contraction of the [14s9p4d3f] primitive set for boron and carbon atoms. Throughout

this paper, we will refer to UB3LYP/6-311+G(2df) as DFT, CASSCF(12,12)/6-311+G(2df) as

CAS, and CASPT2(12,12)/ANO-L//CASSCF(12,12)/6-311+G(2df) as CASPT2, respectively. In

the GAMESS and MOLCAS calculations, the C_{2v} point group was adapted for linear isomers due

to limitations in handling high symmetry. The geometry of the conical intersection was obtained

at the CASSCF(6,6)/6-311+G(2df) level by using Gaussian98, and then single-point calculations

for both electronic states (^3A' and ^3A") were carried out at the CAS level with GAMESS and

CASPT2 level with MOLCAS. The natural bonding orbital (NBO)[41] program implemented in

Gaussian98 program was used for the Wiberg bond index (WBI)[42] analysis. Thermodynamic and

spectroscopic properties were calculated from the DFT and CASPT2 results as described in the

literature.[43] For comparison, we also performed G3B3[44] calculations to obtain the heat of

formation of **S1** (Figure1). We will use a notation scheme with a boldface "**S**" for singlets and

"**T**" for triplets followed by one number for minima and two numbers for transition states. Thus,

T12 is the triplet transition state between triplet **T1** and triplet **T2**.

2.3 Results and Discussion

Important electronic configurations of diatomic fragments and minimum energy species

of BCP species are given in Table 1. For the diatomic fragments only ground states are

considered. The ground state electronic configurations of BC and CP are available from the

literature and we obtained the same configurations for the ground states of BC ($^4\Sigma^-$) and CP ($^2\Sigma^+$).

The ground state of BP is $^3\Pi$ with the electronic configuration $[Core]5s^26s^22p^37s^1$, which is the

same as previously reported.[45] This suggests that BP can be obtained by combining ground state

B and P atoms without change of electronic configuration. This fact can help explain why BP

can easily polymerize to form a polymeric film (boronphosphide) since the diradical is expected

to be kinetically labile.[21]

The ground state of the linear BCP (**S1**), the first excited linear triplet isomer (**T1**) and

other linear isomers have the electronic configurations:

$[Core]6s^27s^28s^22p^49s^2$ **S1** ($^1\Sigma^+$), **S3** ($^1\Sigma^+$)

$[Core]6s^27s^28s^22p^49s^13p^1$ **T1** ($^3\Pi$), **T6** ($^3\Pi$), **T34** ($^3\Pi$)
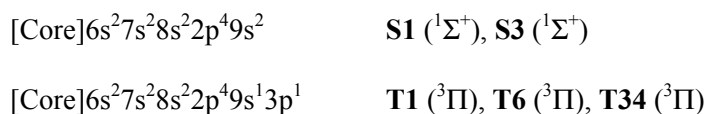
Triangular C_s symmetry isomers have electronic configurations:

$[Core]7a'^28a'^29a'^210a'^22a''^211a'^2$ **S2** ($^1A'$)

$[Core]7a'^28a'^29a'^210a'^22a''^211a'^112a'^1$ **T2**, **T3** ($^3A'$)

$[Core]7a'^28a'^29a'^210a'^22a''^211a'^13a''^1$ **T4**, **T5** ($^3A''$)
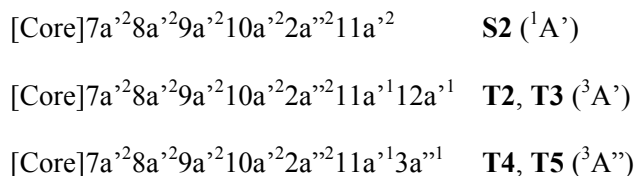
Table 1. Important electronic configurations of ground state diatomic fragments of BCP and minimum energy isomers of BCP at the CASPT2 level[a]

Species	E-State	Configurations	C_i^2
BC	$^4\Sigma^-$ ($^4A_2$)	$3\sigma^2\,4\sigma^2\,5\sigma\,1\pi_x\,1\pi_y$	0.89
		$3\sigma^2\,4\sigma\,5\sigma^2\,1\pi_y\,2\pi_x$	0.02
		$3\sigma^2\,4\sigma\,5\sigma^2\,1\pi_x\,2\pi_y$	0.02
CP	$^2\Sigma^+$ ($^2A_1$)	$5\sigma^2\,6\sigma^2\,2\pi^4\,7\sigma$	0.85
		$5\sigma^2\,6\sigma^2\,2\pi_x^2\,7\sigma\,3\pi_y^2$	0.02
		$5\sigma^2\,6\sigma^2\,2\pi_y^2\,7\sigma\,3\pi_x^2$	0.02
		$5\sigma^2\,6\sigma^2\,2\pi_x^2\,1\bar{\pi}_y\,7\sigma\,3\pi_y$	0.01
		$5\sigma^2\,6\sigma^2\,2\bar{\pi}_x\,1\pi_y^2\,7\sigma\,3\pi_x$	0.01
BP	$^3\Pi$ ($^3B_1$)	$5\sigma^2\,6\sigma^2\,2\pi_x\,2\pi_y^2\,7\sigma$	0.90
		$5\sigma^2\,6\sigma^2\,2\pi_x\,7\sigma\,3\pi_y^2$	0.02
S1	$^1\Sigma^+$ ($^1A_1$)	$6\sigma^2\,7\sigma^2\,8\sigma^2\,2\pi^4\,9\sigma^2$	0.82
		$6\sigma^2\,7\sigma^2\,8\sigma^2\,2\pi^4\,3\pi_x\,4\bar{\pi}_x$	0.01
		$6\sigma^2\,7\sigma^2\,8\sigma^2\,2\pi^4\,3\pi_y\,4\bar{\pi}_y$	0.01
		$6\sigma^2\,7\sigma^2\,8\sigma^2\,2\pi_x^2\,9\sigma^2\,3\pi_y^2$	0.01
		$6\sigma^2\,7\sigma^2\,8\sigma^2\,2\pi_y^2\,9\sigma^2\,3\pi_x^2$	0.01
		$6\sigma^2\,7\sigma^2\,8\sigma^2\,2\pi_x\,2\pi_y\,9\sigma^2\,3\bar{\pi}_x3\bar{\pi}_y$	0.01
S2	$^1A'$	$7a'^2\,8a'^2\,9a'^2\,10a'^2\,2a''^2\,11a'^2$	0.78
		$7a'^2\,8a'^2\,9a'^2\,10a'^2\,2a''^2\,12a'^2$	0.08
		$7a'^2\,8a'^2\,9a'^2\,10a'^2\,11a'^2\,3a''^2$	0.01
S3	$^1\Sigma^+$ ($^1A_1$)	$6\sigma^2\,7\sigma^2\,8\sigma^2\,2\pi^4\,9\sigma^2$	0.73
		$6\sigma^2\,7\sigma^2\,8\sigma^2\,2\pi_y^2\,9\sigma^2\,3\pi_x^2$	0.05
		$6\sigma^2\,7\sigma^2\,8\sigma^2\,2\pi_x^2\,9\sigma^2\,3\pi_y^2$	0.05
		$6\sigma^2\,7\sigma^2\,8\sigma^2\,2\pi_x2\pi_y9\sigma^23\bar{\pi}_x\,3\bar{\pi}_y$	0.03
		$6\sigma^2\,7\sigma^2\,8\sigma^2\,2\pi_x\,2\bar{\pi}_y\,9\sigma^2\,3\pi_x3\bar{\pi}_y$	0.02
		$6\sigma^2\,7\sigma^2\,8\sigma^2\,2\pi_x^2\,2\pi_y\,9\sigma^2\,3\bar{\pi}_y$	0.01
		$6\sigma^2\,7\sigma^2\,8\sigma^2\,2\pi_x\,2\pi_y^2\,9\sigma^2\,3\bar{\pi}_x$	0.01
T1	$^3\Pi$ ($^3B_1$)	$6\sigma^2\,7\sigma^2\,8\sigma^2\,2\pi^4\,9\sigma\,3\pi_x$	0.85
		$6\sigma^2\,7\sigma^2\,8\sigma^2\,2\pi_x^2\,9\sigma\,3\pi_x3\pi_y^2$	0.02
T2	$^3A'$	$7a'^2\,8a'^2\,9a'^2\,10a'^2\,2a''^2\,11a'\,12a'$	0.86
		$7a'^2\,8a'^2\,9a'^2\,10a'^2\,11a'\,12a'\,3a''^2$	0.01
T3	$^3A'$	$7a'^2\,8a'^2\,9a'^2\,10a'^2\,2a''^2\,11a'\,12a'$	0.79
		$7a'^2\,8a'^2\,9a'^2\,10a'^2\,11a'\,12a'\,3a''^2$	0.01
T4	$^3A''$	$7a'^2\,8a'^2\,9a'^2\,2a''^2\,10a'^2\,11a'\,3a''$	0.80
		$7a'^2\,8a'^2\,9a'^2\,2a''\,10a'^2\,11a'\,3\bar{a}''\,4a''$	0.01
T5	$^3A''$	$7a'^2\,8a'^2\,9a'^2\,2a''^2\,10a'^2\,11a'\,3a''$	0.80
		$7a'^2\,8a'^2\,9a'\,2a''^2\,10a'^2\,11a'^2\,3a''$	0.01
T6	$^3\Pi$ ($^3B_1$)	$6\sigma^2\,7\sigma^2\,8\sigma^2\,2\pi^4\,9\sigma\,3\pi_x$	0.69
		$6\sigma^2\,7\sigma^2\,8\sigma^2\,2\pi_x^2\,9\sigma\,3\pi_x3\pi_y^2$	0.06
		$6\sigma^2\,7\sigma^2\,8\sigma^2\,2\pi_x^2\,2\bar{\pi}_y\,9\sigma\,3\pi_x3\pi_y$	0.03
		$6\sigma^2\,7\sigma^2\,8\sigma^2\,2\pi_x\,2\bar{\pi}_y\,9\sigma\,3\pi_x^2\,3\pi_y$	0.02
		$6\sigma^2\,7\sigma^2\,8\sigma^2\,2\pi_x^2\,2\pi_y\,9\sigma\,3\pi_x3\bar{\pi}_y$	0.01
		$6\sigma^2\,7\sigma^2\,8\sigma^2\,2\pi_x^2\,2\pi_y\,9\sigma\,3\bar{\pi}_x3\pi_y$	0.01

[a] Orbitals with a single β-spin electron are indicated with a bar over the orbital designation.

34
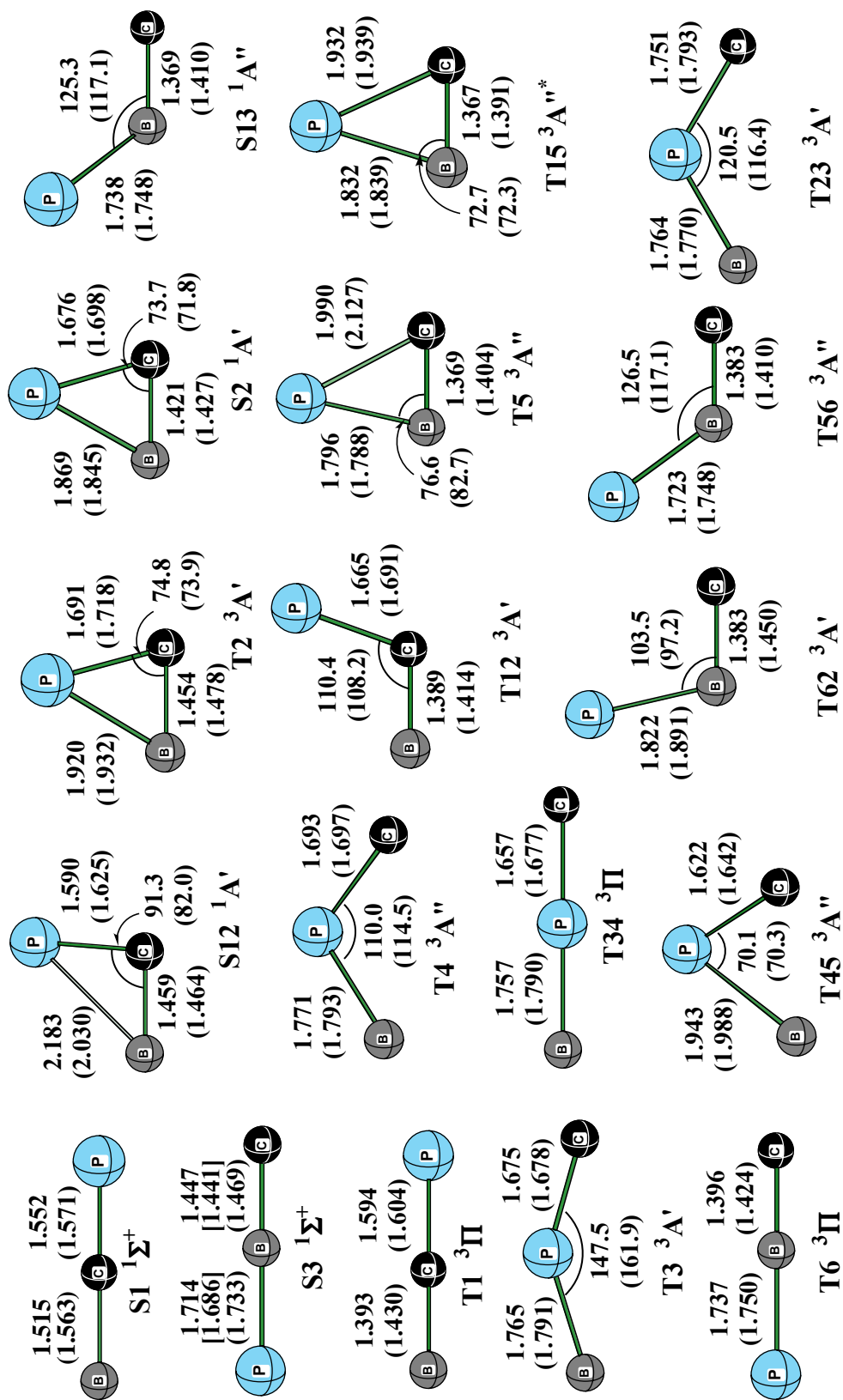
Figure 1. Optimized geometric parameters of stationary points at the DFT level with the CAS level in parentheses. Bond lengths are in Å and angles are in degrees. The symbol (*) indicates the geometry was obtained at the DFT level using the 6-311+G(df) basis set. The brackets for **S3** indicate the values obtained with RDFT (i.e. **S3'**).

Excitation from singlet state to triplet state can be accomplished by exciting one electron from the HOMO (9σ) to LUMO (3π). The other linear isomer on the singlet PES (CBP), **S3**, also has the same configuration as **S1**, and two triplet linear species (CBP, BPC), **T6** and **T34**, have the same configuration as **T1**. In our calculations for the triplet linear species, using the C_{2v} point group, we only calculate one component of the degenerate triplet state; however, we give the linear electronic state designation in Table 1. Linear species have some multireference character as judged by the square of coefficient of the dominant configuration to the wave function (C_i^2) which is between 0.69 and 0.85 (Table 1). The low-lying π orbitals ($2\pi/3\pi/4\pi$) play an important role in this system where four to six electrons are distributed among the π sets.

All possible linkage isomers of three atoms on singlet and triplet surfaces were considered. Optimized structures are as shown in Figure 1 and their relative energies are given in Table 2. Three singlet and six triplet minimum-energy structures are characterized from DFT geometry optimizations and frequency calculations. Among those isomers, singlet linear B-C-P, **S1** ($^1\Sigma^+$) proved to be the global minimum. For most structures, geometries optimized at the CAS level had slightly longer bonds lengths than those at the DFT level (Figure 1) due to the population of antibonding orbitals. The B-C bond lengths in **S1** and **T1** isomers showed larger deviations between DFT and CAS, these may be attributed to the neglect of dynamic electron correlations in the CASSCF method. In **S1** (BCP) the C-P bond is a triple bond (1.552 Å, DFT), slightly shorter than the experimental[46] bond length of CP (1.562 Å), while the B-C bond is a single bond (1.515 Å, DFT), and slightly longer than experimental[14] bond length in BC (1.491 Å). The C-P/B-C bond lengths (1.594/1.393 Å, DFT) in **T1** (BCP) are longer and shorter than a normal CP triple bond and a normal BC single bond, respectively. These bond length changes can be easily rationalized by drawing Lewis structures of **S1** and **T1**. As shown in Scheme 1, the triplet **T1** is formed from **S1** by promoting an electron from the lone pair of boron into an empty

π^* orbital of phosphorus. The CP bond in **T1** becomes weaker while the BC bond becomes stronger. At the CASPT2 + ZPC level, **T1** is 16.3 kcal/mol less stable than **S1**.

Three triangular planar structures, **S2**, **T2**, and **T5** are found to be minima and their electronic states are $^1A'$, $^3A'$ and $^3A''$, respectively. **S2** and **T2** have very similar geometries and
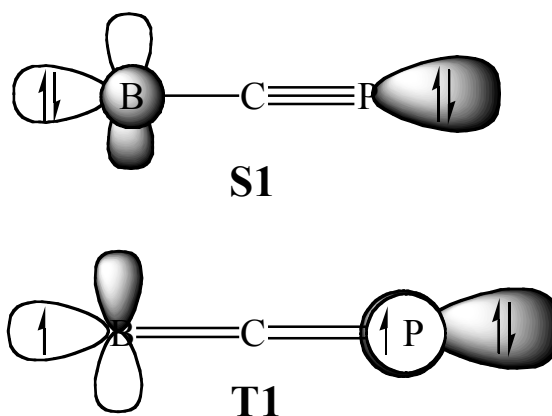
Scheme 1. Lewis structures of **S1** and **T1**

their energy difference is only 2.2 kcal/mol at the CASPT2 + ZPC level. Therefore, it is possible that vibrational excitation may lead to intersystem crossing. The other triangular isomer, **T5**, has a somewhat different structure from **S2** and **T2** with a much longer P-C bond (1.990 Å). All three isomers have relatively low energies despite high bond strain which may be attributed to the large size of the phosphorus atom and the relatively weak repulsion among the electron pairs around phosphorus.

Another pair of linear linkage isomers, **S3**/**T6** (P<u>BC</u>), shows very similar properties to **S1**/**T1** (P<u>CB</u>) where the BC fragment is rotated by 180°. The triplet (**T6**) can be formed from **S3** by promoting a phosphorus lone pair electron to an empty carbon π^*-orbital which, in turn, can form a partial B-C double bond. Thus, the B-C bond is shorter in **T6** than **S3** but the P-B bond is longer (B-C: 1.396/1.447 Å and P-B: 1.737/1.714 Å).

37

Table 2.   Relative Energies (in kcal/mol) of species on the potential energy surface of BCP

BCP	State	$\langle S^2 \rangle$[a]	Rw[b]	ZPC[a]	H_{corr}[a]	ΔE			ΔE + ZPC		
						DFT	CAS	CASPT2	DFT	CAS	CASPT2
S1[c]	$^1\Sigma^+$	0.15	0.91	3.6	6.7	0.0	0.0	0.0	0.0	0.0	0.0
S2	$^1A'$	0.72	0.90	4.0	6.6	12.4	24.7	13.6	12.8	25.1	14.0
S3[d]	$^1\Sigma^+$	0.56	0.90	3.4	6.5	35.6	42.4	35.6	35.4	42.2	35.4
S3'[d]	$^1\Sigma^+$	0.00		3.3	5.5	37.2			36.9		
S12	$^1A'$	0.29	0.90	3.0	5.4	19.8	29.7	19.4	19.2	29.1	18.8
S13	$^1A''$	1.10	0.89	3.3	5.7	63.0	83.8	70.3	62.8	83.6	70.0
T1	$^3\Pi$	2.02	0.90	4.3	7.0	11.2	19.7	15.6	11.9	20.4	16.3
T2	$^3A'$	2.01	0.88	4.0	6.5	15.1	28.3	15.8	15.5	28.7	16.2
T3	$^3A'$	2.06	0.89	2.5	5.5	93.5	97.6	91.2	92.5	96.6	90.2
T4	$^3\Pi$	2.08	0.90	3.1	5.5	87.6	93.3	88.5	87.1	92.8	88.0
T5	$^3A''$	2.03	0.88	3.5	6.3	50.2	61.2	49.2	50.1	61.1	49.1
T6	$^3A''$	2.46	0.89	3.7	6.5	52.5	59.2	52.1	52.7	59.4	52.3
T12	$^3A'$	2.01	0.87	3.5	5.9	30.9	43.4	34.0	30.9	43.4	33.9
T23	$^3A'$	2.03	0.89	2.2	4.7	94.9	103.2	95.2	93.6	101.9	93.8
T34	$^3\Pi$	2.05	0.89	2.5	4.6	93.9	97.7	91.0	92.8	96.6	89.9
T45	$^3A''$	2.38	0.90	2.0	4.6	99.1	102.1	99.8	97.6	100.5	98.3
T56[e]	$^3A''$	2.11	0.89	3.3	5.7	56.4	64.1	55.5	56.1	63.9	55.2
T15[f]	$^3A''$	2.03	0.91	3.2	5.6	50.2	81.3	48.2	49.8	80.9	48.7
T26[f]	$^3A'$	2.06	0.91	3.0	5.5	73.7	79.4	66.3	73.1	78.8	66.6
T$_{crs}$[g]				3.1	5.5		96.1	91.4		95.7	91.0

[a]   Spin-squared values $\langle S^2 \rangle$, zero-point corrections (kcal/mol), and heat capacity contributions to enthalpy at 298K (kcal/mol) were calculated at the B3LYP/6-311+G(2df) level.

[b]   Reference weights, the fraction of electron correlation energy obtained within the active space, were calculated at the CASPT2(12,12)/ANO-L//CASSCF(12,12)/6-311+G(2df) level.

[c]   For **S1**, the zero-point energy and heat capacity correction were computed with the RDFT method which gives an energy 0.2 kcal/mol higher than the UDFT method. The UDFT and RDFT geometries are very similar.

[d]   The **S3** species is determined by UDFT (broken-symmetry), while **S3'** is determined by RDFT (closed-shell). **S3** is a minimum while **S3'** is a transition state.

[e]   DFT results were obtained by using B3LYP/6-311+G(df) geometry optimization with a single-point calculation at the B3LYP/6-311+G(2df) level.

[f]   CASPT2 results were obtained by using the level shift method (see Table 3).

[g]   The geometry of the crossing point was obtained at the CASSCF(6,6)/6-311+G(2df) level. The ZPC from **T4** was used to compute the values under "ΔE + ZPC".

146.2 C (^{3}P) + BP($^3\Pi$)

128.9 P(^{4}S) + BC($^4\Sigma$)

128.9 BC($^4\Sigma$) + P(^{4}S)

111.7 B(^{2}P) + CP($^2\Sigma$)

[T23/T3/T34/T4/T45, T$_{crs}$]

Intermediates

B—P—C

66.6 T62 ^{3}A'

52.3 T6 $^3\Pi$

55.2 T56 ^{3}A''

49.1 T5 ^{3}A''

48.7 T15 ^{3}A''

33.9 T12 ^{3}A'

18.8 S12 ^{1}A'

16.3 T1 $^3\Pi$

14.0 S2 ^{1}A'

16.2 T2 ^{3}A'

P—B—C

0.0 S1 $^1\Sigma^+$

70.0 S13 ^{1}A''

35.4 S3 $^1\Sigma^+$

14.0 S2 ^{1}A'

B—C—P

P—B—C

Reaction Coordinate
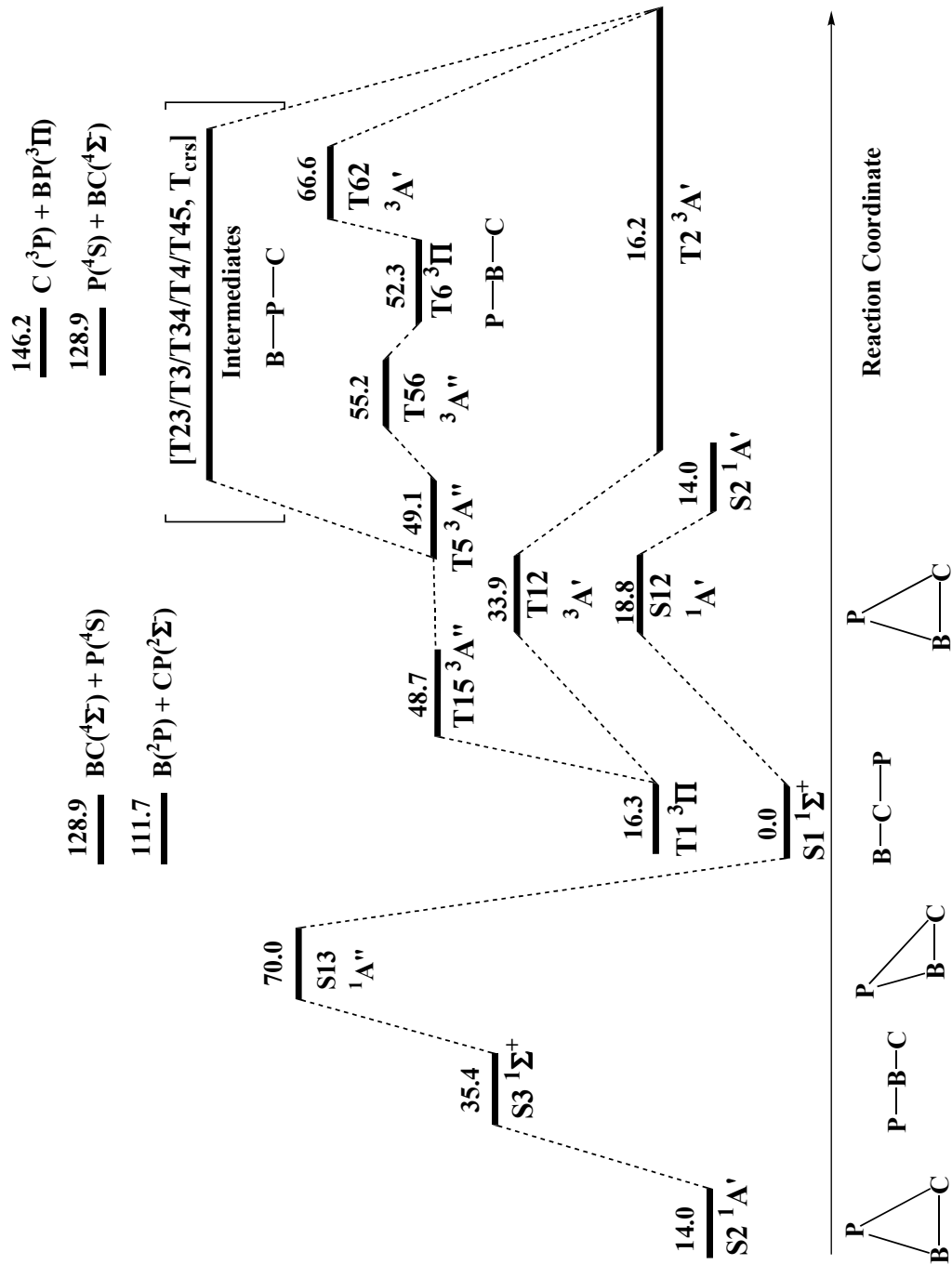
Figure 2.   Schematic potential energy surface for the BCP system. Relative energies (kcal/mol) are obtained at the CASPT2+ZPC level. More details of the PES within the brackets are given in Figure 4.

The remaining linkage isomer, B-P-C, was not found to be a minimum on either the singlet or triplet potential energy surface. Singlet linear B-P-C was found to be a high-energy transition state between **S2** configurations, while the triplet linear B-P-C (**T34**) is a degenerate ($^3\Pi$) Renner-Teller state connecting the **T3** ($^3A'$) and **T4** ($^3A''$) minima (see below for further discussion).

On the triplet surface there are intruder state problems with **T15** and **T62** at the CASPT2 level. We observed a low reference weight (Rw); 0.15 for **T15** and 0.34 for **T62**. By applying the level shift (LS) technique, we could remove the intrusion and obtained relative energies as shown in Table 3. When a 0.1 level shift parameter was applied, the problem was solved in **T15** (Rw: 0.90), but **T62** was still affected (Rw: 0.82). With a 0.2 LS parameter all intruder state problems disappeared. The same shifted values were used to calculate both minima connected to each transition state for comparison, and then zero-point energy corrections were applied to obtain the energy differences relative to **T2**. Finally, we note the strong structural similarity between the diradical transition states **S13** and **T56** ($^1A''$ and $^3A''$) at the DFT and CAS levels. The triplet **T56** is 15.3 kcal/mol higher in energy than **S13** (Figure 2) so intersystem crossing is unlikely.

The singlet and triplet potential energy surfaces are constructed based on their relative energies after zero-point energy corrections (Figure 2). As mentioned above, **S1** is the global minimum. On the singlet PES **S1** and **S2** are characterized as energy minima. Between **S1** and **S2**, a first-order saddle point, **S12**, is located 18.8 kcal/mol higher than **S1** and 4.8 kcal/mol higher than **S2**. An alternative mechanism for the **S1**→**S2** rearrangement is over the **S13** transition state ($^1A''$) through **S3**, the linear P-B-C species. At the UDFT level, **S3** has a $<S^2>$ value of 0.56 and no imaginary frequencies. However, at the RDFT level, the optimized linear structure (**S3'**) is only 1.5 kcal/mol higher in energy than the spin-broken symmetry UDFT

Table 3.   Energies relative to T2 (in kcal/mol) and reference weights (Rw) obtained by using the level shift (LS) technique[a,b]

LS	T1		T15		T5		T2		T26		T6	
	ΔE	Rw	ΔE	Rw	ΔE	Rw	ΔE	Rw	ΔE	Rw	ΔE	Rw
0.0	1.0	0.90	33.7	0.15	33.8	0.88	0.0	0.88	49.8	0.34	37.0	0.89
0.1	1.0	0.91	32.4	0.90	33.9	0.90	0.0	0.91	44.0	0.82	37.1	0.90
0.2	0.9	0.92	32.5	0.91	33.9	0.91	0.0	0.91	50.4	0.91	37.1	0.91

[a]   See Reference 37.

[b]   The reference weight is the fraction of the electron correlation obtained within the active space. A value significantly different from other species on the PES may indicate an intruder state problem.
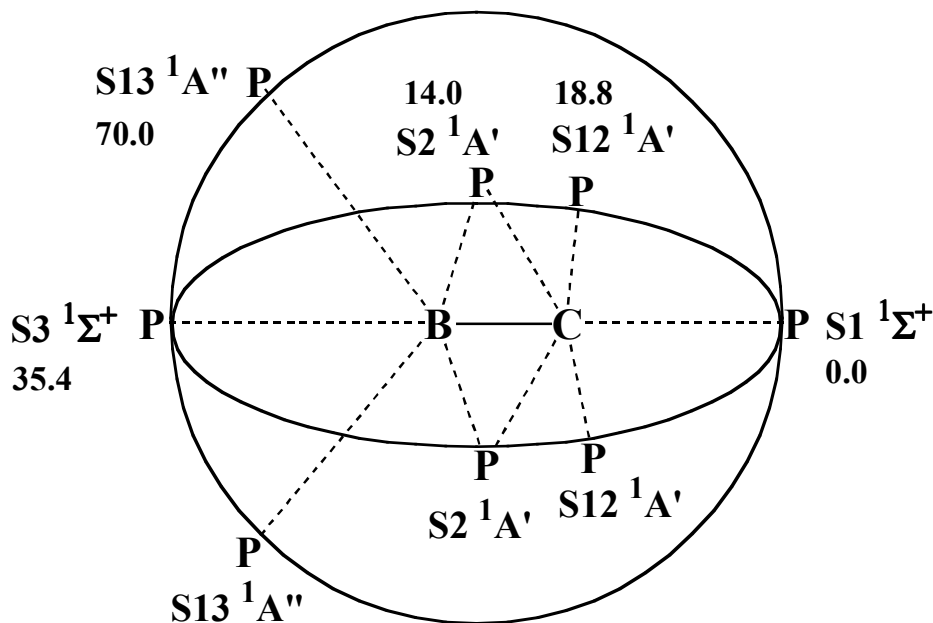
Figure 3.   Schematic drawing for revolution of the phosphorus atom around the B-C core on the singlet PES. The dashed lines represent the approximate B-C-P angle for the stationary points with the energy (kcal/mol) relative to **S1**. The outer circle indicates the A" surface while the inner eclipse indicates the A' surface. The A' and A" surfaces are degenerate at **S1** and **S3**.

solution and has two imaginary frequencies (**S2**→**S3'(RDFT)**→**S2**). While we are not

confident that **S3** is an intermediate on the PES, we do feel that the barrier to collapse to **S2** must

be very small. In addition, **S2** should undergo rearrangement over a transition state very much

like **S3** (i.e. **S3'(RDFT)**). In these two scenarios, the P atom can "orbit" the BC fragment

(Figure 3). Movement around the C-end gives the global minimum **S1**, while movement around

the B-end gives the P-BC (**S3**) and then back to **S2**.

The triplet potential energy surface is somewhat more complicated than the singlet PES.

The triplet surface is composed of ^{3}A', ^{3}A" and ^{3}P states, and all are connected to one another.

From the lowest energy isomer **T2**, the reaction can proceed over a 17.7 kcal/mol barrier (**T12**)

to reach linear **T1** by breaking the B-P bond, over a 50.4 kcal/mol barrier (**T62**) to reach linear

T6 by breaking the C-P bond, or over a 77.6 kcal/mol barrier (**T23**) to reach **T3** by breaking the

B-C bond. Breaking the C-P bond (**T2**→**T6**) occurs on the ^{3}A' surface to give the linear P-B-C

isomer (**T6**) which can then proceed on the ^{3}A" surface, since the ^{3}A' and ^{3}A" states are

degenerate in **T6**. A small 2.9 kcal/mol barrier (**T56**) separates **T6** from **T5** on the ^{3}A" surface.

From **T5**, the reaction proceeds without barrier (**T15** is lower in energy than **T5** at the

CASPT2+ZPC level).

A higher-energy pathway connecting **T2** and **T1** was calculated involving intermediate

species **T3**, **T4**, and a crossing point **T$_{crs}$**. While that pathway is not relevant on the **T1/T2**

pathway, it may be important in reactions between the fragments (BC + P, BP + C, CP + B).

As shown in Figure 4a, species **T3** (^{3}A') is 0.3 kcal/mol higher in energy than **T34** and

2.2 kcal/mol higher than **T4** (**T34**, a transition state at the CAS level, is stabilized relative to **T3**

and **T4** at the CASPT2 level). Similar to the **T62/T6/T56** pathway above, the reactant (**T3**)

starts on the ^{3}A' surface and finishes on the ^{3}A" surface (**T4**) while passing through **T34** ($^3\Pi$).

Distortion along one of the two imaginary bending modes (π_x and π_y) of linear B-P-C (**T34**)

gives rise to the ^{3}A' or ^{3}A" electronic surface.

42

a)

90.2
T3 ^{3}A'

89.9
T34 $^3\Pi$

88.0
T4 ^{3}A"

b)

1.943
(1.988)

1.622
(1.642)

70.1
(70.3)

98.3
T45 ^{3}A"

1.764
(1.770)

1.751
(1.793)

120.5
(116.4)

93.8
T23 ^{3}A'

(1.873)

(1.639)

(100.8)

T$_{crs}$

91.0

88.0
T4 ^{3}A"

1.920
(1.932)

74.8
(73.9)

1.830
(1.718)

1.454
(1.478)

1.771
(1.793)

1.693
(1.697)

110.0
(114.5)

16.2
T2 ^{3}A'

Figure 4.   (a) State crossing from the ^{3}A' surface to ^{3}A" surface via linear **T34** ($^3\Pi$).

(b) State crossing through a conical intersection. The geometry of **T$_{crs}$** is optimized at the CASSCF(6,6)/6-311+G(2df) level, and single-point calculations were performed for each state symmetry (^{3}A' and ^{3}A") at the CASPT2 level. The relative energy of **T$_{crs}$** was obtained by averaging the two state energies. Energies (kcal/mol) are relative to **S1**.

43

Figure 5.   Orbital crossing diagram around the conical intersection (see Figure 4 for details of the crossing).

Another interesting finding in this study is the occurrence of a conical intersection between the ^{3}A' and ^{3}A" surfaces. The location is between **T2**-**T23** on the ^{3}A' surface and **T45**-**T4** on the ^{3}A" surface (Figure 4b). The optimized structure of the crossing point (Figure 4b) is 3.0 kcal/mol higher in energy than **T4**. As the B-P-C angle increases, the energy of the ^{3}A' surface rises, while the energy of the ^{3}A" surface falls. The orbital interactions that are responsible for the crossing are given in Figure 5. When the structure is triangular, the 3a" orbital has a strong antibonding interaction between the p_z orbitals of boron and carbon which decreases as the B-P-C angle increases. At the same time, the bonding interaction in the 12a' orbital becomes more antibonding as the angle increases. The B-P-C angle at the crossing **T$_{crs}$** (100.8^o) is intermediate to the value in **T2** (74.8^o) and **T4** (110.0^o).

Calculated bond dissociation energies are shown in Table 4. Our bond dissociation energy (D_0) of B-C ($^4\Sigma^-$) is 100.9 kcal/mol at the CASPT2 level and 101.7 kcal/mol at the DFT level which is close to the experimental value[11,12] ($D_0 = 106\pm7$ kcal/mol) determined by mass

Table 4.   Calculated bond dissociation energies (in kcal/mol)

Bond	State	Products	D_e				D_0		
			DFT	CASPT2	G3B3	exptl	DFT	CASPT2	G3B3
B-C	$^4\Sigma^-$	$^2P + {}^3P$	103.4	102.6	104.3	$102.2^{a,b}$	101.7	100.9	102.7
C-P	$^2\Sigma^+$	$^3P + {}^4S$	123.2	119.9	126.2	123.5^c	121.3	118.1	124.4
B-P	$^3\Pi$	$^2P + {}^4S$	81.7	72.8	78.4	72.6^d	80.3	71.4	77.1
B-CP	$^1\Sigma^+$	$^2P + {}^2\Sigma^+$	117.4	113.4	118.0		115.7	111.7	116.3
BC-P	$^1\Sigma^+$	$^4\Sigma^- + {}^4S$	137.2	130.7	139.8		135.4	128.9	138.0
B-C-P	$^1\Sigma^+$	$^2P + {}^3P + {}^4S$	240.6	233.3	244.2		237.1	229.7	240.7

a   Reference 20.

b   Theoretical values of 97.0 kcal/mol[16] and 100.1 kcal/mol[19] have been reported.

c   Reference 25.

d   Reference 45(b).

spectroscopy. Tzeli and Marvridis[20] reported MRCI/cc-pVnZ-CBS calculations including scalar relativistic corrections (mass velocity + Darwin terms) and spin-orbit corrections and suggested a value of 100.5±0.1 kcal/mol for the B-C bond dissociation energy (D_0). Martin and Taylor[19] used calculations at the CCSD(T) level to obtain a BDE of B-C as 98.3±1 kcal/mol. Our CASPT2 and DFT calculations of the BDE (100.9, 101.7 kcal/mol) are very similar to those reported previously, while the G3B3 results give a slightly stronger B-C bond (102.7 kcal/mol).

For the bond dissociation energy of CP, our DFT results agree best with the reference D_e value of 123.5 kcal/mol[46] with CASPT2 about 4 kcal/mol lower and G3B3 about 3 kcal/mol higher than the experimental D_e values. The difference between the CASPT2 and G3B3 methods for the calculated D_e value of CP (as well as for the D_e values of BC and BP) are mainly due to the higher level correction (HLC)[44(a)] in which deficiencies in the basis set are empirically

corrected for based on the number of spin-paired electrons and unpaired electrons.[47] Without

this higher-level correction, the CASPT2 results are very similar to the G3B3 results.

Table 5. Wiberg Bond Index calculated at the DFT level

	B-C	C-P	B-P
S1	0.90	2.67	0.14
S2	1.76	1.74	1.16
S3	1.64	0.64	2.33
T1	1.40	2.06	0.16
T2	1.37	1.65	0.92
T3	0.19	2.02	1.53
T4	0.18	1.83	1.51
T5	2.02	0.70	1.34
T6	1.77	0.19	1.85

We report bond dissociation energies and atomization energy of BCP (**S1**) in Table 4. It

is surprising that the bond energy (D_e) of B-CP (113.4 kcal/mol, CASPT2) is larger than in BC

(102.6 kcal/mol, CASPT2), even though the DFT-based Wiberg Bond Index (WBI) of the B-C

bond is only 0.90 (Table 5). Also, the bond dissociation energy (D_e) of BC-P (130.7 kcal/mol,

CASPT2) is larger than that of the diatomic CP molecule (119.6 kcal/mol, Table 4). These

unexpected results can be understood from the WBI and the NBO interaction energy analysis.

From the WBI analysis, there is a rather large 1,3-bonding interaction between the B and P atoms

(0.14) even though their atomic separation is 3.067 Å (DFT). As shown in Table 6, the NBO

stabilization energy ("2e-stabilization") between the C-P bonding π orbitals and empty p orbitals

on boron is 28.5 kcal/mol. In addition, the lone-pair electron donations from the B atom to the

C-P σ^* orbital and from the P atom to the B-C σ^* orbital is stabilizing by 14.3 kcal/mol and 16.5

kcal/mol, respectively. Thus, breaking the B-C bond in BCP also breaks the B···P bonding

interaction.

Table 6.　　　NBO stabilization energies associated with electron delocalization (kcal/mol) at the DFT level

Donor	Acceptor	Energy
π_x (C-P)	p_x (B)	13.9
π_y (C-P)	p_y (B)	14.6
σ (B)	σ^* (C-P)	14.3
σ (P)	σ^* (B-C)	16.5

Calculated heats of formation are compared with experimental values in Table 7. In the JANAF table[48] and NIST webbook,[49] the heat of formation of BC at 0K is given as 196±10 kcal/mol based on the old bond dissociation of BC (105±10 kcal/mol) and heat of formation of boron (132.6±2.9 kcal/mol). Using the newer experimental bond dissociation energy of BC (D_e = 102.2 kcal/mol)[20] with a ZPC correction of 1.7 kcal/mol and a more recent heat of formation of boron (136.2±0.2 kcal/mol),[43] we obtained a heat of formation of BC at 0K as 206±1 kcal/mol, which is in much better agreement with our best results (205.3 kcal/mol, CASPT2 level). DFT and G3B3 results are also in good agreement.

Previous studies have reported a disagreement between theory and experiment for the heat of formation of CP.[26-28] The calculated ΔH_f^o (0K) for CP of 124.1 kcal/mol (DFT), 127.3 kcal/mol (CASPT2), and 121.0 kcal/mol (G3B3) are in good agreement with the best computational heat of formation (124±2). The variation between CASPT2 and G3B3 for the heats of formation (0K) of CP (6.3 kcal/mol) and BP (5.7 kcal/mol) can be attributed largely to the empirical higher-level correction (HLC) in the G3B3 method.

The heat of formation of **S1** was calculated in two ways; directly from atoms (B + C + P→BCP), and averaging the heats of formation calculated from reactions shown in Table 8 using reference heats of formation of reactants. The two methods give similar results at the DFT

Table 7.   Heats of formation (kcal/mol) of ground state diatomic fragments and **S1**

Species	ΔH_f^o 0K				ΔH_f^o 298K		
	DFT	CASPT2	G3B3	exptl	DFT	CASPT2	G3B3
B				136.2±0.2[a]			
C				169.98±0.1[a]			
P				75.4±0.2[a]			
BC	204.5	205.3	203.5	206±1[b]	206.1	206.8	205.0
CP	124.1	127.3	121.0	124±2[c]	124.6	127.9	121.5
BP	131.3	140.2	134.5		131.9	140.7	135.0
BCP	144.5	151.9	140.9		145.8	153.1	142.1
BCP[d]	145.3	150.5	143.6		146.9	152.2	145.2

[a]   Reference 43.

[b]   Revised based on Tzeli and Marvridis' D_e and heats of formation of boron and carbon from Ref. 43.

[c]   References 26-28.

[d]   Averaged value. See Table 8.

Table 8.   Heats of formation (kcal/mol) of **S1** at 0K and 298K by different reactions

reacction	ΔH_f^o 0K			ΔH_f^o 298K		
	DFT	CASPT2	G3B3	DFT	CASPT2	G3B3
B+C+P → BCP	144.5	151.9	140.9	145.8	153.1	142.1
BC+P → BCP	146.0	152.6	143.4	148.6	155.1	145.7
B+CP →BCP	144.5	148.5	143.9	146.1	150.1	144.2
BC+CP →BCP+C	146.0	149.2	146.4	147.0	150.3	148.6
Average[a]	145.3±0.8	150.5±1.9	143.6±2.2	146.9±1.2	152.2±2.4	145.2±2.7

[a]   Error is obtained at 95% confidence interval.

and CASPT2 levels, but the G3B3 results show more variation. Our best estimate of ΔH_f^o (0K) of BCP ($^1\Sigma^+$) is 150.5±2 kcal/mol at the CASPT2 level.

We note that all three linear triplet species (**T1**, **T6**, and **T34**) have a degenerate electronic state ($^3\Pi$), and so are Renner-Teller species.[38] The vibrational frequencies of the linear

Table 9.   Vibrational Frequencies (cm^{-1}) and Renner-Teller Constants of Triplet Linear
           Species

Isomer	State	Level	π_x	π_y	σ_1	σ_2	$|\varepsilon|^a$
T1	$^3\Pi$ ($^3B_1$)	DFT	314.5	225.9	859.6	1577.7	0.319
		CAS	326.3	231.3	826.1	1444.0	0.331
T6	$^3\Pi$ ($^3B_1$)	DFT	273.7	206.7	683.6	1455.4	0.274
		CAS	265.0	198.8	671.6	1379.2	0.280
T34	$^3\Pi$ ($^3B_1$)	DFT	-82.1	-149.5	787.4	940.5	0.537
		CAS	-54.8	-142.0	723.2	937.0	0.740

a   Calculated by using the equation $\varepsilon = \{(\omega^+)^2-(\omega^-)^2\}/\{(\omega^+)^2+(\omega^-)^2\}$ in Ref. 51.

Table 10.   Calculated Vibrational Frequencies (cm^{-1}) and IR intensities (km/mol) of **S1**, **S2**,
            T1 and **T2**^{a}

	S1		S2		T1		T2	
	DFT	CAS	DFT	CAS	DFT	CAS	DFT	CAS
ν_1	110.4	180.7	606.6	645.6	225.9	231.3	590.6	594.9
	(12.1)	(3.5)	(21.7)	(75.2)	(5.9)	(3.5)	(19.8)	(15.2)
ν_2	110.6	180.7	929.6	885.9	314.5	326.3	932.3	892.8
	(12.0)	(3.5)	(21.7)	(40.0)	(16.1)	(11.2)	(8.8)	(7.3)
ν_3	750.8	714.6	1308.4	1350.0	859.6	826.1	1243.8	1193.2
	(129.2)	(122.7)	(16.3)	(16.4)	(0.3)	(0.6)	(10.2)	(7.5)
ν_4	1558.6	1466.8			1577.7	1444.0		
	(408.0)	(341.6)			(52.1)	(15.2)		

a   IR intensities are given in parentheses.

triplet species were calculated at the DFT and CAS levels in order to determine the nature of the

π bending modes (Table 9). While a more sophisticated study of the potential energy surface is

required for a full analysis of the Renner-Teller effect, we note that DFT and CAS give similar

results for the π bending modes. Both **T1** and **T6** are RT Type A (i.e. the π modes are different

and real)[50] with good agreement between DFT and CAS on the ε parameter (see Table 9). The

linear triplet **T34** is an RT Type D (i.e. both π modes are different and imaginary) with less

agreement on the ε value (0.54 DFT and 0.74 CAS). At the CASPT2 level there is an indication

that **T34** may actually be an RT Type C species (i.e. one π real mode and one π imaginary mode).

At the CAS level, **T34** is a transition state between **T3** (^{3}A') and **T4** (^{3}A") while at the CASPT2

level, the energy order is **T3**, **T34**, **T4** (i.e. **T34** is intermediate in energy to **T3** and **T4**). Thus,

we expect that dynamic electron correlation may have an important effect around this part of the

PES. To clarify this disagreement, we performed a series of CASPT2/ANO-L geometry

optimizations[52] for the different electronic states (^{3}A', ^{3}A", and $^3\Pi$) of **T34** and found that a

slightly bent ^{3}A' state is higher in energy than linear $^3\Pi$ state and a slightly bent ^{3}A" state is lower

in energy than $^3\Pi$; thereby confirming that **T34** must be an RT Type C species.

We report the vibrational frequencies and IR intensities in Table 10 for **S1**, **S2**, **T1** and

T2 calculated at the DFT and the CAS levels. These are the lowest energy species on the BCP

potential energy surfaces and may be observable in a low-temperature matrix. The most likely

species for observation is **S1** with quite intense BC and CP IR stretching frequencies.

2.4 Conclusions

On the BCP PES, three singlet and six triplet minima were found. The singlet linear BCP

(**S1**, $^1\Sigma^+$) is the global minimum while both the triplet triangular **T2** (^{3}A') and the triplet linear **T1**

are about 16 kcal/mol higher in energy. Rearrangements of triplets on the ^{3}A' and ^{3}A" PES can

take place by two mechanisms, either by going through a linear species of $^3\Pi$ symmetry where

the ^{3}A' and ^{3}A" states are degenerate or by going through a conical intersection. On the singlet

surface, the lowest energy pathways involve a B-C core with the phosphorus atom revolving

around on the A' surface **S1**→**S2**→**S3** or on the A" surface **S1**→**S3**.

50

Calculation of thermodynamic data at the DFT, CASPT2, and G3B3 levels are in good agreement with each other and with experimental values. The B-C and C-P bond dissociation energies (D_0) in B-C-P are 111.7 and 128.9 kcal/mol by CASPT2, respectively, which are larger that the BDE in the BC and CP diatomics, 100.9 and 118.1 kcal/mol, respectively. The stronger B-C and C-P bonds in BCP are due to stabilizing 1,3-interactions between the boron and phosphorus atoms. The calculated heat of formation (ΔH_f^o) of BCP ($^1\Sigma^+$) is 150.5±2 kcal/mol at the CASPT2 level. The absence of other low-energy unimolecular reactions suggests that BCP might be observed under appropriate conditions. Three Renner-Teller species among BCP isomers are discussed. Two of them (**T1** and **T6**) are classified as a Type A Renner-Teller species and the other one (**T34**) is classified as a Type D or C Renner-Teller species. In analogy with the BCN monomer and BCN polymeric materials, we hope that this study of the BCP monomer may contribute to its discovery or to the search for BCP polymer materials. To this end, studies are underway of polymers based upon the BCP monomer unit.

2.5 References

(1)   Aoki, K.; Tanaka, S.; Tomitani, Y.; Yuda, M.; Shimada, M.; Oda, K. *Chem. Lett.* **2002**, 112.

(2)   Kawano, T.; Kawaguchi, M.; Okamoto, Y.; Enomoto, H.; Bando H. *Solid State Sciences* **2002**, *4*, 1521.

(3)   Langenhorst, F.; Solozhenko, V. L. *Phys. Chem. Chem. Phys.* **2002**, *4*, 5183.

(4)   Ahn, J. Y.; Yoon, S. F.; Zhang, Q.; Gan, R. B.; Chew, K.; Yu, M. B.; Bai, X. D.; Wang, E. G. *Appl. Phys. Lett.* **2000**, *77*, 1949.

(5)   Gago, R.; Jimenez, I.; Agulló-Rueda, F.; Albella, J. M.; Czigány, Z.; Hultman, L. *J. Appl. Phys.* **2002**, *92*, 5177.

(6)   Miyamoto, Y.; Rubio, A.; Cohen, M. L.; Louie, S. G. *Phys. Rev. B* **1994**, *50*, 4976.

(7)   Thomson, C. *J. Chem. Phys.* **1973**, *58*, 216.

(8)   Martin, J. M. L.; Tayler, P. R. *J. Phys. Chem.* **1994**, *98*, 6105.

(9)   Lanzisera, D. V.; Andrews, L. *J. Phys. Chem. A* **1997**, *101*, 9660.

(10)   Lanzisera, D. V.; Andrews, L.; Taylor, P. R. *J. Phys. Chem. A* **1997**, *101*, 7134.

(11)   Verhaegen, D. G.; Stafford, F. E.; Ackerman, M.; Drowart, J. *Nature* **1962**, *193*, 1280.

(12)   Verhaegen, D. G.; Stafford, F. E.; Drowart, J. *J. Chem. Phys.* **1964**, *40*, 1662.

(13)   Kuoba, J. E.; Öhrn, Y. *J. Chem. Phys.* **1970**, *53*, 3923.

(14)   Fernando, W. T. M. L.; O'Brien, L. C.; Bernath, P. F. *J. Chem. Phys.* **1990**, *93*, 8482.

(15)   Wyss, M.; Grutter, M.; Maier, J. P. *J. Phys. Chem. A.* **1998**, *102*, 9106.

(16)   Hirsch, G.; Buenker, R. J. *J. Chem. Phys.* **1987**, *87*, 6004.

(17)   Knight, L. B., Jr.; Cobranchi, S. T.; Petty, J. T.; Earl, E.; Feller, D.; Davidson, E. R. *J. Chem. Phys.* **1989**, *90*, 690.

(18)   Oliphant, N.; Adamowicz, L. *Chem. Phys. Lett.* **1990**, *168*, 126.

(19)   Martin, J. M. L.; Taylor, P. R. *J. Chem. Phys.* **1994**, *100*, 9002.

(20)   Tzeli, D.; Mavridis, A. *J. Phys. Chem. A* **2001**, *105*, 1175.

(21)   Kumashiro, Y.; Sato, K.; Chiba, S.; Yamada, S.; Tanaka, D.; Hyodo, K.; Yokoyama, T.; Hirata, K. *J. Solid State Chem.* **2000**, *154*, 39.

(22)   Ferhat, M.; Zaoui, A.; Certier, M.; Aourag, H. *Physica B* **1998**, *252*, 229.

(23)   Rodríguez-Hernández, P.; González-Diaz, M.; Muñoz, A. *Phys. Rev. B* **1995**, *51*, 14705.

(24)   *Zaoui, A.; Hassan, F E. H. J. Phys.: Condens. Matter* **2001**, *13*, 253.

(25)   (a) de Brouckère, G.; Feller, D. *J. Phys. B: At. Mol. Opt. Phys.* **1996**, *29*, 5283. (b) Fast, P. L.; Sánchez, M.; Truhlar, D. G. *J. Chem. Phys.* **1999**, *111*, 2921.

(26)   Fleming, P. E.; Lee, E. P. F.; Wright, T. G. *Chem. Phys. Lett.* **2000**, *332*, 199.

(27)   Kwon, O.; McKee, M. L. *J. Phys. Chem. A* **2001**, *105*, 478.

(28)   Hajgató, B.; Pham-Tran, N.; Veszprémi, T.; Nguyen, M. T. *Phys. Chem. Chem. Phys.* **2001**, *3*, 5158.

(29)   Joo, H; McKee, M. L. *J. phys. chem. A* **2004**, *108*, 1851.

(30)   *Gaussian 98 (Revision A.11),* Frisch, M. J.; Trucks, G. W.; Schlegel, H. B.; Scuseria, G. E.; Robb, M. A.; Cheeseman, J. R.; Zakrzewski, V. G.; Montgomery, J. A., Jr.; Stratmann, R. E.; Burant, J. C.; Dapprich, S.; Millam, J. M.; Daniels, A. D.; Kudin, K. N.; Strain, M. C.; Farkas, O.; Tomasi, J.; Barone, V.; Cossi, M.; Cammi, R.; Mennucci, B.; Pomelli, C.; Adamo, C.; Clifford, S.; Ochterski, J.; Petersson, G. A.; Ayala, P. Y.; Cui, Q.; Morokuma, K.; Salvador, P.; Dannenberg, J. J.; Malick, D. K.; Rabuck, A. D.; Raghavachari, K.; Foresman, J. B.; Cioslowski, J.; Ortiz, J. V.; Baboul, A. G.; Stefanov, B. B.; Liu, G.; Liashenko, A.; Piskorz, P.; Komaromi, I.; Gomperts, R.; Martin, R. L.; Fox, D. J.; Keith, T.; Al-Laham, M. A.; Peng, C. Y.; Nanayakkara, A.; Challacombe, M.; Gill, P. M. W.; Johnson, B.; Chen, W.; Wong, M. W.; Andres, J. L.; Gonzalez, C.; Head-Gordon, M.; Replogle, E. S.; Pople, J. A. Gaussian, Inc., Pittsburgh PA, 2001.

(31)   (a) Becke, A. D. *J. Chem. Phys.* **1993**, *98*, 5648. (b) Lee, C.; Yang, W.; Parr, R. G. *Phy.*

         Rev. B **1988**, *37*, 785. (c) Miehlich, B.; Savin, A.; Stoll, H.; Preuss, H. *Chem. Phys. Lett.*

         1989, *157*, 200.

(32)   *GAMESS,* Schmidt, M. W.; Baldridge, K. K.; Boatz, J. A.; Elbert, S. T.; Gordon, M. S.;

         Jensen, J. J.; Koseki, S.; Matsunaga, N.; Nguyen, K. A.; Su, S.; Windus, T. L.; Dupuis,

         M.; Montgomery, J. A. *J. Comput. Chem.* **1993**, *14*, 1347.

(33)   Roos, B. O. "The complete active space self-consistent field method and its applications

         in electronic structure calculations" In: Lawley, K. P., Ed. *Advances in Chemical*

         Physics; Ab Initio Methods in Quantum Chemistry-II; John Wiley & Sons: Chichester,

         UK, 1987.

(34)   *MOLCAS* Version 5.4, Andersson, K.; Barysz, M.; Bernhardsson, A.; Blomberg, M. R.

         A.; Cooper, D. L.; Fülscher, M. P.; de Graaf, C.; Hess, B. A.; Karlström, G.; Lindh, R.;

         Malmqvist, P.-Å.; Nakajima, T.; Neogrády, P.; Olsen, J.; Roos, B. O.; Schimmelpfennig,

         B.; Schütz, M.; Seijo, L.; Serrano-Andrés, L.; Siegbahn, P. E. M.; Stålring, J.;

         Thorsteinsson, T.; Veryazov, V.; Widmark, P.-O.; Lund University, Sweden, 2002.

(35)   (a) Roos, B. O.; Andersson, K.; Fülscher, M. P.; Malmqvist, P.-Å.; Serrano-Andrés, L.;

         Pierloot, K.; Merchán, M. "Multiconfigurational perturbation theory: Applications in

         electronic spectroscopy" In: Prigogine, I; Rice, S. A., Ed. *Advances in Chemical Physics:*

         New Methods in Computational Quantum Mechanics; John Wiley & Sons: New York,

         1995. (b) Andersson, K.; Malmqvist, P.-Å.; Roos, B. O.; Sadlej, A. J.; Wolinski, K. *J.*

         Phys. Chem. **1990**, *94*, 5483. (c) Andersson, K.; Malmqvist, P.-Å.; Roos, B. O. *J. Phys.*

         Chem. **1992**, *96*, 1218.

(36)   (a) Krishnan, R.; Binkley, J. S.; Seeger, R.; Pople, J. A. *J. Chem. Phys.* **1980**, *72*, 650.

         (b) McLean, A. D.; Chandler, G. S. *J. Chem. Phys.* **1980**, *72*, 5639. (c) Clark, T.;

         Chandrasekhar, J.; Spitznagel, G. W.; Schleyer, P. v. R. *J. Comp. Chem.* **1983**, *4*, 294.

(37)   (a) Roos, B. O.; Andersson, K. *Chem. Phys. Lett.* **1995**, *245*, 215. (b) Roos, B. O.;

Andersson, K.; Fülscher, M. P.; Serrano-Andrés, L.; Pierloot, K.; Merchán, M.; Molina,

V. *THEOCHEM* **1996**, *388*, 257.

(38)   *MOLDEN,* Schaftenaar, G.; Noordik, J. H. *J. Comput.-Aided Mol. Design*, **2000**, *14*, 123.

(38)   (a) Renner, R. *Z. Phys.* **1934**, *92*, 172. (b) Herzberg, G. *Molecular Spectra and*

Molecular Structure III. Electronic Spectra and Electronic Structure of Polyatomic

Molecules; Krieger: Malabara, FL, 1991.

(40)   (a) Widmark, P. O.; Malmqvist, P.-Å.; Roos, B. O. *Theor. Chim. Acta* **1990**, *77*, 291. (b)

Widmark, P. O.; Malmqvist, P.-Å.; Roos, B. O. *Theor. Chim. Acta* **1991**, *79*, 419.

(41)   Reed, A.; Curtiss, L.A.; Weinhold, F. *Chem. Rev.* **1988**, *88*, 899.

(42)   Wiberg, K. B. *Tetrahedron* **1968**, *24*, 1083.

(43)   (a) Ochterski, J. W. Gaussian White Paper " Thermochemistry in Gaussian"

http://www.gaussian.com/g_whitepap/thermo.htm (b) Curtiss, L. A.; Raghavachari, K;

Redfern, P. C.; Pople, J. A. *J. Chem. Phys.* **1997**, *106*, 1063.

(44)   (a) Curtiss, L. A.; Raghavachari, K.; Redfern, P. C.; Rassolov, V.; Pople, J. A. *J. Chem*

Phys. **1998**, *109*, 7764. (b) Baboul, A. G.; Curtiss, L. A.; Redfern, P. C.; Raghavachari,

K. *J. Chem. Phys.* **1999**, *110*, 7650.

(45)   (a) Boldyrev, A. I.; Simons, J. *J. Chem. Phys.* **1993**, *97*, 6149. (b) Miguel, B.; Omar, S.;

Mori-Sánchez, P.; García de la Vega, J. M. *Chem. Phys. Lett.* **2003**, *381*, 720.

(46)   Huber, K. P.; Herzberg, G. "Molecular Spectra and Molecular Structure. IV. Constants of

Diatomic Molecules", New York: Van Nostrand, 1979.

(47)   We calculated $\Delta E(HLC)$ as found in reference 43a. The result $\Delta\Delta E(HLC)$ for diatomic

fragments are as follow; BC: 3.6, CP:6.4, BP: 5.0 (kcal/mol). These corrections increase

the bond dissociation energies computed by G3B3 method. When this factor is taken into

account the CASPT2 and G3B3 methods give very similar bond dissociation energies.

(48)   Chase, M. W., Jr. *NIST-JANAF Thermochemical Tables, 4th Ed.; J. Phys. Chem. Ref. Data* **1998**, Monograph 9.

(49)   NIST Chemistry Webbook Site http://webbook.nist.gov/chemistry .

(50)   Lee, T. J.; Fox, D. J.; Schaefer, H. F.; Pitzer, R. M. *J. Chem. Phys.* **1984**, *81*, 356.

(51)   Brown, S. T.; Yamaguchi, Y.; Schaefer, H. F. *J. Phys. Chem. A* **2000**, *104*, 3603.

(52)   For a discussion of CASPT2 optimized geometries see: Page, C. S.; Olivucci, M. *J. Comp. Chem.* **2003**, *24*, 298.

CHAPTER 3

AN EXPERIMENTAL AND THEORETICAL EVALUATION OF THE REACTIONS OF

SILVER HYPONITRITE WITH PHOSPHORUS HALIDES. IN SEARCH OF THE

ELUSIVE PHOSPHORUS-CONTAINING HYPONITRITES

3.1 Introduction

The existence of organic hyponitrites is well documented in the chemical literature. These hyponitrites have been synthesized by reactions of appropriate organic halides and silver hyponitrite.[1-3] The hyponitrites are a source of alkoxy or aryloxy radicals. The geometries of alkyl hyponitrites are *trans* based on vibrational spectroscopy,[4,5] dipole moment measurements,[6] and low temperature X-ray crystallography.[7] Decomposition is thought to occur by homolytic scission with loss of N_2.[8-10]

The presence of the N=N bond has been confirmed by ultraviolet spectrum.[11] The *trans* isomer has been found to be the product obtained by usual preparative methods as confirmed by Raman[12-14] and infrared[15-17] spectroscopy. *Cis*-hyponitrous acid has been postulated as an unstable intermediate in the reaction of hydroxylamine and nitrous acid[18] and in the reduction of nitrous acid by europium(II).[19]

A number of alkali metal, alkaline earth metal, mercury, silver, and lead hyponitrites have been synthesized. Mercury and silver hyponitrites are known to have a *trans* configuration,[4] while sodium hyponitrite has been synthesized in both the *cis* and *trans* geometries.[20,21] Several transition metal hyponitrites have been prepared including the very interesting [Ni(dppf)N_2O_2],

[Pd(dppe)N$_2$O$_2$], and [Pt(dppf)N$_2$O$_2$] hyponitrites, all of which have *cis* hyponitrite geometries and decompose by unimolecular kinetics.[21,22]

Beck *et al.*[13] reported that the decomposition of triphenyltin hyponitrite, Ph$_3$SnON=NOSnPh$_3$, yielded N$_2$O and (Ph$_3$Sn)$_2$O. On the other hand, Wiberg *et al.*[14] prepared trimethylsilyl hyponitrite, Me$_3$SiON=NOSiMe$_3$, and reported that thermolysis gave N$_2$, trimethyl silanol, and hexamethyl disiloxane.

Phosphorus-containing hyponitrites are conspicuous by their absence in the chemical literature. Furthermore, no attempts to synthesize these potentially interesting molecules have been reported. This is in spite of the potential use of such hyponitrites to generate extremely interesting radicals (e.g., F$_2$PO, F$_2$PO$_2$, F$_2$P(S)O). This work deals with the attempts to prepare such hyponitrites by reaction with silver hyponitrite as shown in the equation below (eq 1):

$$2R_2P(Y)X + Ag_2N_2O_2 \rightarrow 2AgX + R_2P(Y)ON=NOP(Y)R_2 \tag{1}$$
(R=CH$_3$,F; Y=O,S; X=halide)
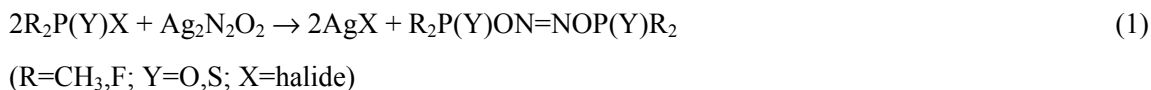
In the thermal decomposition of hyponitrites, the experimental evidence suggests that *trans* hyponitrites decompose to N$_2$ plus other products, while *cis* hyponitrites may decompose to N$_2$O plus other products.[23] A related issue is whether the decomposition is concerted (eq 2a) or stepwise (eq 2b).

$$RON=NOR \rightarrow 2RO\bullet + N_2 \tag{2a}$$
$$RON=NOR \rightarrow RO\bullet + \bullet N=NOR \rightarrow 2RO\bullet + N_2 \tag{2b}$$

Neuman and Bussey determined the activation volume of the *trans*–di-*t*-butyl hyponitrite decomposition and suggested the reaction follows the concerted pathway.[10] For *trans*

hyponitrites, structural and mechanistic studies are well established.[20,24] On the contrary, mechanistic studies on *cis* hyponitrites are rare.[22]

To understand the different chemical reactivities of *trans* and *cis* hyponitrites, theoretical calculations were carried out. No previous calculations have been reported on the structures, stabilities, or decomposition reaction pathways of phosphorus-containing hyponitrites. Hybrid density functional theory, B3LYP, has been applied to study the decomposition pathways of $XON=NOY$, $X,Y=PF_2,OPF_2$, to establish the probable reaction mechanisms leading to observed final products. This work has been published in Journal of Physical Chemistry A in 2005.[25]

3.2 Experimental[26]

Standard vacuum line techniques were used to purify and transfer all volatile substances. Non-volatile compounds were handled in a nitrogen-filled glove bag containing P_4O_{10} as a desiccant.

Infrared spectra were determined on a Perkin-Elmer 983 spectrophotometer. Liquids were examined as neat samples; solids were studied as Nujol and fluorolube mulls. [31]P and ^{1}H nmr spectra were obtained at 162 and 400 MHz on a Bruker AM 400 spectrometer. [31]P chemical shifts were measured relative to H_3PO_4 (85%, external), and ^{1}H relative to TMS (internal). Mass spectra were recorded on a Finnigan 3300 mass spectrometer equipped with a gas inlet system and a solid probe.

Gaseous reactants were obtained from Matheson. Toluene and benzene (dried over sodium) and acetonitrile (purified by distillation over phosphorus pentoxide and collected over molecular sieves) were obtained from Fisher. Thiophosphoryl chloride was obtained from Aldrich and distilled prior to use. Bromopentafluorobenzene was obtained from Columbia Organics and dried over 4A molecular sieves prior to use. Phosphorus trichloride was obtained from Matheson, Coleman & Bell and distilled prior to use. Silver hyponitrite was prepared by the

literature method.[27] $(CH_3)_2P(S)Br$,[28] $(CH_3)_2P(O)Cl$,[29] $(C_6F_5)_2PBr$,[30] $F_2P(O)Br$,[31a] and F_2PBr[31b] were prepared by literature methods.

The reaction of dimethylthiophosphinic bromide with silver hyponitrite in 2:1 ratio

$(CH_3)_2P(S)Br$ (0.462 g, 2.67 mmol) was placed in a 100 mL three-necked flask containing a magnetic stirring bar. Toluene (30 mL) was added to the flask to dissolve the bromide. Silver hyponitrite (0.382 g, 1.38 mmol) was placed in a thumb-shaped solid addition tube and added slowly over a period of 15 minutes at room temperature. The system was protected from light by wrapping the flask with aluminum foil. The collected gas (1.33 mmol) was shown to be N_2O by its infrared and mass spectra. The yellowish liquid was filtered off and the solvent was removed *in vacuo* to give 0.269 g of solid, identified as $(CH_3)_2P(S)OP(S)(CH_3)_2$ by its ^{31}P nmr and infrared spectrum.

Several low-temperature reactions were carried out to see if any hyponitrite, $(CH_3)_2P(S)ON=NO(S)P(CH_3)_2$, could be detected. In one of those reactions, 0.219 g (1.27 mmol) of dimethylthiophosphinic bromide was taken in a 100 mL flask as described in the previous reaction, using 25 mL of toluene and 0.205 g (0.74 mmol) silver hyponitrite. The reaction flask was placed in a dry-ice acetone slush bath to keep the reaction mixture at -78°C. The silver hyponitrite was then added slowly over a 10-minute period. After 20 minutes, no volatiles were observed. The reaction flask was then quickly transferred to a chlorobenzene-liquid nitrogen slush bath (-45°C). Again no gas was detected after 20 minutes. The reaction flask was then transferred to a carbon tetrachloride-liquid nitrogen slush bath (-23°C). After 20 minutes, 2 torr (V=396 mL) pressure was observed. The color of the reaction mixture did not change. The reaction flask was then transferred to an ice bath. After a while the pressure observed was 13 torr (V=396 mL). The reaction went to completion at this temperature. In the second batch, the reaction was monitored by ^{31}P nmr on a Bruker AM 400 instrument at –30°C, using 0.0981 g

(0.47 mmol) of the bromide. From the previous low-temperature reaction, it was thought that the reaction might have started well below –23°C. Therefore, the reactants were mixed at bromobenzene-liquid nitrogen temperature (-30°C). The amount of silver hyponitrite taken was 0.079 g (0.03 mmol). After mixing the reactants for 20 minutes, a 2 mL portion of the solution was transferred by a syringe into an nmr tube and the spectrum was recorded at –30°C. Two peaks were found at 66.0 ppm and 91.3 ppm. These peaks were assigned to dimethylthiophosphinic bromide and $(CH_3)_2P(S)OP(S)(CH_3)_2$, respectively.[32] The reaction was allowed to go for six hours. Again a 2 mL portion of the liquid from the flask was syringed out and the ^{31}P nmr spectrum was taken at -30°C. Only one peak was observed at 91.3 ppm, which corresponds to the phosphorus chemical shift in $(CH_3)_2P(S)OP(S)(CH_3)_2$.

The mass spectrum of the solid product showed the following peaks:

$M^+=[(CH_3)_2P(S)OP(S)(CH_3)_2^+]$ 202(44%); $(M-CH_3)^+$ 187(3%); $(M-HS)^+$ 169(27%); $(M-CH_3-S)^+$ 155(3%); $(CH_3)_2P(S)OH^+$ 110(7%); $(CH_3)_2PS^+$ 93(100%); $H_2C=PS^+$ 77(58%); PS^+ 63(45%); PO^+ 47(77%); PCH_2^+ 45(51%); CH_3^+ 15(41%). Mass spectrum of the gaseous product: N_2O^+ 44(100%); NO^+ 30(35%).

The infrared spectrum of the gaseous sample is given below (all values in cm^{-1}) N_2O: 2234(s), 2214(s), 1299(s), 1272(s).

Reaction of dimethylphosphinic chloride with silver hyponitrite in 2:1 ratio

Dimethylphosphinic chloride (0.331 g, 2.96 mmol) was dissolved in 20 mL toluene (Na dried) in a 100 mL three-necked flask equipped with a magnetic stirring bar. Silver hyponitrite (0.440 g, 1.60 mmol) was placed in a thumb-shaped tube with ground joint and fitted to the flask. The flask was then evacuated on the vacuum line. The entire flask including the thumb-shaped tube was wrapped with aluminum foil to protect the contents from light. Silver hyponitrite was then added to the solution over a period of 20 minutes. The heterogeneous mixture was stirred

for two hours at room temperature. The flask was then connected to the vacuum line and the gaseous product was collected (1.46 mmol) at -196°C. The gas was shown to be N_2O by infrared and mass spectrometry. The mixture in the three-necked flask was filtered and the solvent was evaporated from the filtrate under high vacuum. The solid recovered was 0.247 g (98% yield) based on the amount of $(CH_3)_2P(O)Cl$ reacted. The ^{31}P nmr of the solid run in toluene showed only one signal at 49.6 ppm. The mass spectrum of the compound $(CH_3)_2P(O)OP(O)(CH_3)_2$ was: M^+ peak not observed; $(CH_3)_2PO_2H^+$ 94(41%); $(CH_3)_2P(O)H_2^+$ 79(100%); HPO^+ 48(4%); H_2PO^+ 49(7%); PO_2^+ 63(3%); $(CH_3)_2P=O^+$ 77(5%). The mass spectrum and the infrared spectrum of the gas collected at -196°C is identical with that reported above. The infrared of the solid in Nujol showed the following peaks (all values in cm^{-1}): 1305(s)(P=O), 972(vs)(P-O-P, asym.), 871(s)(P-O-P, sym.), 723(m)(P-C).

Reaction of difluorophosphinic bromide with silver hyponitrite in 2:1 ratio

The reaction of difluorophosphinic bromide was performed in the absence of light. $F_2P(O)Br$ (9.20 mmol) was condensed into a Fisher-Porter tube charged with silver hyponitrite (1.701 g, 6.20 mmol). The mixture was warmed to room temperature and left for two hours. The product was passed through four traps at -78°C, -130°C, -160°C, and -196°C. The -78°C and -130°C traps each contained 4.40 mmol of gas with a liquid mixture of $F_2P(O)Br$ and $F_2P(O)OP(O)F_2$[33] (as indicated by infrared). There were no products in the -160°C trap. The -196°C trap contained 4.0 mmol of a gas identified as N_2O by its mass spectrum and infrared spectrum. The data are the same as that obtained for N_2O in previous reactions.

The infrared spectrum of the samples from the -78°C and -130°C traps showed the following absorptions (all values in cm^{-1}): 1425(s)(P=O) $F_2P(O)OP(O)F_2$; 1375(ms) $F_2P(O)Br$; 1325(s) $F_2P(O)Br$; 1075(vs)(POP asym. stretch) $F_2P(O)OP(O)F_2$; 993(s)(POP sym. stretch)

$F_2P(O)OP(O)F_2$; 976(vs) $F_2P(O)OP(O)F_2$; 942(vs) $F_2P(O)Br$; 899(s) $F_2P(O)OP(O)PF_2$; 885(vs)

$F_2P(O)Br$; 560(vs) $F_2P(O)Br$.

The mass spectra showed the following peaks for the gas in the -130°C trap: $F_2P(O)Br^+$

164(91%), 166(91%); $FP(O)Br^+$ 145(37%), 147(37%); F_3PO^+ 104(91%); PF_3^+ 88(21%); F_2PO^+

85(100%); PF^+ 50(35%); PO^+ 47(71%).

Reaction of bis(perfluorophenyl)bromophosphine and silver hyponitrite in 2:1 ratio

$(C_6F_5)_2PBr$ (1.171 g, 2.63 mmol) was dissolved in 25 mL benzene (Na dried) in a three-

necked flask. The arrangement and precautions were the same as the previous reactions. Silver

hyponitrite (0.376 g, 1.36 mmol) was added slowly over a period of 10 minutes and the mixture

was stirred for two hours at room temperature and then filtered. The amount of product,

recovered from the filtrate by removing the solvent *in vacuo*, was 0.956 g. The gas evolved (1.27

mmol) was N_2O, identified by mass spectral and infrared data. The ^{31}P nmr spectrum run in

benzene showed a multiplet (apparent nonet) at +93.4 ppm assigned to $(C_6F_5)_2POP(C_6F_5)_2$. The

mass spectrum of the white solid, $(C_6F_5)_4P_2O$, was: $(C_6F_5)_4P_2O^+$ 746(30%); $C_{24}F_{19}P_2O^+$ 727(3%);

$(C_6F_5)_3P_2O^+$ 579(11%); $(C_6F_5)_3P^+$ 532(25%); $(C_6F_5)_2PO^+$ 381(92%); $(C_6F_5)_2P^+$ 365(50%); $C_{12}F_8^+$

296(100%); $C_{12}F_7^+$ 277(11%); $C_6F_5PF^+$ 217(58%); $C_6F_5P^+$ 198(22%); $C_6F_4P^+$ 179(15%); $C_6F_4^+$

148(20%); $C_6F_3^+$ 129(95%); $C_5F_3^+$ 117(35%); CF_3^+ 69(100%); PO^+ 47(8%). The infrared

spectrum showed two intense peaks at 909 and 640 cm^{-1} (P-O-P asym. and sym.). The absorption

at 1465(s) and 1102(s) cm^{-1} are P-C stretching modes, while the bands at 1377(s), 1303(s), and

1232(s) cm^{-1} are C-F stretching bands. The N_2O gas was identified as previously described.

Reaction of Bromodifluorophosphine and silver hyponitrite in 2:1 ratio

Silver hyponitrite (1.701 g, 6.2 mmol) was placed in a Fisher-Porter tube wrapped in

aluminum foil. F_2PBr gas (12.4 mmol) was condensed into the tube. The mixture was warmed to

room temperature and kept for two hours. The reactor contents were passed through -90°C, -130°C, -160°C, and -196°C traps. Nothing was collected in the -90°C trap. The -130°C trap contained 5.4 mmol of gas. The infrared spectrum showed it to be a mixture of F_2POPF_2[34] and F_2PBr. The -160°C trap stopped 4.1 mmol of gas which was identified as N_2O from its infrared and mass spectrum. The mass spectrum of the products collected in the -130°C trap was: $F_2POPF_2^+$ 154(60%); F_2POPF^+ 135(23%); F_3PO^+ 104(13%); F_2PO^+ 85(33%); PF_2^+ 69(29%); PF^+ 50(65%); PO^+ 47(49%); P^+ 31(4%); F_2PBr^+ 148(96%); F_2PBr^+ 150(100%); $FPBr^+$ 129(29%); $FPBr^+$ 131(23%). The mass spectrum of the -160°C trap gas was: $F_2POPF_2^+$ 154(37%); F_3PO^+ 104(33%); F_2PO^+ 85(41%); PF_2^+ 69(100%); PF^+ 50(31%); PO^+ 47(46%); N_2O^+ 44(85%).

3.3 Computational methods

The decomposition of the three phosphorus-containing hyponitrite species listed in Scheme 1 (**A**, **B**, **C**), where **A** and **C** were the synthetic targets of the experimental study, were considered in our computational study (numbering system is given for **C**). Hyponitrite **B** was included to examine the effects of asymmetric oxygen substitution on phosphorus. The Gaussian03 program package[35] running on a Beowolf cluster was used for all calculations. The hybrid B3LYP combination of exchange and correlation functions, which has been shown to yield good results for a number of inorganic systems,[36] was used throughout. For geometry optimization, the 6-31+G(d) basis set was used for F, N, O, and P atoms and the LANL2DZ[37] effective core potential (ECP) and basis set was used for the Ag^+ ion. For transition states with strong biradical character we applied the unrestricted broken-symmetry UB3LYP method with the same basis set. At every optimized geometry, frequency calculations were made using the same level of theory to characterize the stationary points as minima (0 imaginary frequencies) or transition states (1 imaginary frequency). The transition vector of every TS structure was animated with the Molden program.[38] If necessary, intrinsic reaction coordinates (IRC) were
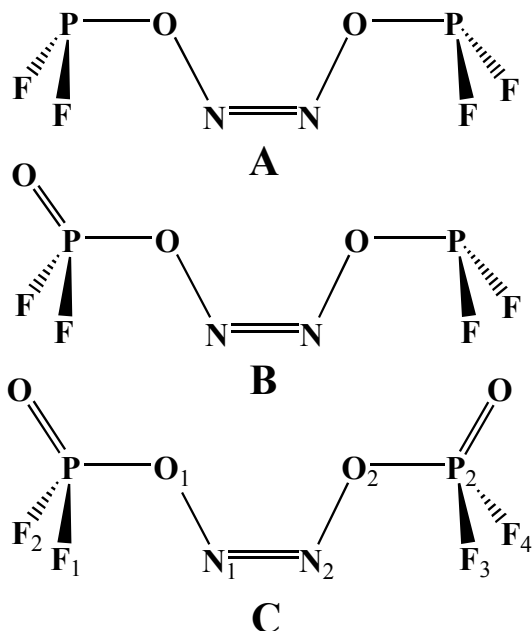
Scheme 1

calculated to connect a TS to the corresponding minima. After the reaction profile was

constructed, single-point calculations were performed on stationary points with the larger

6-311+G(2df) basis set for F, N, O and P and the standard SDD[39] effective core potential and

basis set for Ag. For convenience, "SBS" is used to indicate B3LYP/6-31+G(d)+LANL2DZ and

"LBS" to indicate B3LYP/6-311+G(2df)+SDD. The natural population analysis (NPA) charges

were obtained by using the NBO[40] program implemented in the Gaussian program.

The reactions of F_2PBr and $F_2P(O)Br$ with AgON=NOAg were carried out in neat liquid.

In order to estimate the effect of medium, single-point energy calculations were carried out using

the conductor polarizable continuum model (CPCM)[41] at the B3LYP/6-311+G(2df) level with the

dielectric constant of THF. While the dielectric constants of F_2PBr and $F_2P(O)Br$ are unknown,

the dielectric constant of Cl_3PO is known to be 14.0 which is reasonably close to THF (7.58).[42]

The structures and geometrical parameters of $F_2PON=NOPF_2$ (**A**), $F_2P(O)ON=NOPF_2$ (**B**), and $F_2P(O)ON=NOP(O)F_2$ (**C**) species are given in Figure 1. Relative energies, enthalpies, and free energies (kcal/mol) at the B3LYP/LBS//B3LYP/SBS level of theory are given for **A** in Table 1, for **B** in Table 2, and for **C** in Table 3. A table of spin-squared values, absolute energies, and free energies of solvation in THF is available as supporting information (Table S1) as well as Cartesian coordinates of all structures in Tables 1-3 and 5 (Table S2). Reaction profiles of free energies (kcal/mol) at 298K at the B3LYP/LBS//B3LYP/SBS level of theory are provided for **A** (Figure 2), **B** (Figure 3), and **C** (Figure 4).

3.4 Results and Discussion:

The reactions of silver hyponitrite with $(CH_3)_2P(S)Br$, $(CH_3)_2P(O)Cl$, $F_2P(O)Br$ and F_2PBr have been evaluated as potential synthetic paths to the hyponitrites $R_2P(Y)ON=NOP(Y)R_2$ (Y=O,S; R=CH$_3$,F) and $R_2PON=NOPR_2$ (R=C$_6$F$_5$,F). In all cases the reactions were carried out in the absence of moisture and light (because silver hyponitrite is light-sensitive). The gaseous products were identified by infrared and mass spectra; the solids were identified by nmr, mass and infrared spectra. The results obtained in this series of reactions may be expressed by the following general equations (eq 3):

$$2R_2P(Y)X + AgON=NOAg \rightarrow 2AgX + N_2O + R_2P(Y)OP(Y)R_2 \qquad (3a)$$
(R=CH$_3$,F; Y=electron-pair,O,S; X=halide)

$$2R_2PX + AgON=NOAg \rightarrow 2AgX + N_2O + R_2POPR_2 \qquad (3b)$$
(R=C$_6$F$_5$,F; X=Br)
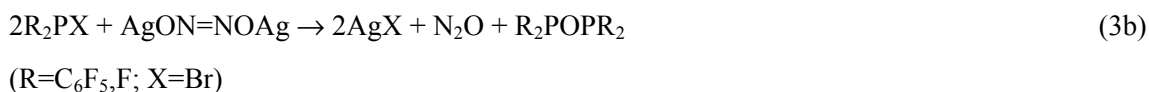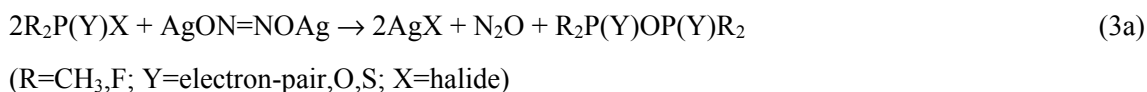
Thus, no hyponitrites were isolated from the above synthetic pathway even when reactions were carried out at low temperatures. In all cases, µ-oxo phosphorus-containing species were obtained.

66

The change in substituents from electron-releasing methyl groups to the highly electronegative F (eq 3a, R=CH$_3$,F) or from tri-coordinate phosphorus to pentavalent phosphorus, P=O or P=S (eq 3a, Y=electron-pair,O,S) did not change the reaction pathway. We had hoped that the postulated hyponitrites formed in these reactions might have a stability comparable to t-butyl hyponitrite. Since the stability of t-butyl hyponitrite has been attributed to its lack of an α-hydrogen,[2] we reasoned that the proposed hyponitrites of phosphorus might have comparable stability to t-butyl hyponitrite because they also lacked an α-hydrogen.

  Cis-hyponitrites are known to be less stable than *trans*-hyponitrites.[43,44] Therefore, the fact that we do not observe a phosphorus-containing hyponitrite might be due to an initially formed *cis*-hyponitrite (which decomposes) or to the rearrangement of the *trans*-hyponitrite to *cis*-hyponitrite under experimental conditions. It is interesting to note that the electronegative fluorine or less electronegative perfluorophenyl groups on the trivalent phosphorus did not result in an identifiable hyponitrite. To determine whether this might have a thermodynamic or kinetic origin, we turned to theoretical calculations.

  Optimized geometries for the hypothetical hyponitrites are shown in Figure 1 and natural population analysis (NPA) charges are given in Table 4. For all three molecules, the *cis* isomer has slightly shorter N=N bond lengths (about 0.007 Å) and longer N-O bond lengths which indicate less π delocalization in the *cis* compared to the *trans* isomer (Figure 1, **AC/AT**, **BC/BT**, **CC/CT**). As the phosphinyl (F$_2$P) groups in F$_2$PON=NOPF$_2$ are oxidized to phosphoryl (F$_2$P(O)) groups (**AC→CC**), the O-P bond lengths are shortened from 1.667 to 1.634 Å. The oxidation to phosphoryl groups makes these phosphorus atoms more positively charged (III→V) and leads to a strong bonding interaction between P$_1$ and O$_1$ (See Scheme 1 for numbering). Interestingly, in the unsymmetrical F$_2$P(O)ON=NOPF$_2$ (**BC**), the phosphoryl P$_1$-O$_1$ bond length is much shorter than the phosphinyl O$_2$-P$_2$ bond length (1.623 and 1.680 Å, respectively), while the
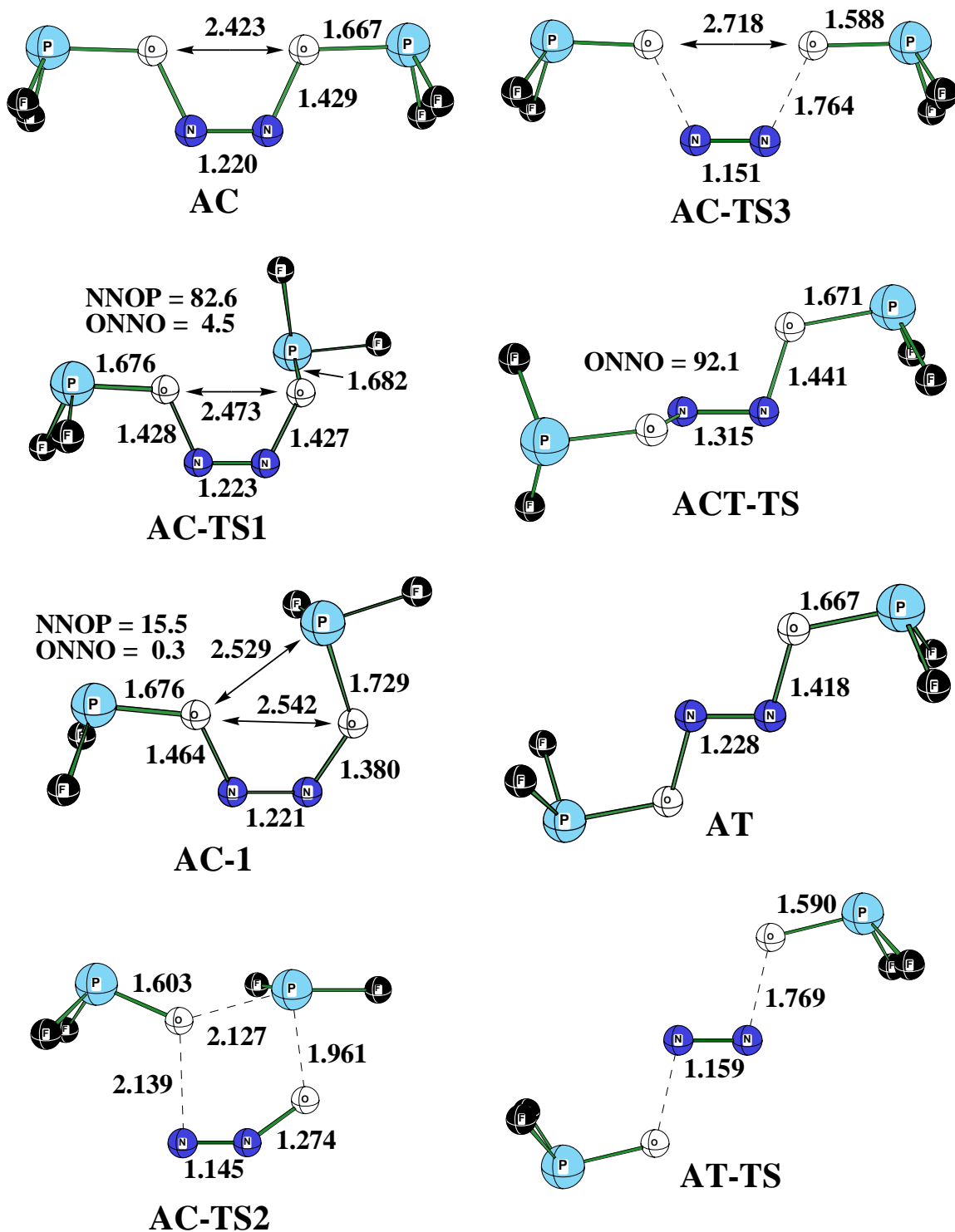
Figure 1. (A)   Calculated geometries for species on the following PES F$_2$PON=NOPF$_2$ (**A**) at the

B3LYP/SBS level.
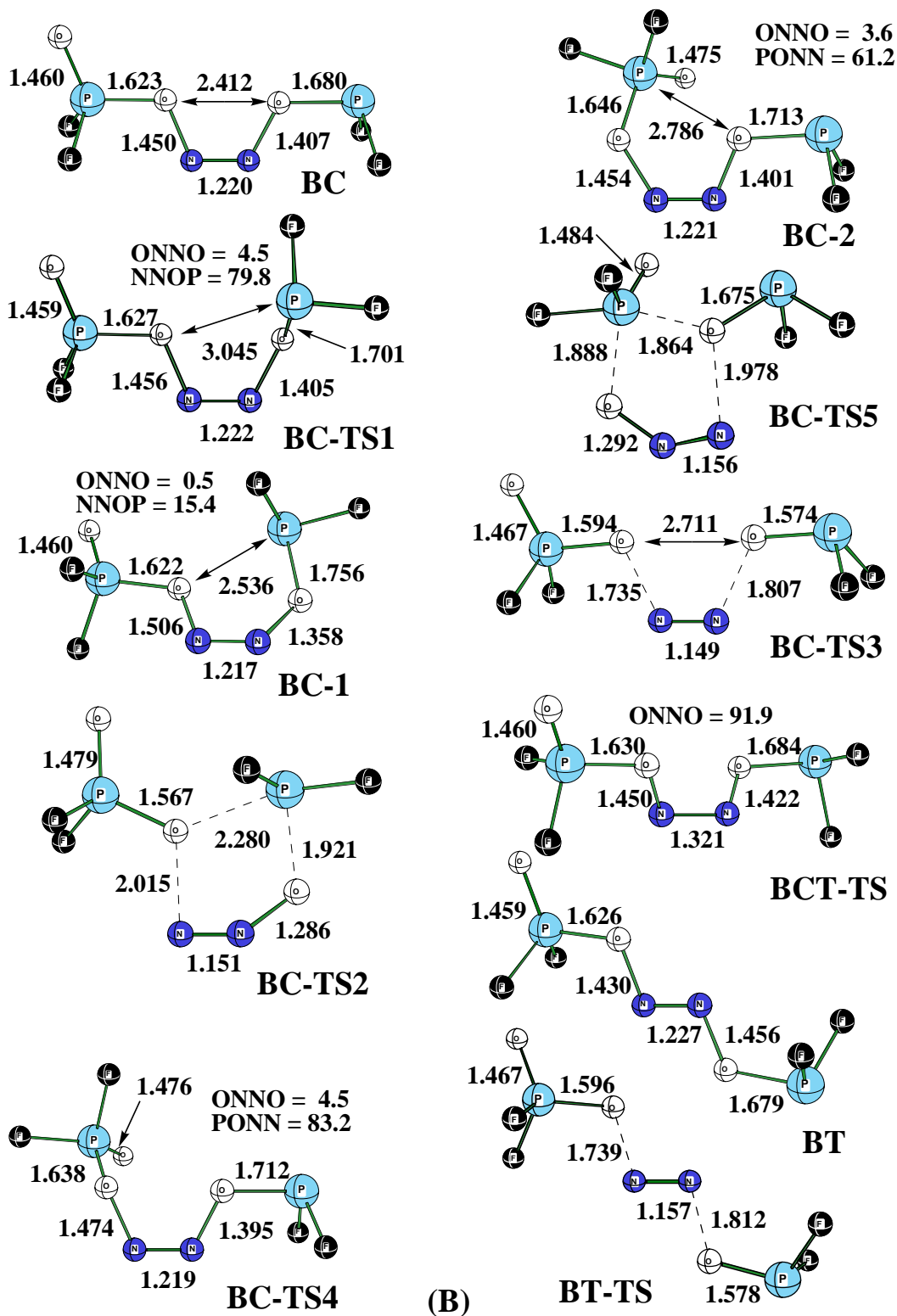
Figure 1. (B) Calculated geometries for species on the PES of $F_2P(O)ON=NOPF_2$ (**B**) at the

B3LYP/SBS level.
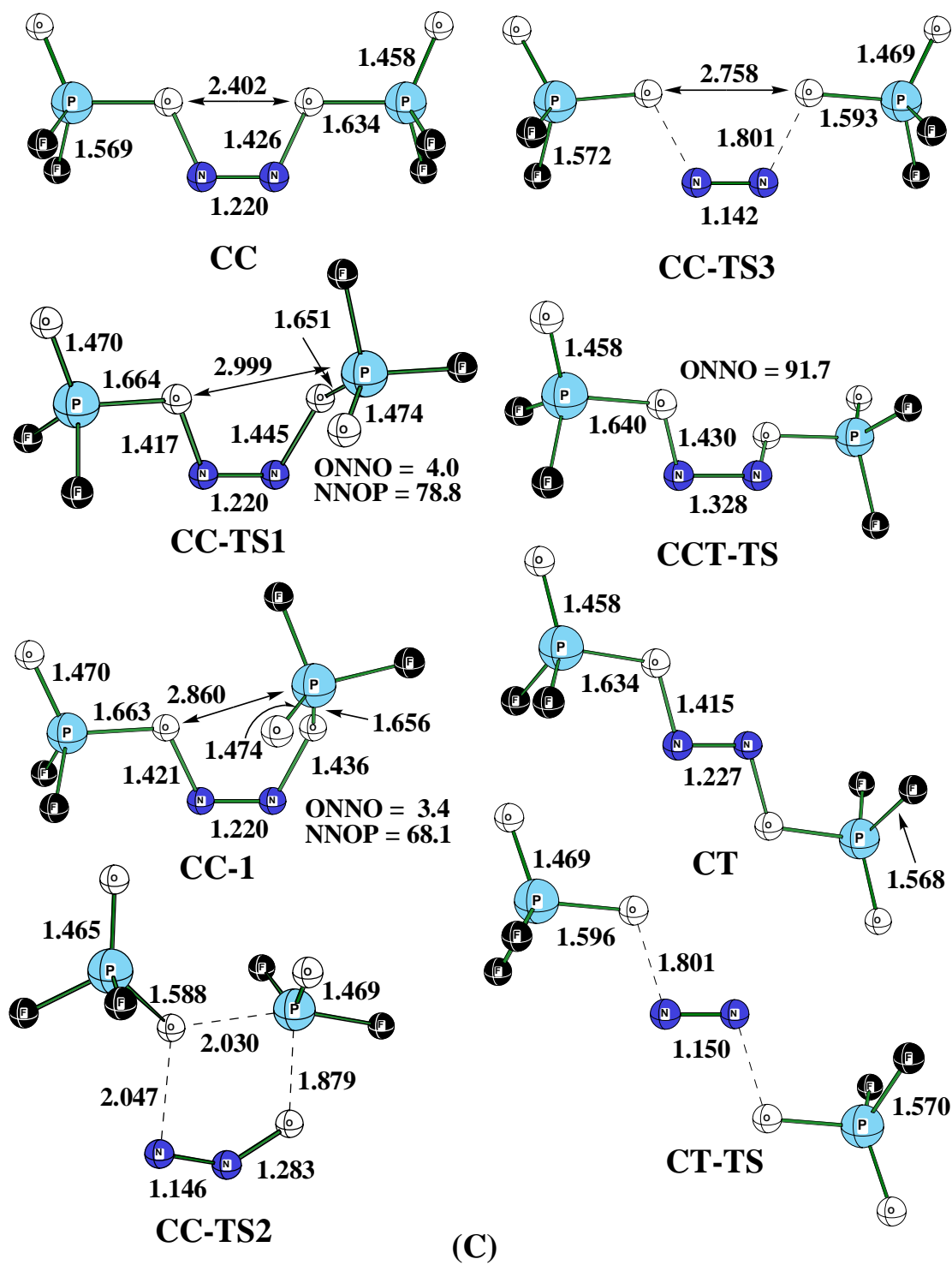
Figure 1. (C) Calculated geometries for species on the PES of $F_2P(O)ON=NOP(O)F_2$ (**C**) at the B3LYP/SBS level.

Table 1.   Relative Enthalpies and Free Energies (kcal/mol) on the Potential Energy Surface of $F_2PON=NOPF_2$ at the B3LYP/LBS//B3LYP/SBS Level

	ΔE_e	ΔH_{0K}	ΔH_{298K}	ΔG_{298K}	ΔG_{THF}[a]
AC	0.0	0.0	0.0	0.0	0.0
AC-1	6.0	5.7	5.8	5.7	6.0
AT	1.9	1.9	1.9	1.9	2.2
AC-TS1	6.8	6.6	6.1	7.0	7.5
AC-TS2	14.4	13.3	13.4	13.2	13.9
AC-TS3	11.5	9.1	9.7	7.8	9.3
AT-TS	15.5	13.1	13.9	12.1	13.1
ACT-TS	53.3	50.7	50.7	50.5	51.2
N_2+2OPF_2	-44.3	-47.3	-46.5	-69.2	-66.2
$N_2O+F_2POPF_2$	-47.4	-48.2	-47.7	-58.3	-55.8

a)   Including solvation free energy calculated by CPCM method in THF.

Table 2.   Relative Enthalpies and Free Energies (kcal/mol) on the Potential Energy Surface of $F_2P(O)ON=NOPF_2$ at the B3LYP/LBS//B3LYP/SBS Level

	ΔE_e	ΔH_{0K}	ΔH_{298K}	ΔG_{298K}	ΔG_{THF}[a]
BC	0.0	0.0	0.0	0.0	0.0
BC-1	6.1	5.8	5.8	6.0	6.6
BC-2[b]	8.5	8.2	8.3	8.3	7.5
BT	2.2	2.2	2.2	2.2	2.2
BC-TS1	7.4	7.1	6.6	7.4	7.9
BC-TS2	9.6	8.5	8.6	8.8	7.7
BC-TS3	14.5	11.9	12.5	10.5	10.9
BC-TS4[b]	8.3	8.0	7.5	8.8	7.8
BC-TS5	30.4	29.5	29.2	30.8	28.9
BT-TS	19.2	16.5	17.1	15.3	15.7
BCT-TS	54.0	51.5	51.5	51.2	49.9
$N_2+OPF_2+O_2PF_2$	-26.3	-30.4	-29.4	-51.7	-47.4
$N_2O+F_2POP(O)F_2$	-49.5	-50.2	-49.8	-60.9	-58.6

a)   Including solvation free energy calculated by CPCM method in THF.

b)   Geometry optimized at the B3LYP/cc-pVDZ level.

Table 3.   Relative Enthalpies and Free Energies (kcal/mol) on the Potential Energy Surface of $F_2(O)PON=NOP(O)F_2$ at the B3LYP/LBS//B3LYP/SBS Level

	ΔE_e	ΔH_{0K}	ΔH_{298K}	ΔG_{298K}	ΔG_{THF}[a]
CC	0.0	0.0	0.0	0.0	0.0
CC-1[b]	10.0	9.5	9.6	8.5	8.2
CT	2.0	1.9	2.0	1.9	2.1
CC-TS1[b]	9.7	9.1	8.7	9.4	9.3
CC-TS2	29.9	28.9	28.8	29.3	25.8
CC-TS3	19.5	16.5	17.2	15.1	15.3
CT-TS	24.7	21.5	22.2	19.9	16.3
CCT-TS	54.3	51.8	51.9	51.5	52.3
$N_2+2O_2PF_2$	-9.7	-15.0	-13.9	-36.7	-30.7
$N_2O+F_2P(O)OP(O)F_2$	-49.8	-50.5	-50.0	-61.7	-59.2

a)   Including solvation free energy calculated by CPCM method in THF.

b)   Geometry optimized at the B3LYP/cc-pVDZ level.

O_1-N_1 and N_2-O_2 bond lengths change in the opposite direction (1.450 and 1.407 Å, respectively) which suggests a resonance contribution from $P_1=O_1\ldots N_1=N_2=O_2\ldots P_2$.

The elimination of N_2O can occur after the phosphorus-containing group (F_2P or ($F_2P(O)$)) has rotated around the N-O bond. This allows interaction between a phosphorus center and a remote oxygen center (i.e. P_2 with O_1 in **AC-1**, **BC-1**, **CC-1** or P_1 with O_2 in **BC-2**). In **AC-1** and **BC-1**, the interacting phosphorus center is a $-OPF_2$ group which is more electrophilic than a $-OP(O)F_2$ group. As a consequence, the non-bonded P_2—O_1 interactions in **AC-1** and **BC-1** cause the O_2-P_2 bond lengths to increase relative to **AC** and **BC** (1.667→1.729 and 1.680→1.756 Å for **AC**→**AC-1** and **BC**→**BC-1**, respectively). In turn, the free energy of activation for elimination of N_2O is small for **AC-1**→**AC-TS2** and **BC-1**→**BC-TS2** (7.9, 1.1 kcal/mol, respectively). On the other hand, in **BC-2** and **CC-1**, the $-OP(O)F_2$ group is the electrophile which causes a much smaller increase in the P-O bond length relative to **BC** and **CC** (1.623→1.646 and 1.634→1.656 Å for **BC**→**BC-2** and **CC**→**CC-1**, respectively) and leads to a
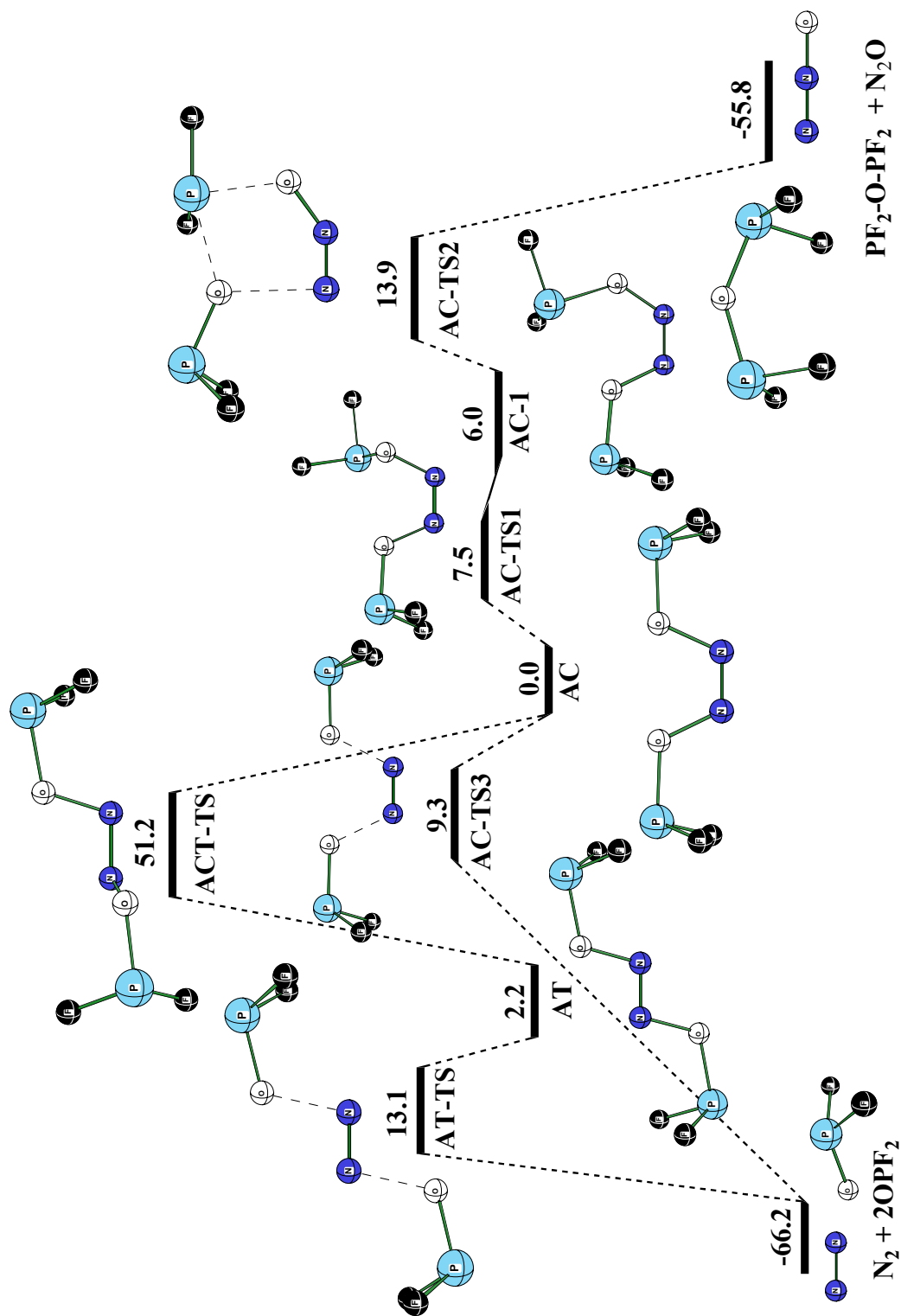
Figure 2. Reaction profiles of free energies for the reaction of **A** in THF solution at the B3LYP/LBS//B3LYP/SBS level.
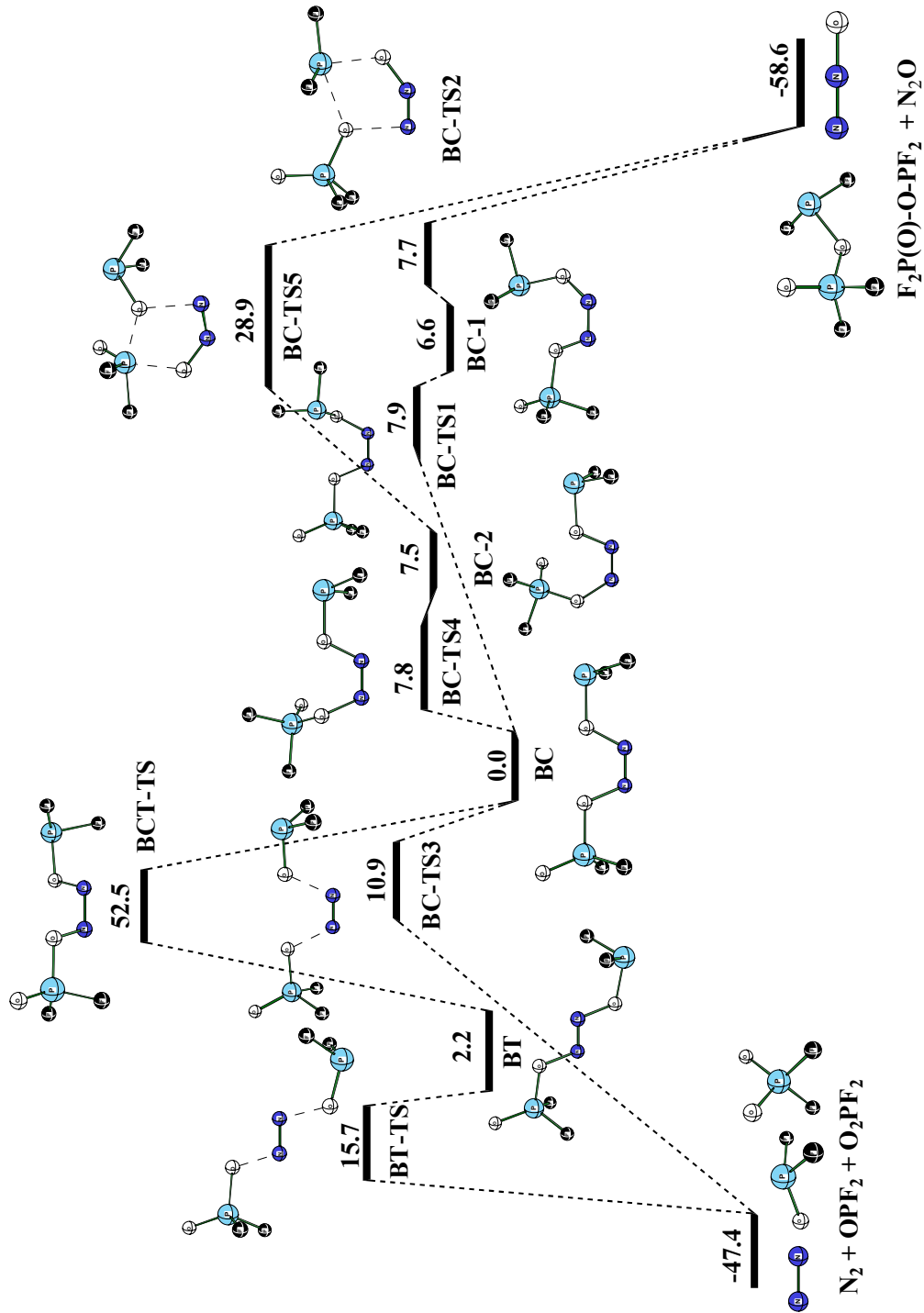
Figure 3. Reaction profiles of free energies for the reaction of **B** in THF solution at the B3LYP/LBS//B3LYP/SBS level.
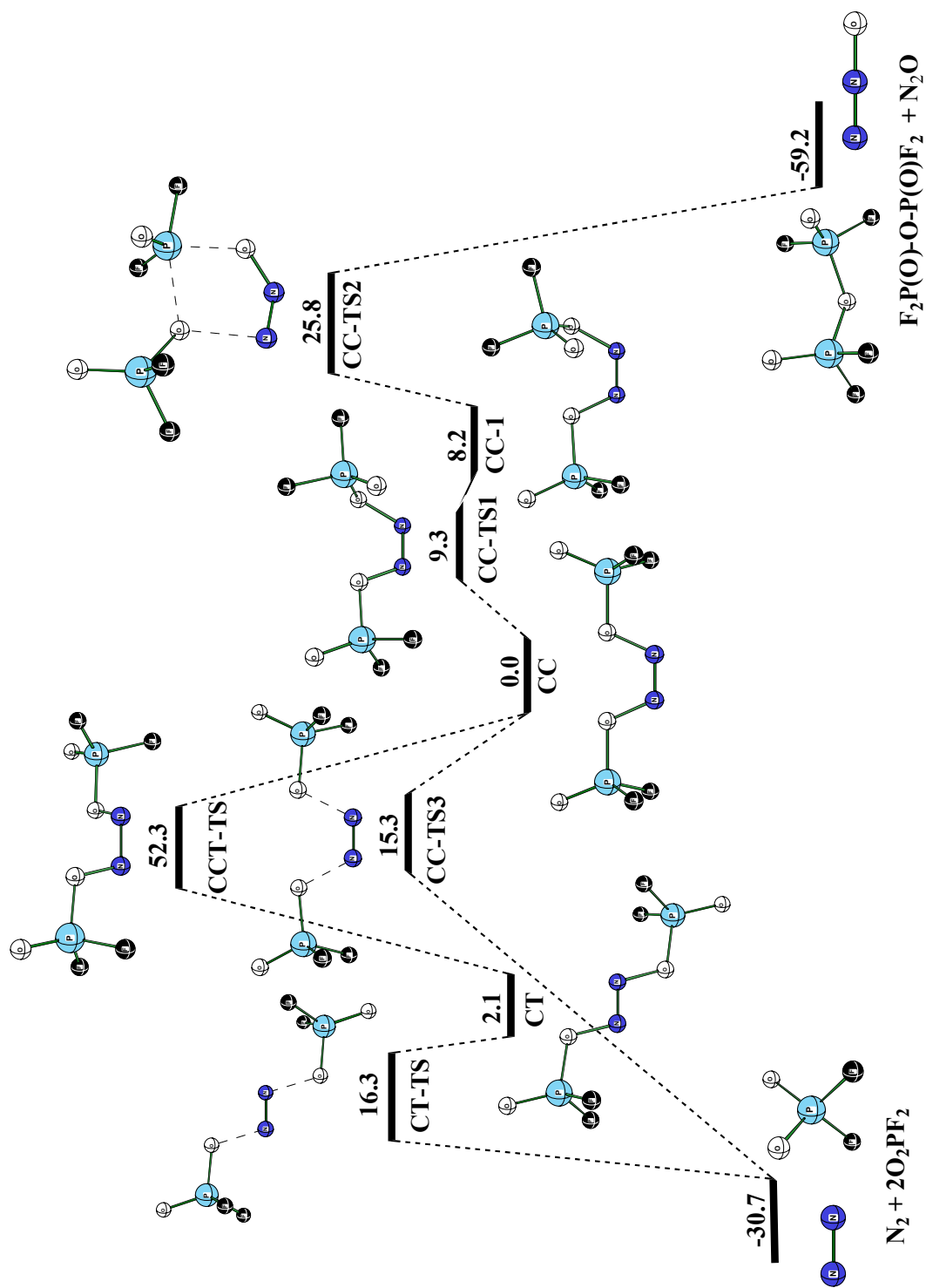
Figure 4.   Reaction profiles of free energies for the reaction of **C** in THF solution at the B3LYP/LBS//B3LYP/SBS level

Table 4.   Natural Population Analysis (NPA) Charges for Stationary Points at the
B3LYP/SBS level[a]

	P_1	P_2	N_1	N_2	O_1	O_2	$O=P_1$	$O=P_2$	Ag
AC	1.73	1.73	0.13	0.13	-0.70	-0.70			
AC-1	1.75	1.71	0.11	0.18	-0.78	-0.71			
AT	1.73	1.73	0.11	0.11	-0.68	-0.68			
AC-TS1	1.74	1.70	0.14	0.14	-0.72	-0.69			
AC-TS2	1.72	1.76	0.17	0.31	-1.12	-0.48			
AC-TS3	1.80	1.80	0.13	0.13	-0.78	-0.78			
BC	2.64	1.74	0.12	0.15	-0.70	-0.68	-1.02		
BC-1	2.65	1.73	0.11	0.20	-0.79	-0.63	-1.02		
BC-2	2.60	1.75	0.16	0.16	-0.70	-0.69	-1.02		
BT	2.53	1.66	0.10	0.13	-0.64	-0.64	-0.97		
BC-TS1	2.64	1.71	0.13	0.16	-0.72	-0.67	-1.01		
BC-TS2	2.65	1.79	0.19	0.30	-1.07	-0.50	-1.05		
BC-TS3	2.62	1.85	0.13	0.13	-0.72	-0.78	-0.99		
BC-TS4	2.60	1.74	0.14	0.16	-0.71	-0.67	-1.02		
BC-TS5	2.56	1.79	0.29	0.20	-0.49	-1.03	-1.04		
CC	2.63	2.63	0.14	0.14	-0.67	-0.67	-1.01	-0.67	
CC-1	2.62	2.60	0.15	0.17	-0.68	-0.69	-0.99	-1.11	
CT	2.63	2.63	0.11	0.11	-0.65	-0.65	-1.01	-1.01	
CS-TS1	2.62	2.60	0.15	0.16	-0.67	-0.69	-0.99	-1.02	
CS-TS2	2.66	2.56	0.23	0.31	-1.07	-0.48	-1.02	-1.00	
CS-TS3	2.61	2.61	0.14	0.14	-0.69	-0.69	-0.96	-0.96	
AgCC$^+$	2.70	2.69	0.18	0.22	-0.72	-0.70	-1.11	-1.14	0.96
AgCC-TS2$^+$	2.69	2.65	0.33	0.37	-1.19	-0.48	-1.20	-1.03	0.95
AgCC-TS3$^+$	2.67	2.67	0.20	0.20	-0.80	-0.68	-1.04	-1.09	0.95

a)   See Scheme 1 for numbering.

larger free energy of activation for N_2O elimination (21.4, 17.6 kcal/mol for **BC-2→BC-TS5**,

CC-1→CC-TS2, respectively).

The transition states for rotation around the N=N bond, which interconverts *cis-* and

trans-hyponitrites (**XCT-TS, X=A,B,C**), were located. The transition states, which have strong

biradical character ($<S^2>=1.01-1.02$), are reached after about 92° rotation around the N-N bond

which breaks the N=N π bond and causes the N-N bond to elongate by about 0.1 Å. The

activation enthalpies (298K) for the *cis*→*trans* rearrangement are very similar for **AC**, **BC**, and

CC (50.7-51.9 kcal/mol, Tables 1-3).

In all three cases the *cis* isomers are found to be global minima and *trans* isomers are

about 2 kcal/mol higher in free energy. Their potential energy surfaces are very similar along the

free energy reaction coordinates (Figures 2-4). Rotation about the N-O bond in the *cis* isomer

leads to a transition state (**XC-TS1**, **X=A,B,C**) and then an intermediate (**XC-1**,

X=A,B,C) followed by another barrier (**XC-TS2**, **X=A,B,C**) to yield N_2O plus product.

The *cis* isomer is predicted not to form the *trans* isomer due to the high free energy

barriers for breaking the N=N bond ((**XCT-TS**, **X=A,B,C**), 51.2-52.5 kcal/mol). We would like

to emphasize that these predictions are for unimolecular rearrangement of the *cis* isomer. It is

possible that the coordination of an electrophile to the *cis* isomer could lower the barrier for *cis*

$\leftrightarrow$ *trans* isomerization. For example, coordination of Ag^+ to nitrogen could lower the barrier for

cis $\leftrightarrow$ *trans* isomerization by stabilizing the transition state (Figure 5).
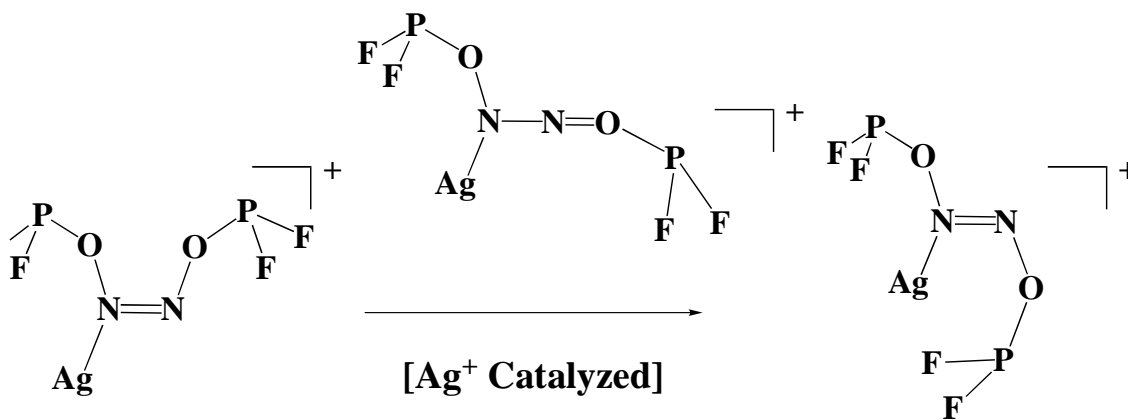
Figure 5.   Illustration of possible catalytic effect of Ag^+ on the *cis*→*trans* isomerization of
              $F_2PON=NOPF_2$.

The *trans* isomers are predicted to undergo concerted synchronous fragmentation (**XT-TS**, **X=A,B,C**) of both N-O bonds to form N_2 plus two radicals. Thus, if a *trans* isomer is initially formed, it can only fragment to produce N_2 because rearrangement to the *cis* isomer is blocked by a high barrier (unassisted reaction). On the other hand, the *cis* isomer can fragment to form either N_2 (with radicals formed) or N_2O (with no radicals formed) with competitive activation free energies (Figures 2-4). For **A** and **C**, the pathway for N_2 production is 4.6 and 10.5 kcal/mol lower than the pathway for N_2O production, while for **B**, the N_2O production pathway is lower than the N_2 production by 3.0 kcal/mol. The N_2O production pathway for **C** is much higher than for **A** or **B** because only the $-OP(O)F_2$ group (not the $-OPF_2$ group) can attack the remote oxygen atom.

Since only N_2O is observed with no radical products for **A** and **C**, the N_2O production pathway must be the preferred pathway under our experimental conditions. If the phosphorus-containing hyponitrite (**A**, **B**, or **C**) is an intermediate in the reaction, this suggests: (1) the *cis*-hyponitrite is formed in the reaction and (2) the *cis*-isomer

Figure 6.   Optimized geometries of $F_2P(O)ON=NOP(O)F_2$ with Ag(I) at the B3LYP/SBS level.

decomposes via the N_2O production pathway. While the two pathways (N_2-production and N_2O-production) have very similar free energies of activations for **A**, the calculations clearly predict N_2 production for **C**, in conflict with experiment. Thus, the reaction profile of **C** constructed by considering all the thermodynamic corrections and solvation free energies fails to explain the reaction mechanism. The question is why.

The possibility that silver cation might have a catalytic effect on the decomposition of the *cis*-isomer of **C** was considered. Optimized geometries of silver cation complexes with **C** are given in Figure 6. The most stable Ag(I)-**C** complex is not with **CC** (the global minimum) but rather with **CC-1** due to the much stronger Ag(I) interactions with the P=O oxygens (2.366 and 2.336 Å, Figure 6). Structural parameters of **AgCC**$^+$ show slightly longer bond lengths for O_1-N_1 and N_2-O_2 than those of **CC-1** but shorter P_1-O_1 and O_2-P_2 bond lengths. Interestingly, O=P_1, O=P_2 and N_1-N_2 bond lengths remain essentially the same.

The effect of Ag(I) on the PES of **C** is shown in Figure 7 and Table 5. The binding enthalpy (298K) of Ag$^+$ to both P=O oxygen atoms of the bidentate ligand is 37.8 kcal/mol (Table 5) relative to the lowest conformation (**CC**) of the ligand and 47.4 kcal/mol relative to the less stable **CC-1** conformation. In comparison, the experimental gas-phase binding enthalpy[45] (298K) of the first two waters to Ag$^+$ is 58.7 (33.3+25.4) kcal/mol. Calculated Ag$^+$ binding enthalpies to

Table 5.   Binding Energies, Enthalpies, and Free Energies (kcal/mol) of Ag(I) with
                $F_2P(O)ON=NOP(O)F_2$[a]

	ΔE_e	ΔH_{0K}	ΔH_{298K}	ΔG_{298K}	ΔG_{THF}[b]
AgCC$^+$	37.9	37.6	37.8	30.1	6.0
AgCC-TS2$^+$	55.3	54.7	54.4	48.4	23.8
AgCC-TS3$^+$	41.8	41.0	41.3	33.2	7.7

a)   Calculated at B3LYP/LBS+CPCM//B3LYP/SBS level.
b)   Including solvation free energy calculated by CPCM method in THF.
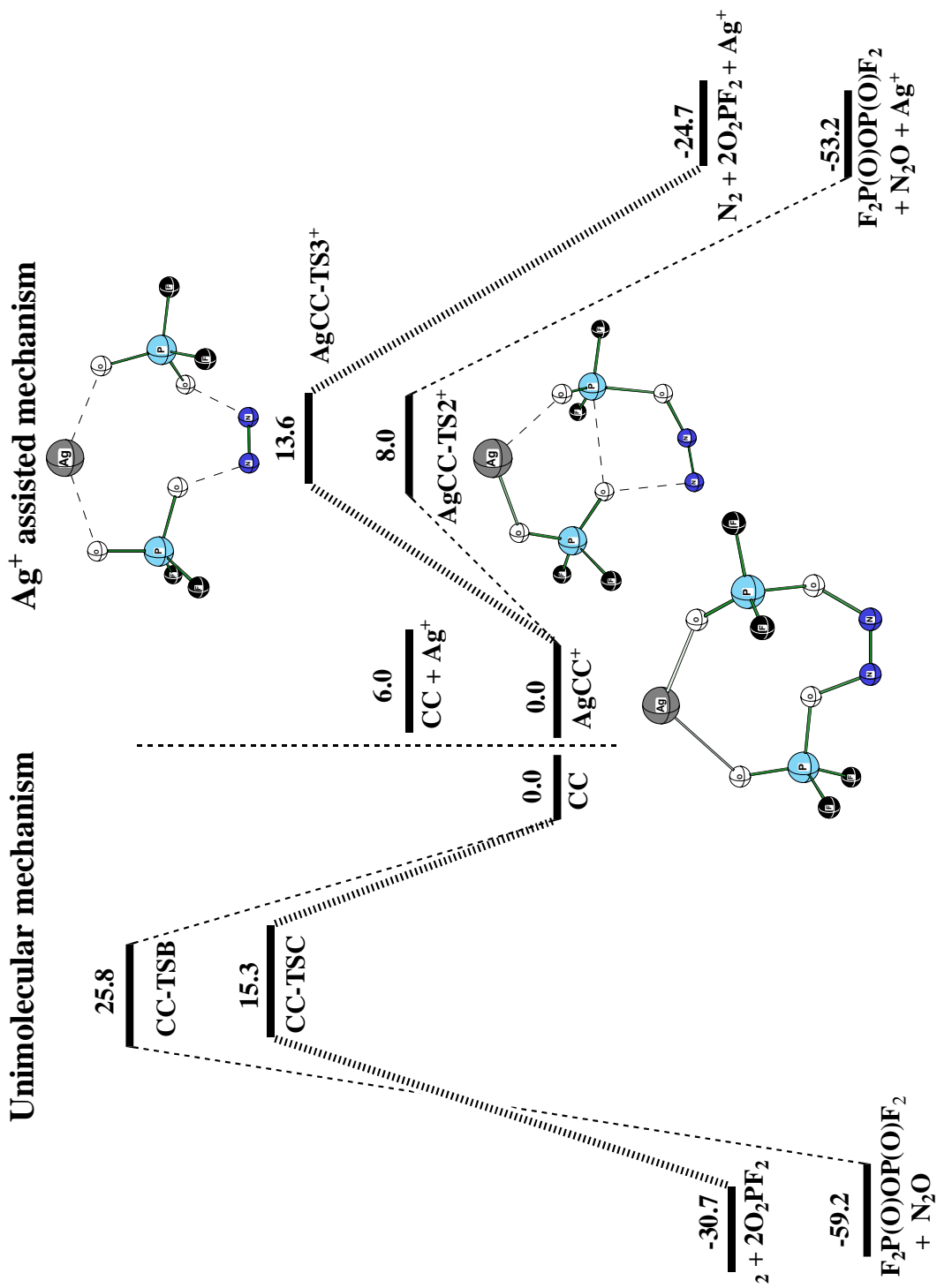
Figure 7.   Comparison of the free energy reaction profiles for C in THF with C catalyzed by Ag(I) in THF.

oxygen range from 32-38 kcal/mol (water, methanol, ethanol, diethyl ether, and acetone).[46] In

THF (which models the $F_2P(O)Br$ neat reaction environment), the Ag^+ cation is predicted to be

bound relative to $Ag^+ + CC$ by 6.0 kcal/mol in free energy (Figure 7). The bound Ag^+ has a

dramatic effect on the free energies of the two reaction pathways, N_2-producing and N_2O-

producing. The bound Ag(I) reduces the free energy barrier of the N_2O-producing pathway from

25.8 to 8.0 kcal/mol. On the other hand, the bound Ag(I) reduces the free energy barrier of the

N_2-producing pathway by only 1.7 kcal/mol (15.3→13.6 kcal/mol, Figure 7). Thus, the Ag(I)

reverses the relative free energies of the two pathway compared to the Ag(I)-free reaction and

may explain why the N_2O-producing pathway is observed experimentally.

The relative stabilities of possible radical products including PF_2, OPF_2 and O_2PF_2 were

also examined (Table 6). The PF_2 radical has been observed and computed[47] but the OPF_2 and

O_2PF_2 radicals have not yet been reported. Some experimental evidence for the existence of

O_2PF_2 has been given.[48] From the first four reaction enthalpies (298K) in Table 6, it can be seen

that the O-P bond enthalpies vary from 70.8 to 96.8 kcal/mol. This variation can be understood

from differences in radical stabilization energies (RSE), i.e. the fact that the unpaired electron

density reorganizes from the nascent radical fragment to the final radical product. From a

comparison of the spin densities and NPA charges (Table 7), it is clear that almost all of the

Table 6.   Reaction Enthalpies and Free Energies (kcal/mol) for Radical Recombinations

Bond Energy	ΔE_e	ΔH_{0K}	ΔH_{298K}	ΔG_{298K}	ΔG_{THF}[b]
$PF_2+OPF_2 \rightarrow F_2P\text{-}OPF_2$	-72.2	-70.6	-70.8	-58.4	-58.8
$OPF_2+OPF_2 \rightarrow F_2PO\text{-}P(O)F_2$	-83.0	-80.7	-81.0	-68.7	-67.7
$PF_2+O_2PF_2 \rightarrow F_2PO\text{-}P(O)F_2$	-92.3	-89.5	-89.8	-78.4	-80.5
$OPF_2+O_2PF_2 \rightarrow F_2P(O)\text{-}OP(O)F_2$	-100.0	-96.5	-96.8	-84.5	-84.8
$OPF_2+OPF_2 \rightarrow F_2P(O)\text{-}P(O)F_2$	-63.5	-60.8	-61.1	-47.9	-46.0
$OPF_2+OPF_2 \rightarrow F_2PO\text{-}OPF_2$	7.2	8.0	8.0	20.6	21.2

a)   Calculated at B3LYP/LBS//B3LYP/SBS level.

b)   Including solvation free energy calculated by CPCM method in THF.

unpaired spin density is on phosphorus in PF_2 and OPF_2 while it is distributed between the two

oxygen atoms in O_2PF_2. Thus, the initial radical formed by breaking the N-O bond in $N\text{-}OPF_2$

will undergo significant RSE to form a radical with spin on the phosphorus center, while the

initial radical formed by breaking the O-P or N-O bond in $O\text{-}PF_2$ or $N\text{-}OP(O)F_2$ will undergo little

RSE.

Radical stabilization energies (RSE) are defined in this work as the enthalpy change of

the isodesmic reaction eq 4

$$HO\text{-}H + XO \quad \rightarrow \quad XO\text{-}H + OH \qquad\qquad\qquad (4)$$
$$X = PF_2, OPF_2$$

where $RSE = \Delta H_{rxn} = \Delta H_{products} - \Delta H_{reactants}$. From this isodesmic reaction, the RSE of OPF_2 was

determined to be 24.2 kcal/mol, which is much larger than the value for O_2PF_2 (4.2 kcal/mol at

the B3LYP/LBS//B3LYP/SBS level including ZPC and C_p corrections to 298K).

Table 7.　　　Atomic Mulliken Spin Densities and NPA Charges of Radical Species Calculated
　　　　　　　at the B3LYP/SBS Level

Radical	PF_2		OPF_2		O_2PF_2	
Atom	Spin Density	NPA Charge	Spin Density	NPA Charge	Spin density	NPA Charge
P	1.02	1.17	0.77	2.03	-0.09	2.57
F	-0.01	-0.58	-0.01	-0.55	0.01	-0.54
O			0.25	-0.93	0.53	-0.74

The much larger RSE of OPF_2 compared to O_2PF_2 explains the large change in reaction

exothermicities in the N_2-producing pathways of **AC**, **BC**, and **CC** (Tables 2-4; -46.5, -29.4, and

–13.9 kcal/mol, respectively). The N_2-producing pathway of **AC** breaks two $N\text{-}OPF_2$ bonds

compared to one $N\text{-}OPF_2$ bond for the **BC** reaction and none for the **CC** reaction. The difference

in reaction exothermicities ($\Delta\Delta H_{rxn}$) is 17.1 kcal/mol for the **BC/AC** reactions and 15.1 kcal/mol

for the **CC/BC** reactions which approximately equals the difference between the RSE of OPF_2

and O_2PF_2 (20.0 kcal/mol).

Table 8. Kinetic and Thermodynamic Data (kcal/mol) for the Concerted N_2-Producing
Pathway[a]

trans-XN=NX X=	$\Delta H_a(298K)$ N_2-Producing	ΔH_{rxn} (298K)	RSE[b]
OPF_2	12.0	-48.4	2·24.2=48.4
O_2PF_2	20.2	-15.9	2·4.2=8.4
OR	25-30[c]	-6.3[d]	~0[e]

a) Calculated with respect to the *trans* hyponitrite isomer. See Tables 1-3.

b) From eq 4.

c) See ref. 49 where $R=CH_3$, CH_3CH_2, $(CH_3)_2CH$, and $(CH_3)_3C$.

d) See ref. 49 where $R=(CH_3)_3C$.

e) The RSE for the alkoxy radical (OR) is assumed to be near zero.

The variation in the activation enthalpies for the N_2-procducing pathway for

$XN=NX \rightarrow 2X+N_2$, $X=OPF_2,OP(O)F_2$ can also be understood in terms of the RSE of the radicals

produced; $\bullet OPF_2$ and $\bullet OP(O)F_2$ (Table 8). When two OPF_2 radicals are formed by the N_2-

procducing pathway, the activation barrier is smaller than when two O_2PF_2 radicals are produced

(12.0 compared to 20.2 kcal/mol, Table 8) due to the much larger RSE of the OPF_2 radicals.

Support for this interpretation comes from the experimental activation enthalpies of organic

hyponitrites RON=NOR, $R=CH_3,CH_3CH_2,(CH_3)_2CH,(CH_3)_3C$ which are known to produce N_2

upon decomposition[47] with experimental barriers of 25 to 30 kcal/mol.[49] It is reasonable to expect

the RSE's of the RO radicals ($R=CH_3,CH_3CH_2,(CH_3)_2CH,(CH_3)_3C$) to be small since little spin

reorganization is expected upon decomposition. Therefore, it is expected (and found) that their

N_2-producing barriers (25-30 kcal/mol) are larger than for either $F_2PON=NOPF_2$ or

$F_2P(O)ON=NOP(O)F_2$.

3.5 Conclusion

The reaction of neat F_2PBr and $F_2P(O)Br$ with silver hyponitrite (AgON=NOAg) did not produce the expected phosphorus-containing hyponitrites, $F_2PON=NOPF_2$ and $F_2P(O)ON=NOP(O)F_2$, but rather N_2O and μ-oxo phosphorus species. A computational study of XON=NOY, $X,Y=PF_2,P(O)F_2$ using density functional theory was carried out to explain the absence of any phosphorus-containing hyponitrites. Single-point energies (B3LYP/6-311+G(2df)//B3LYP/6-31+G(d)) using the CPCM method with the dielectric constant of THF were used to simulate the experimental environment of neat F_2PBr or $F_2P(O)Br$. Two dissociation pathways, N_2-producing and N_2O-producing, were considered. For $F_2P(O)ON=NOPF_2$, the N_2O-producing pathway was lower in free energy while the two pathways were of similar free energy in $F_2PON=NOPF_2$. For $F_2P(O)ON=NOP(O)F_2$, the N_2-producing pathway was 10.5 kcal/mol lower in free energy which is in conflict with experiment (only N_2O is produced). The disagreement is removed when the catalytic effect of Ag^+ (present from the silver hyponitrite reactant) is considered. The Ag^+ is predicted to lower the free energy barrier of the N_2O-producing pathway much more than the N_2-producing pathway.

3.6 References

(1)   Hughes, M. N. *Quart. Rev. Chem. Soc.* **1968**, *22*, 1.

(2)   Kiefer, H.; Traylor, T. G. *Tetrahedron Lett.* **1966**, *7*, 6163.

(3)   Arulsamy, N.; Bhole, D. S.; Imonigie, J. A.; Sagan, E. S. *J. Am. Chem. Soc.* **2000**, *122*, 5539.

(4)   Kuhn, L.; Lippincott, E. R. *J. Am. Chem. Soc.* **1956**, *78*, 1820.

(5)   Rauch, J. E.; Decius, J. C. *Spectrochim. Acta* **1966**, *22*, 1963.

(6)   Hughes, M. N. *J. Inorg. Nucl. Chem.* **1967**, *29*, 1376.

(7)   McGraw, G. E.; Bernitt, D. L.; Hisatsune, I. C. *Spectrochim. Acta* **1967**, *23A*, 25.

(8)   Hughes, M. N.; Stedman, G. *J. Chem. Soc.* **1963**, 2824.

(9)   Fraser, R. T. M.; Lee, R. N.; Hyden, K. *J. Chem. Soc. A* **1967**, 741.

(10)   Neuman, Jr., R. C.; Bussey, R. J. *J. Am. Chem. Soc.* **1970**, *92*, 2440.

(11)   Addison, C. C.; Gamlen, G. A. Thompson, R. *J. Chem. Soc.* **1952**, 338.

(12)   Quinga, E. M. Y.; Mendenhall, G. D. *J. Org. Chem.* **1985**, *50*, 2836.

(13)   Beck, W.; Engelmann, H.; Smedal, H. S. *Z. Anorg. Allg. Chem.* **1968**, *357*, 134.

(14)   Wiberg, V. N.; Bayer, H.; Zeigleder, G. *Z. Anorg. Allg. Chem.* **1979**, *459*, 208.

(15)   Brown, R. E.; Mendenhall, G. D.; Bartlett, R. J. *Int. J. Quantum Chem. Symp.* **1987**, *21*, 603.

(16)   Quinga, E. M. Y.; Bieker, T.; Dziobak, M. P.; Mendenhall, G. D. *J. Org. Chem.* **1989**, *54*, 2769.

(17)   Abata, J. D.; Dziobak, M. P.; Nachbor, M.; Mendenhall, G. D. *J. Phys. Chem.* **1989**, *93*, 3368.

(18)   Prinetto, F.; Ghiotti, G.; Nova, I.; Lietti, L.; Tronconi, E.; Forzatti, P. *J. Phys. Chem. B* **2001**, *105*, 12732.

(19)   Westerberg B.; Fridell, E. *J. Mol. Catal. A: Chem.* **2001**, *165*, 249.

(20)   Al-Ajlouni, A. M.; Gould, E. S *J. Chem. Soc. Dalton Trans.* **2000**, 1239.

(21)   Feldmann, C.; Jansen, M. *Angew. Chem. Int. Ed. Engl.* **1996**, *35*, 1728.

(22)   Arulsamy, N.; Bohle, D. S.; Imonigie, J. A.; Levine, S. *Angew. Chem. Int. Ed.* **2002**, *41*, 2371.

(23)   Poskrebyshev, G. A.; Shafirovich, V.; Lymar, S. V. *J. Am. Chem. Soc.* **2004**, *126*, 891.

(24)   Arulsamy, N.; Bohle, D. S.; Imonigie, J. A.; Sagan, E. S. *Inorg. Chem.* **1999**, *38*, 2716.

(25)   Joo, Hyun; Biswas, M. A. S.; Hill, W. E.; McKee, M. L. *J. Phys. Chem. A* **2005**, *109*, 1420.

(26)   Biswas, M. A. S. *Preparation and Reactions of Fluorophosphonium ions; Reaction of Silver Hyponitrite with a Series of Main Group Compounds*, Auburn University, 1988

(27)   Brauer, G. *Handbook of Preparative Inorganic Chemistry*, Academic Press: New York, 1963; Vol 1, p 494.

(28)   (a) Parshall, G. W. *Inorganic Synthesis*; McGraw-Hill: New York, 1974; Vol. 15, p 186. (b) Parry, R. W. *Inorganic Synthesis*; McGraw-Hill: New York, 1970; Vol. 12, p 287.

(29)   Reinhardt, H.; Bianchi, D.; Mölle, D. *Chem. Ber.* **1957**, *90*, 1656.

(30)   Magnelli, D. D.; Tesi, G.; Lowe, Jr., J. U.; McQuisition, W. E. *Inorg. Chem.* **1966**, *5*, 457.

(31)   (a) Cavell, R, G. *Can. J. Chem.* **1967**, *45*, 1309. (b) Hägele, G.; Kuchen, W.; Steinberger, H. *Z. Naturforsch.* **1974**, *29B*, 349.

(32)   Crutchfield, M. M.; Dungan, C. H.; Lechter, J. H.; Mark, V.; Van Wazer, J. R. In *Topics in Phosphorus Chemistry,* Grayson, M.; Griffith, E. J., Eds. Wiley: New York, 1967*,* Vol. 5*,* p 281.

(33)   Robinson, S. A. *Can. J. Chem.* **1962**, *40*, 1725.

(34)   Rudolph, R. W.; Taylor, R. C.; Parry, R. W. *J. Am. Chem. Soc.* **1966**, *88*, 3729.

(35)   *Gaussian03, (Revision B.4)*, Frisch, M. J.; Trucks, G. W.; Schlegel, H. B.; Scuseria, G.

         E.; Robb, M. A.; Cheeseman, J. R.; Montgomery, J. A. Jr.; Vreven, T.; Kudin, K. N.;

         Burant, J. C.; Millam, J. M.; Iyengar, S. S.; Tomasi, J.; Barone, V.; Mennucci, B.; Cossi,

         M.; Scalmani, G.; Rega, N.; Petersson, G. A.; Nakatsuji, H.; Hada, M.; Ehara, M.;

         Toyota, K.; Fukuda, R.; Hasegawa, J.; Ishida, M.; Nakajima, T.; Honda, Y.; Kitao, O.;

         Nakai, H.; Klene, M.; Li, X.; Knox, J. E.; Hratchian, H. P.; Cross, J. B.; Adamo, C.;

         Jaramillo, J.; Gomperts, R.; Stratmann, R. E.; Yazyev, O.; Austin, A. J.; Cammi, R.;

         Pomelli, C.; Ochterski, J. W.; Ayala, P. Y.; Morokuma, K.; Voth, G. A.; Salvador, P.;

         Dannenberg, J. J.; Zakrzewski, V. G.; Dapprich, S.; Daniels, A. D.; Strain, M. C.; Farkas,

         O.; Malick, D. K.; Rabuck, A. D.; Raghavachari, K.; Foresman, J. B.; Ortiz, J. V.; Cui,

         Q.; Baboul, A. G.; Clifford, S.; Cioslowski, J.; Stefanov, B. B.; Liu, G.; Liashenko, A.;

         Piskorz, P.; Komaromi, I.; Martin, R. L.; Fox, D. J.; Keith, T.; Al-Laham, M. A.; Peng,

         C. Y.; Nanayakkara, A.; Challacombe, M.; Gill, P. M. W.; Johnson, B.; Chen, W.; Wong,

         M. W.; Gonzalez, C.; and Pople, J. A. Gaussian, Inc., Pittsburgh PA, 2003.

(36)   Koch, W.; Holthausen, M. C. A Chemist's Guide to Density Functional Theory, Wiley:

         New York, 2001.

(37)   (a) Hay, P. J.; Wadt, W. R. *J. Chem. Phys.* **1985**, *82*, 270. (b) Wadt, W. R.; Hay, P. J. *J.

         Chem. Phys.* **1985**, *82*, 284. (c) Hay, P. J.; Wadt, W. R. *J. Chem. Phys.* **1985**, *82*, 299.

(38)   *MOLDEN,* Schaftenaar, G.; Noordik, J. H. *J. Comput.-Aided Mol. Design*, **2000**, *14*, 123.

(39)   Dolg, M.; Stoll, H.; Preuss, H.; Pitzer, R. M. *J. Phys. Chem.* **1993**, *97*, 5852.

(40)   Reed, A.; Curtiss, L. A.; Weinhold, F. *Chem. Rev.* **1988**, *88*, 899.

(41)   (a) Barone V.; Cossi, M. *J. Phys. Chem. A* **1998**, *102*, 1995. (b) Cossi, M.; Rega, N.;

         Scalmani, G.; Barone, V. *J. Comput. Chem.* **2003**, *24*, 669.

(42)   The dielectric constant for THF is 7.5. The dielectric constant for liquid $O=PCl_3$ is 14.0.

         See: http://www.asiinstr.com/dc1.html

(43)   Loechler, E. L.; Schneider, A. M.; Schwartz, D. B.; Hollocher, T. C. *J. Am. Chem. Soc.* **1987**, *109*, 3076.

(44)   Hussain, M. A.; Stedman, G.; Hughes, M. N. *J. Chem. Soc. B* **1968**, 597.

(45)   Holland, P. M.; Castleman, Jr., A. W. *J. Chem. Phys.* **1982**, *76*, 4195.

(46)   (a) Ma, N. L. *Chem. Phys. Lett.* **1998**, *297*, 230. (b) El Aribi, H.; Shoeib, T.; Ling, Y.; Rodriquez, C. F.; Hopkinson, A. C.; Siu, K. W. M. *J. Phys. Chem. A* **2002**, *106*, 2908.

(47)   (a) Howe, J. D.; Ashfold, M. N. R.; Hudgens, J. W.; Johnson, III, R. D. *J. Chem. Phys.* **1994**, *101*, 3549. (b) Burdet, J. K.; Hodges, L; Dunning, V.; Current, J. H. *J. Phys. Chem.* **1970**, *74*, 4053. (c) Nelson, W.; Jackel, G.; Gordy, W. *J. Chem. Phys.* **1970**, *52*, 4572. (d) Wei, M. S.; Current, J. H.; Gendell, J. *J. Chem. Phys.* **1970**, *52*, 1592. (e) Hinchliffe, A.; Bounds, D. G. *J. Mol. Struct.* **1979**, *54*, 231.

(48)   Eisenberg, M.; Desmarteau, D. D. *Inorg. Chem.* **1972**, *11*, 1901.

(49)   Chen, H.-T. E.; Mendenhall, G. D. *J. Am. Chem. Soc.* **1984**, *106*, 6375.

CHAPTER 4

COMPUTATIONAL STUDY OF THE "STABLE" BIS(AMINO)SILYLENE REACTION WITH HALOMETHANES. A RADICAL OR CONCERTED MECHANISM?

4.1 Introduction

The first report of the isolation of a stable silylene, *N,N'*-di-*t*-butyl-1,3-diaza-2-silacyclopent-4-en-2-ylidene, **1**, in 1994[1] resulted in a flurry of publications investigating its chemical and physical properties. At the forefront of the research was the origin of its stability. Both theoretical[2-10] and experimental[8-12] studies have concurred that π-electron donation from the α-substituent to the formally empty silicon p orbital and possible aromaticity of the 6-π electron ring are the main factors causing the divalent silicon species to be stabilized.

1 : R = *t*-Bu
A : R = H
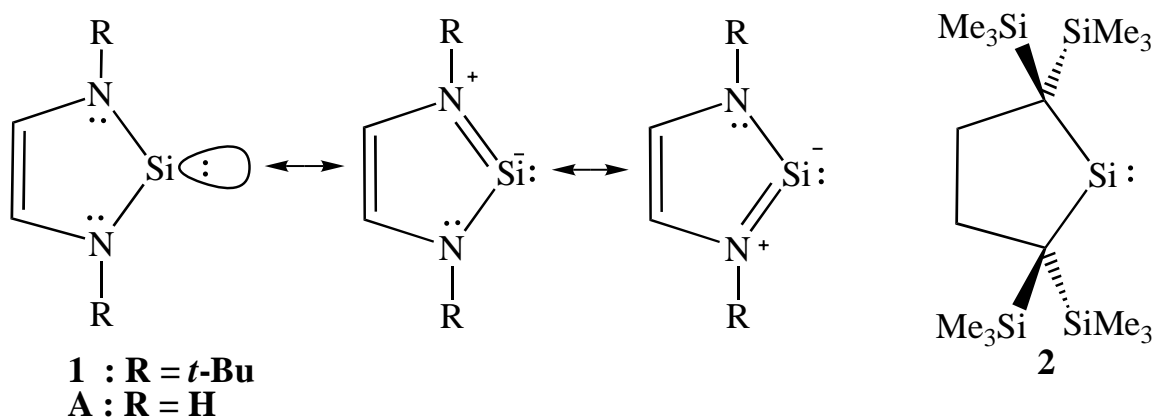
Scheme 1

In addition, there has been an active interest in the reactivity of **1** and related silylenes.[12-18] A divalent silylene, like the isolelectronic divalent carbene,[19] can be a Lewis acid or a Lewis base by virtue of its low-lying vacant p orbital (Lewis acid) and its nonbonding electron pair (Lewis base). It is now well established that acyclic silylenes and cyclic alkyl silylenes behave as Lewis acids.[7a,12] On the other hand, cyclic bis(amino)silylenes can act as Lewis bases by donating the nonbonding electron pair on the silicon atom as in silylene-metal complexes,[14-18] or in Arduengo carbenes (1,3-diimidazol-2-ylidene).[19]

As shown in Scheme 1, π conjugation increases the electron population of the empty p orbital on the Si atom which leads to lower acidity and higher basicity. This can account for the different reactivities of the two types of silylenes, dialkylsilylenes (Lewis acids) and bis(amino)silylenes (Lewis bases).

A number of reactions utilize the electron donicity of **1**, and are well understood.[13-17] However, few examples can be found for the reaction of **1** with Lewis bases. Recently, reactions of silylenes with halocarbons were reported.[18,20-22] The reactions of dialkylsilylene, 2,2,5,5-tetrakis(trimethylsilyl)silacyclopentane-1,1-diyl, **2**, with halomethanes were studied by Ishida *et al.*[20] The reactions of **2** with CCl_4 and $CHCl_3$ gave dichlorosilane by a radical mechanism. Methyl iodide also reacts with **2** to give a single insertion product. However, the reaction with CH_2Cl_2 gave double insertion products in which two Si atoms are bonded to a carbon atom. The authors[20] suggested that the activation of the C-Cl bond by silylene complexation would facilitate the nucleophilic attack of another silylene and proposed a Lewis acid-Lewis base reaction mechanism via an acid-base complex. Similarly, the reactions of **1** with halomethanes (Scheme 2) were reported by West and co-workers.[18,21,22] The reaction between **1** and ICH_3 was reported to give a 1:1 adduct as exclusive product, while chlorocarbons, except for *t*-BuCl, reacted with **1** to give a 2:1 adduct. Interestingly, reaction with bromobenzene gave mixed products of the 1:1 and 2:1 adducts (Scheme 2). Further investigation showed that the proportion of product yields,

1:1 and/or 2:1 adducts, changed depending upon the ratio of the reactants. Also, increasing the

bromobenzene ratio led to a higher proportion of 1:1 adduct with exclusively 1:1 adduct after four

equivalents of bromobenzene. From these observations, a radical mechanism was suggested
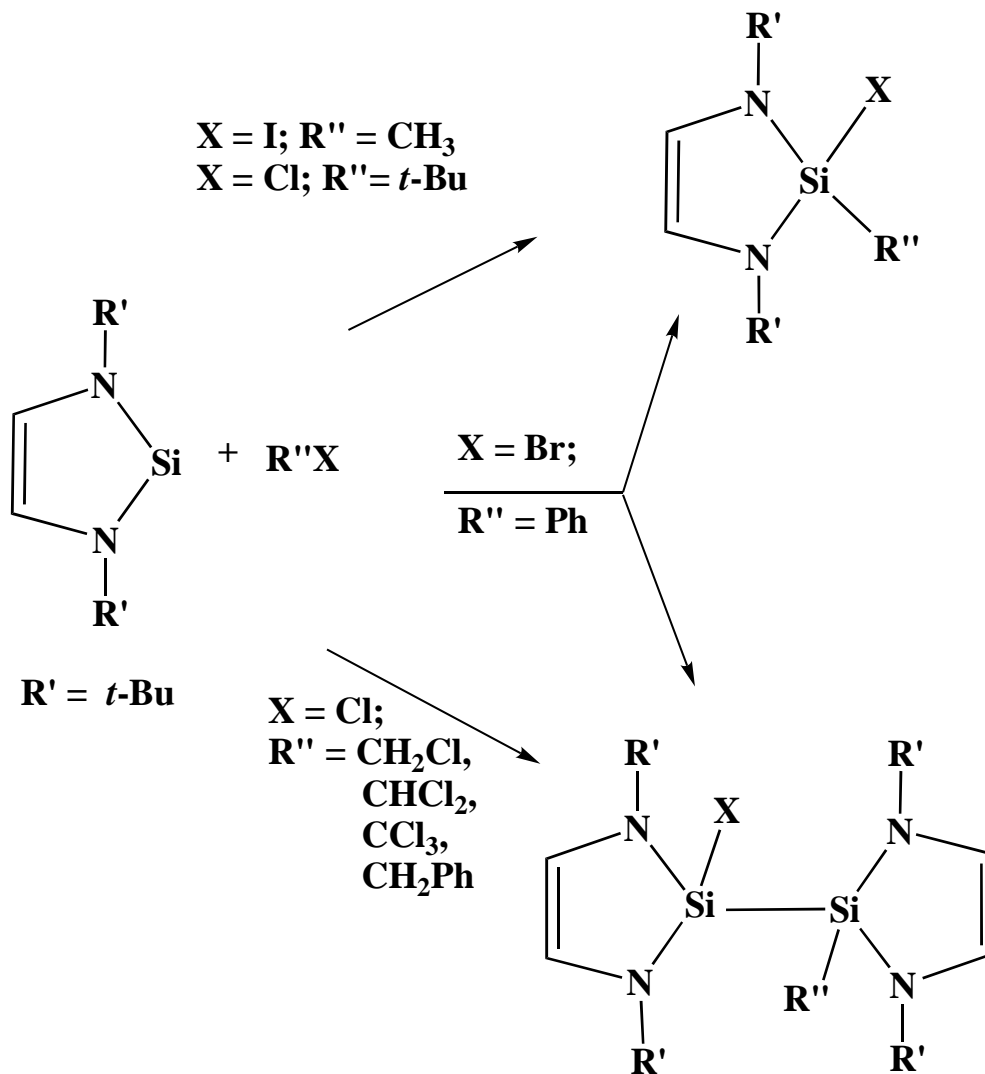
Scheme 2

for the formation of the 1:1 adducts with ICH_3, but a 1,2-shift mechanism with bromobenzene

and t-BuCl via a 1:1 intermediate complex. For chlorocarbons, a halophilic mechanism via a 1,3-

shift from a 2:1 intermediate complex was proposed. Both silylenes, **1** and **2**, show similar trends

of reactivities towards halomethanes, even though they have completely different chemical properties.

Recently theoretical studies on the mechanism of halophilic reactions of silylene **A** (Scheme 1) with ClCH$_3$, CHCl$_3$ and CHBr$_3$ were reported at the B3LYP/6-31G* level.[23] The author suggested that the reactions follow the general pathway: insertion of silylene into a halogen-carbon bond followed by dimerization with another silylene to form the final 2:1 reaction product. However, the reported results cannot completely account for the experimental observations. If the disilane product (2:1 adduct) were formed via initial insertion into Si-X bond of the 1:1 product, the 1:1 product should be observed in the reaction of silylene **1** with a 100-fold excess of CHCl$_3$ as is the case in the reaction with bromobenzene.[22] Furthermore, the possibility of radical involvement was excluded in the study, since only restricted DFT calculations were performed.[23] Therefore, we felt that it is necessary to reinvestigate the reaction of bis(amino)silylene (**A**) with halomethanes to consider the radical mechanism. This work has been published in Journal of Physical Chemistry A in 2005.[24]

4.2 Computational Details

Possible reactions of silylene **A** with XCH$_3$ (X=Cl, Br, I) were examined by using density functional theory[25] implemented in the Gaussian03 program.[26] The hybrid B3LYP combination of exchange and correlation functionals[25b] was utilized throughout this study. Geometry optimizations of all stationary points were performed with a 6-31+G(d) basis set for H, C, N, Si, Cl and Br and with a standard LanL2DZ[27] effective core potential (ECP) and basis set for I (Figure 1). At each stationary point, vibrational frequencies were calculated to confirm whether it was a minimum (no imaginary frequencies) or transition state (one imaginary frequency). At every transition state, the transition vector was animated with the Molden program,[28] and if necessary, the intrinsic reaction coordinate (IRC)[29] was computed to connect the corresponding

minima. To obtain a better energetic description of the reaction profile, single-point calculations were performed with a larger 6-311++G(2df,p) basis set for all atoms except for I, for which the SDD[30] ECP and basis set were used. Thermodynamic corrections to 298K, zero-point vibrational energy corrections (ZPC), heat capacity corrections (C_p), and entropy corrections (ΔS) obtained at the B3LYP/6-31+G(d)+LanL2DZ level were applied to single-point energies at the B3LYP/6-311++G(2df,p)+SDD level. The reaction profiles were constructed based on relative free energies at 298K (Figure 2-4). For convenience, "SBS" will be used to denote the 6-31+G(d)+LanL2DZ basis set and "LBS" to denote the 6-311++G(2df,p)+SDD basis set. The transition states on the singlet PES were tested to determine whether a spin broken-symmetry solution was lower in energy. If so, the transition state was reoptimized with the spin broken-symmetry method. These structures are tabulated in Table 1 (**Cl-TS3**, **Br-TS2**, **Br-TS3**, **I-TS2**) with the $<S^2>$ expectation value. A notation scheme is used in the text, Figures, and Tables for the various structures where "**X**" is the halogen (**Cl**, **Br**, or **I**), "**A**" is the cyclic bis(amino)silylene, "**D**" stands for two cyclic silylene units bonded with a Si-Si bond, and "**P**" stands for a product.

Natural population analysis (NPA) was carried out on the important radical intermediates at the UB3LYP/SBS level by utilizing the NBO program[31] implemented in Gaussian to explain the different reactivity of silylene toward halomethanes. In addition, Si-CH_3 and Si-X bond enthalpies were determined in **X-P1** (Figure 1; X=Cl, Br, I) and compared with X-CH_3 bond enthalpies.

4.3 Results and Discussion

Bond lengths and bond angles of **A** optimized at the B3LYP/6-31+G(d) level are in good agreement with those at the MP2/6-311G(d) level[2b] and also agree with those determined by gas-phase electron-diffraction[1] and solid state X-ray diffraction[32] of the *t*-Bu derivative, **1** (Figure 1a).

Table 1. Calculated Electronic Energies (hartrees), Zero-Point Energies, Heat Capacity Corrections to 298K (kcal/mol), Entropy (cal/mol·K) and Spin-Squared Values ($<S^2>$) are Calculated at the B3LYP/SBS Level

	ZPC	$C_{p\ corr}$	S	$<S^2>$	B3LYP/SBS	B3LYP/LBS
A	41.9	3.4	67.6		-477.64745	-477.73632
AT[a]	40.6	3.9	74.6	2.01	-477.55314	-477.63895
CH$_3$	18.8	2.5	46.5	0.75	-39.84264	-39.85653
Me-A	64.1	5.0	82.9	0.76	-517.53588	-517.63997
Me-D	106.3	9.0	118.1	0.76	-995.19985	-995.39464
Me-TS	61.2	6.0	95.6	0.75	-517.49031	-517.59302
MeD-TS	106.3	8.7	122.3	0.76	-995.18501	-995.37706
ClCH$_3$	23.9	2.5	56.0		-500.11152	-500.15697
Cl-A	42.2	4.6	82.1	0.76	-937.86658	-937.98978
Cl-D	84.6	8.5	115.6	0.76	-1415.53326	-1415.74792
Cl-P1	65.9	6.0	90.0		-977.83386	-977.97601
Cl-P2	107.8	10.0	125.4		-1455.48668	-1455.71920
Cl-TS1	65.0	6.0	93.8		-977.67677	-977.81091
Cl-TS2	64.3	6.3	97.2		-977.67376	-977.81063
Cl-TS3	62.7	6.7	100.6	0.69	-977.70646	-977.84346
ClD-TS	84.6	8.2	115.8	0.76	-1415.51770	-1415.72991
ClA-TS	65.2	7.5	109.9	0.76	-1437.95702	-1438.13061
ClMeA-TS	87.3	7.9	112.3	0.76	-1017.63345	-1017.78579
ClMeD-TS	129.2	11.9	147.0	0.76	-1495.29462	-1495.53768
ClDCl-TS	107.5	11.4	143.3	0.76	-1915.62568	-1915.88940
BrCH$_3$	23.5	2.5	58.8		-2611.63240	-2614.07317
Br-A	42.1	4.7	85.0	0.76	-3049.39289	-3051.90445
Br-D	84.5	8.7	118.9	0.76	-3527.06051	-3529.66078
Br-P1	65.7	6.1	92.5		-3089.35807	-3091.88715
Br-P2	107.6	10.2	127.9		-3567.01446	-3569.63195
Br-TS1	64.8	6.1	95.7		-3089.20762	-3091.73264
Br-TS2	62.7	6.7	103.6	0.71	-3089.21634	-3091.74032
Br-TS3	61.2	7.5	111.8	1.00	-3089.23614	-3091.76072
BrD-TS	84.5	8.2	116.8	0.76	-3527.04677	-3529.64438
BrA-TS	64.7	7.6	114.5	0.76	-5661.02212	-5665.96792
BrMeA-TS	87.3	7.8	113.2	0.76	-3129.17238	-3131.71068
BrMeD-TS	129.1	12.0	148.4	0.76	-3606.83581	-3609.46322
ICH$_3$	23.2	2.6	60.8		-51.29691	-51.34492
I-A	42.1	4.8	87.6	0.76	-489.04402	-489.17480
I-D	84.5	8.7	120.9	0.76	-966.70179	-966.92838
I-P1	65.6	6.2	95.0		-529.00236	-529.15297
I-P2	107.7	10.2	129.5		-1006.65409	-1006.89921
I-TS1	64.6	6.2	98.4		-528.86767	-528.99464
I-TS2	62.4	6.9	107.3	0.82	-528.87552	-529.00960
ID-TS	84.3	8.4	121.3	0.76	-966.69006	-966.91470
IA-TS	63.9	8.0	120.9	0.78	-540.32671	-540.51151
IMeA-TS	86.9	8.0	116.1	0.77	-568.82684	-568.98773

	ZPC	C$_{p\ corr}$	S	$\langle S^2 \rangle$	B3LYP/SBS	B3LYP/LBS
IMeD-TS	128.9	12.0	148.8	0.77	-1046.48418	-1046.74062
CH$_2$Cl$_2$	18.6	2.8	64.6		-959.70053	-959.77776
CHCl$_3$	12.5	3.4	70.7		-1419.28431	-1419.39407
CCl$_4$	5.8	4.1	74.2		-1878.85980	-1879.00285
Cl2-TS	58.3	7.0	108.1	0.60	-1437.30515	-1437.47319
Cl3-TS	53.1	7.5	114.0	0.49	-1896.89944	-1897.09927
Cl4-TS	47.1	8.2	118.6	0.35	-2356.48627	-2356.71888
SiM	76.9	5.4	83.4		-556.26415	-556.26415
SiM-TS	97.6	8.9	119.5	0.67	-1056.32575	-1056.48006
SiM-Cl2TS	93.2	9.2	125.4	0.59	-1515.92477	-1516.11026

a)   Triplet silylene **A**.

The slightly longer Si-N bond lengths in **A** than in **1** can be rationalized by greater electron

donation from the *t*-Bu group in **1**. The possible radical intermediates, **X-A** (X=Cl, Br, I) and

Me-A, show interesting characteristics. Since the 4n+2 π-electron system is interrupted by the

addition of a halogen radical in **X-A** or a methyl radical in **Me-A**, the Si-N bonds lengthen

(0.047-0.053 Å in **X-A** and 0.028 Å in **Me-A**). In addition, the C-C bonds become longer and the

C-N bonds shorter indicating a greater degree of localization in the (-NHCH)$_2$ unit. When the

methyl radical is added (**Me-A**), the C-C and C-N bond lengths show very little change, while the

Si-CH$_3$ bond is long (1.923 Å) compared to other Si-C bonds. Electron donation from the methyl

group strengthens the Si-N bonds and increases delocalization over the (–NHCH)$_2$ unit. On the

other hand, the halogen atom withdraws electron density from the silicon atom and weakens (and

lengthens) the Si-N bonds. The atomic NPA charges and spin densities of **X-A** and **Me-A**

support this interpretation (Table 2). When a Cl or Br atom is attached to **A** (**Cl-A** or **Br-A**), the

spin density is delocalized over the ring with very little spin density on the halogen atom, while,

in contrast, the iodine atom has significant spin density in **I-A**. In **Me-A**, most of the spin density

resides on silicon (0.62 e$^-$) due to 2c-2e Si-C bond formation and the prerequisite electron

promotion.
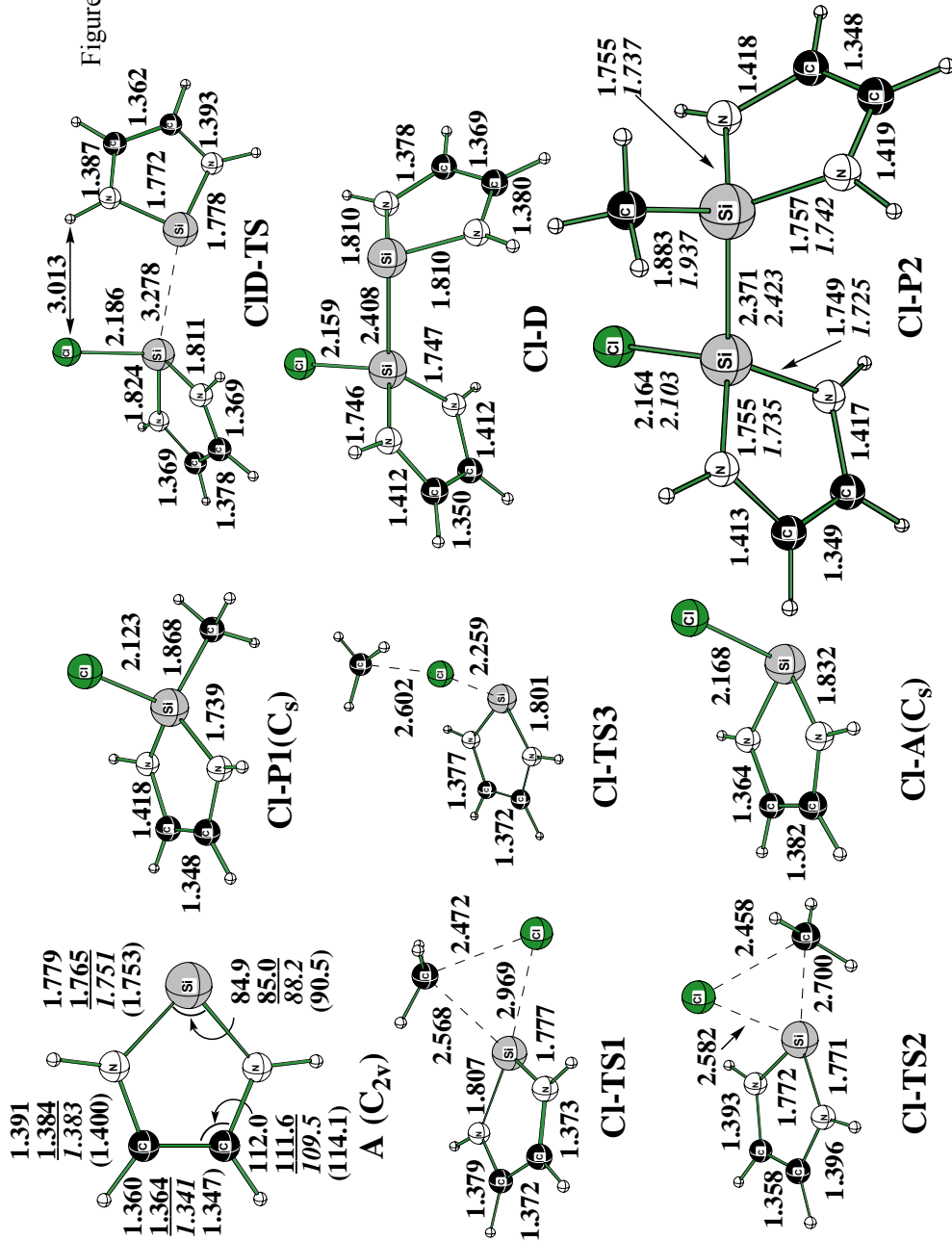
Figure 1. Geometries optimized at B3LYP/6-31+G(d) level where bond lengths are in Å, angles are in degrees, and Schönflies symbols are given in parentheses. (a) Geometrical parameters for stationary points in the reaction of **A** with ClCH₃. The geometry of **A** is compared with MP2/6-311G(d)[2b] underlined; with **1** by gas phase electron diffraction[1] in parentheses; and with **1** by X-ray diffraction[32] *italicized.* The geometry of **Cl-P2** is compared with X-ray diffraction[22] where the *t*-Bu groups have replaced the hydrogens on nitrogen.
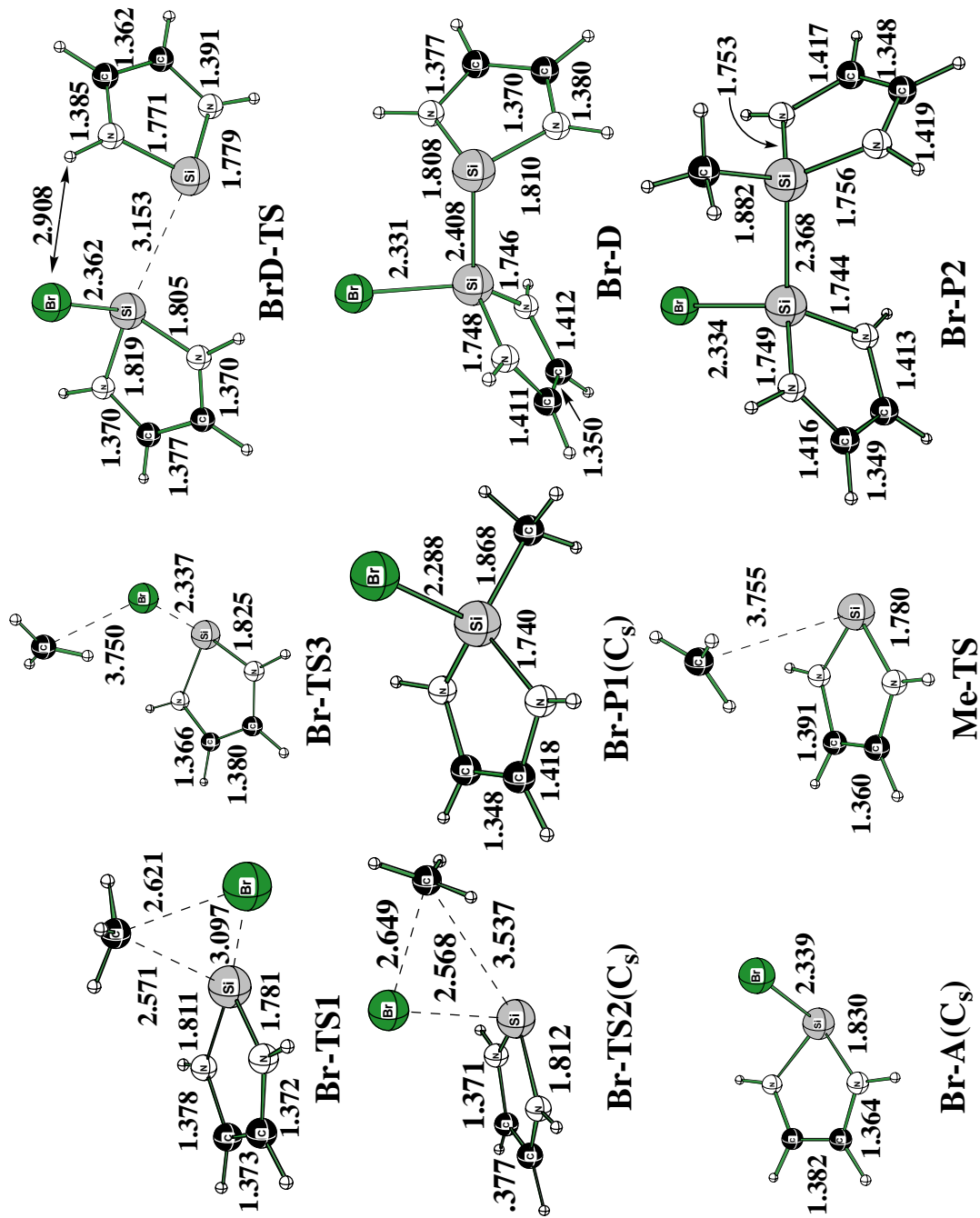
Figure 1. (b)   Geometrical parameters of stationary points in the reaction of **A** with $BrCH_3$.
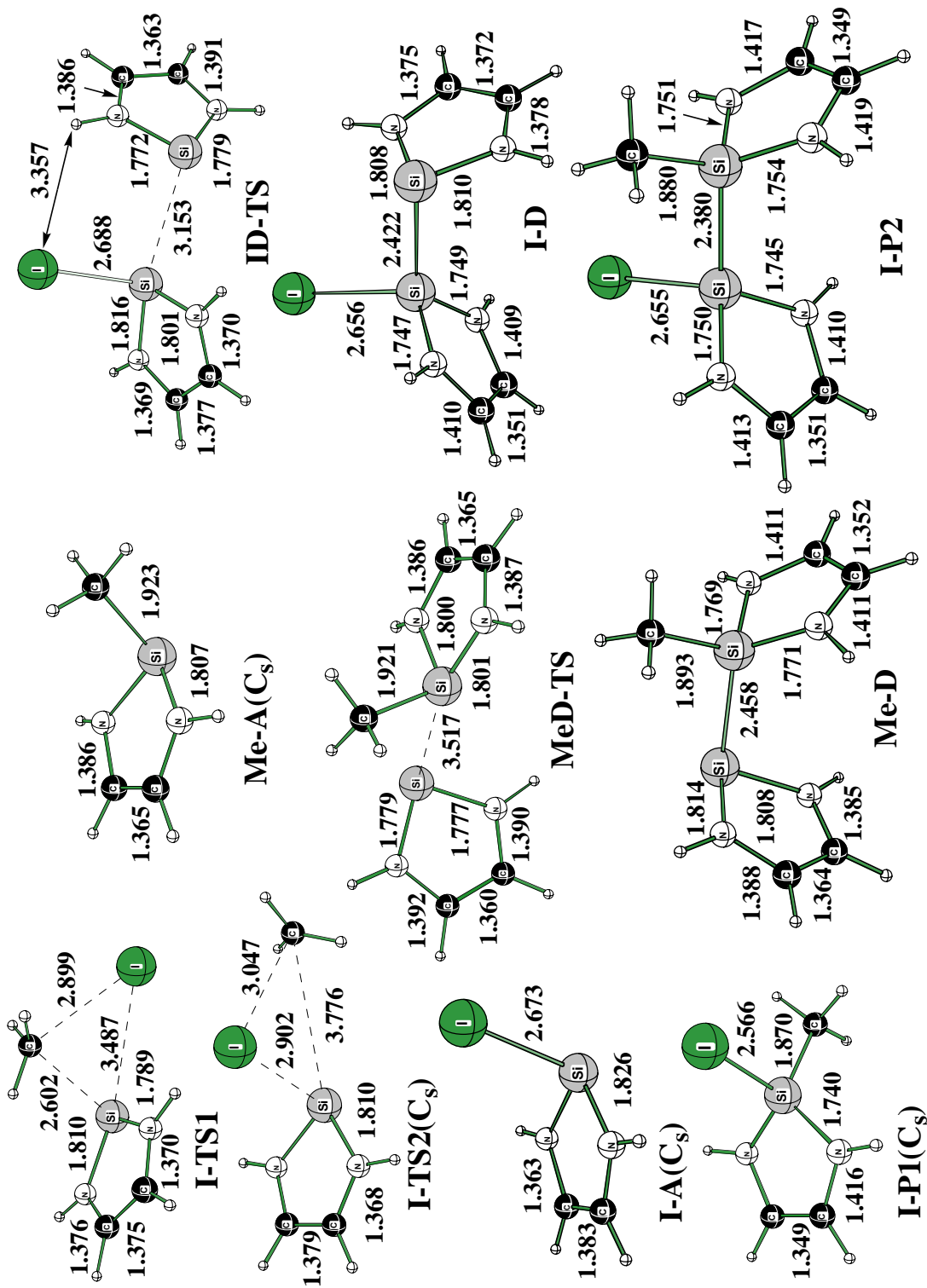
Figure 1. (c) Geometrical parameters of stationary points in the reaction of A with ICH₃.

98

CIMeA-TS (14.6)   **BrMeA-TS (10.0)**   **IMeA-TS (6.4)**

CIMeD-TS (16.6)   **BrMeD-TS (11.4)**   **IMeD-TS (8.4)**
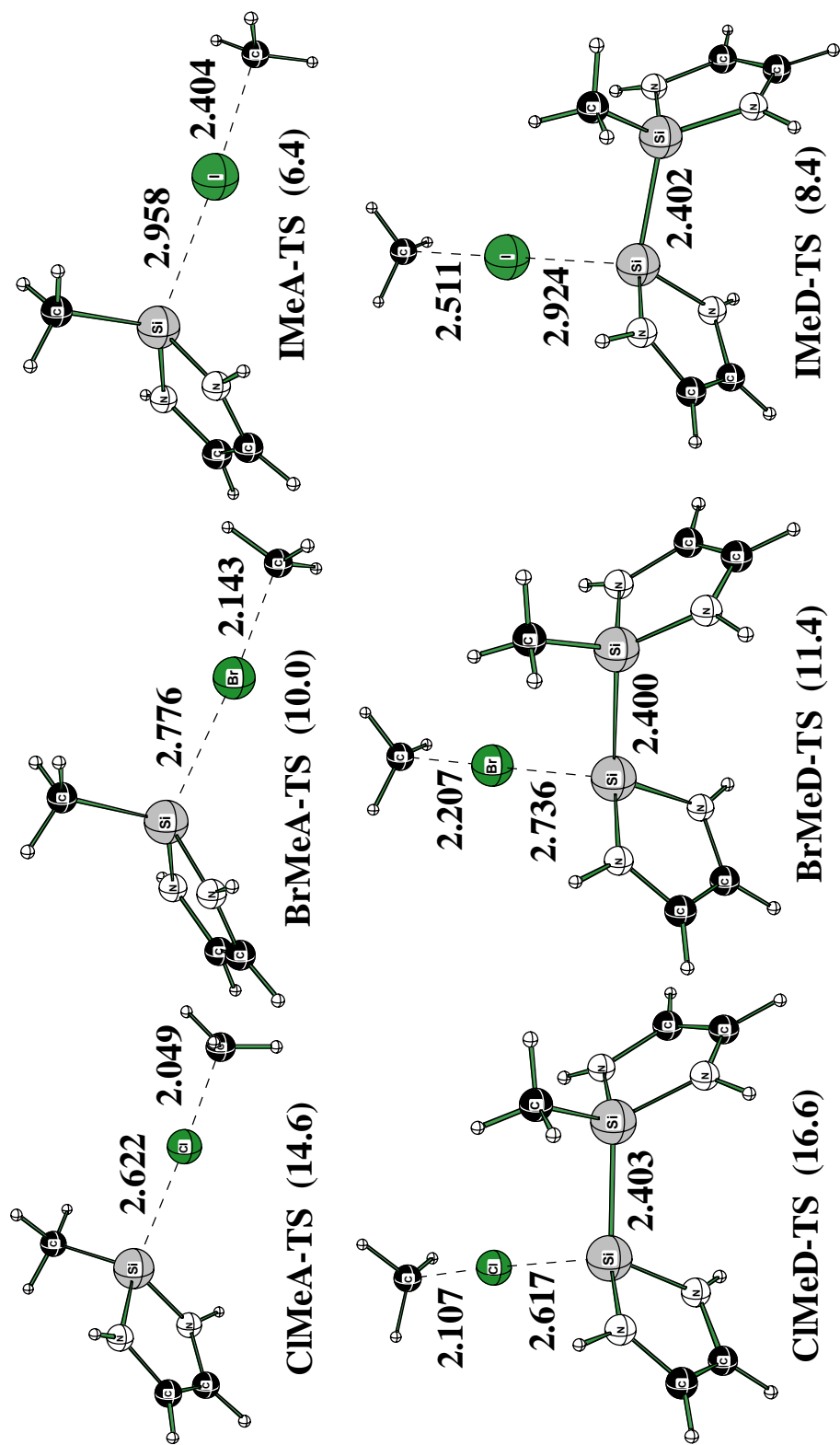
Figure 1. (d) Geometrical parameters of transition states in the reaction of **Me-A** with XCH$_3$ (**XMeA-TS**) and in the reaction of **Me-D** with XCH$_3$ (**XMeD-TS**). Free energies in kcal/mol are given in parentheses with respect to reactants.
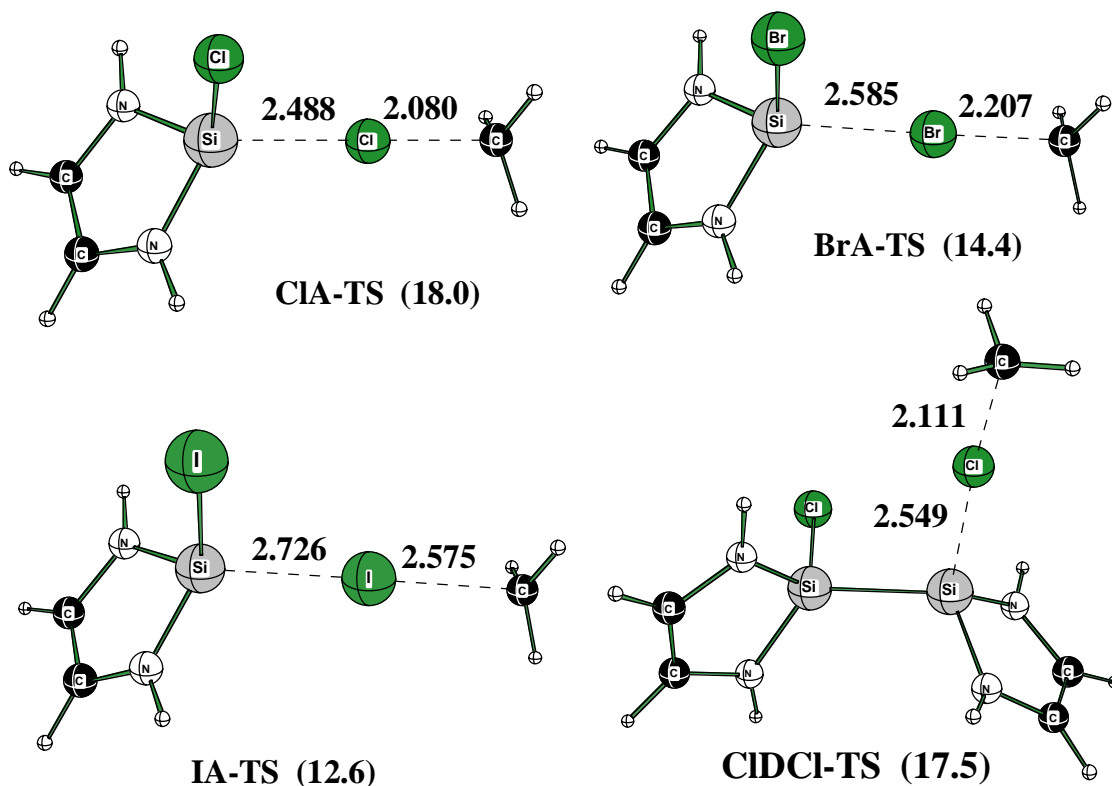
Figure 1.   (e) Geometrical parameters of transition states in the reaction of **X-A** with XCH$_3$ (**XA-TS**) and in the reaction of **Cl-D** with ClCH$_3$ (**ClDCl-TS**). Free energies in kcal/mol are given in parentheses with respect to reactants.

The products from concerted oxidative addition of XCH$_3$, **X-P1**, (X=Cl, Br, I) show very similar ring geometries. All have a localized C-C double bond (1.348-1.349 Å) and C-N single bonds (1.416-1.418 Å). The Si-N bond lengths in the series **A** → **Cl-A** → **Cl-P1** vary irregularly, 1.779 → 1.832 → 1.739 Å. In **A**, the Si-N bonds are short due to π conjugation from nitrogen lone pairs into the empty silicon orbital, while in **Cl-P1** the Si-N bonds are short due to the stronger Si-N single bonds (more s character).

Relative electronic energies (ΔE), enthalpies at 0K (ΔH$_{0K}$), enthalpies at 298K (ΔH$_{298K}$), and free energies at 298K (ΔG$_{298K}$) of all stationary points relevant to the reaction pathways are tabulated in Tables 3-5. Bond enthalpies of X-C in XCH$_3$ and X-Si bond enthalpies in **X-A** and

Table 2. Natural Atomic Charges (NPA) and Mulliken Spin Densities (MSD) of X-Si(NHCH)$_2$, (X=ep[a], CH$_3$, Cl, Br, I) Radicals Calculated at the B3LYP/SBS Level

	Si		X		NH		CH		(NHCH)$_2$[d]
	NPA	MSD	NPA	MSD	NPA	MSD	NPA	MSD	NPA
A	0.94	0.00			-0.60	0.00	0.13	0.00	-0.94
Me-A	1.26	0.62	-0.42[b]	-0.01[c]	-0.56	0.13	0.14	0.07	-0.84
Cl-A	1.11	0.33	-0.45	0.04	-0.51	0.20	0.18	0.14	-0.65
Br-A	1.04	0.29	-0.39	0.08	-0.51	0.19	0.18	0.14	-0.65
I-A	0.96	0.12	-0.32	0.24	-0.51	0.20	0.19	0.14	-0.65

a) Electron pair, designating **A**.

b) Methyl group charge; atomic charges on methyl hydrogens are summed with charge on carbon.

c) Spin density on methyl carbon.

d) Ring -(NHCH)$_2$ group.

Table 3. Relative Energies, Enthalpies, and Free Energies (kcal/mol) in the Reaction Profile for the Reaction of **A** with ClCH$_3$

Label	Species	ΔE_e	ΔH_{0K}	ΔH_{298K}	ΔG_{298K}
a1	3A+2ClCH$_3$	0.0	0.0	0.0	0.0
ats1	Cl-TS3+2A+ClCH$_3$	31.3	28.2	29.0	35.9
a2	Cl-A+CH$_3$+2A+ClCH$_3$	29.5	24.7	26.0	24.5
ats2	Me-TS+A+ClCH$_3$+Cl-A	29.4	25.1	26.5	30.5
a3	Me-A+A+ClCH$_3$+Cl-A	-0.1[a]	-1.4	-1.0	6.9
ats3	ClMeA-TS+A+Cl-A	6.9	4.8	5.7	21.4
a4	Cl-P1+CH$_3$+A+Cl-A	-22.4	-27.1	-25.7	-17.1
ats4	MeD-TS+ClCH$_3$+Cl-A	-0.6[a]	-1.7	-0.8	15.4
a5	Me-D+ClCH$_3$+Cl-A	-11.6	-12.8	-11.6	5.9
ats5	ClMeD-TS+Cl-A	-2.9	-4.9	-3.4	22.2
a6	Cl-P2+CH$_3$+Cl-A	-26.7	-31.5	-29.3	-11.2

a) Since the transition state is lower in energy than the reactant (**a3**→**ats4**), there must be an intervening intermediate. At the ΔE_e level, the **Me-A/A** complex is 2.7 kcal/mol more stable than **a3.**

Table 4.   Relative Energies, Enthalpies, and Free Energies (kcal/mol) in the Reaction Profile for the Reaction of **A** with $BrCH_3$

Label	Species	ΔE_e	ΔH_{0K}	ΔH_{298K}	ΔG_{298K}
b1	$3A+2BrCH_3$	0.0	0.0	0.0	0.0
bts1	**Br-TS3**+$2A$+$BrCH_3$	30.6	26.4	28.0	32.3
b2	**Br-A**+CH_3+$2A$+$BrCH_3$	30.4	25.8	27.2	25.7
bts2	**Me-TS**+A+$BrCH_3$+**Br-A**	30.3	26.3	27.7	31.7
b3	**Me-A**+A+$BrCH_3$+**Br-A**	0.9[a]	-0.3	0.3	8.0
bts3	**BrMeA-TS**+A+**Br-A**	2.4	1.0	1.7	18.0
b4	**Br-P1**+CH_3+A+**Br-A**	-18.3	-22.6	-21.1	-12.5
bts4	**MeD-TS**+$BrCH_3$+**Br-A**	0.4[a]	-0.5	0.4	16.6
b5	**Me-D**+$BrCH_3$+**Br-A**	-10.6	-11.6	-10.4	7.0
bts5	**BrMeD-TS**+**Br-A**	-7.8	-9.3	-7.8	18.1
b6	**Br-P2**+CH_3+**Br-A**	-23.6	-27.9	-25.7	-7.5

a)   Since the transition state is lower in energy than the reactant (**b3**→**bts4**), there must be an intervening intermediate. At the ΔE_e level, the **Me-A/A** complex is 2.7 kcal/mol more stable than **b3.**

Table 5.   Relative Energies, Enthalpies, and Free Energies (kcal/mol) in the Reaction Profile for the Reaction of **A** with ICH_3

Label	Species	ΔE_e	ΔH_{0K}	ΔH_{298K}	ΔG_{298K}
c1	$3A+2ICH_3$	0.0	0.0	0.0	0.0
c2	**I-A**+CH_3+$2A$+ICH_3	31.3	27.0	28.4	26.7
cts2	**Me-TS**+A+ICH_3+**I-A**	31.2	27.4	28.9	32.7
c3	**Me-A**+A+ICH_3+**I-A**	1.8[a]	0.9	1.5	9.1
cts3	**IMeA-TS**+A+**I-A**	0.0[a]	-1.3	-0.3	15.5
c4	**I-P1**+CH_3+A+**I-A**	-13.7	-17.5	-15.9	-7.6
cts4	**MeD-TS**+ICH_3+**I-A**	1.3[a]	0.7	1.6	17.6
c5	**Me-D**+ICH_3+**I-A**	-9.8[a]	-10.4	-9.2	8.1
cts5	**IMeD-TS**+**I-A**	-10.4[a]	-11.6	-10.0	16.2
c6	**I-P2**+CH_3+**I-A**	-19.9	-23.5	-21.3	-3.1

a)   Since the transition state is lower in energy than the reactant (**c3**→**cts3**, **c3**→**cts4**, and **c5**→**cts5**), there must be an intervening intermediate. At the ΔE_e level, the **Me-A**/ICH_3 complex is 1.8 kcal/mol more stable than **c3**; the **Me-A/A** complex is 2.7 kcal/mol more stable than **c3**; the **Me-D**/ICH_3 complex is 2.2 kcal/mol more stable than **c5**.

X-P1 (X=Cl, Br, I) are given in Table 6. The X-C bond enthalpies of methyl halides are in good agreement with well-known experimental values.[33]

Bond formation in **X-A** can be viewed as somewhere between two extremes. At one end of the spectrum, 2c-2e bond formation takes place after electron promotion, while at the other end, 2c-3e bond formation takes place without electron promotion. The preferred mode depends on the required promotion energy versus the strength of the 2c-2e bond. The promotion energy in **A** can be estimated from the singlet-triplet energy gap (ΔH^{s-t}) which was calculated to be 60.3 kcal/mol (ΔH^{s-t}_{298}). Thus, the new 2c-2e bond energy must be greater than 60.3 kcal/mol; otherwise 2c-3e bonding will be favored. The Si-X bond strength in **X-P1** should be a good estimate of full intrinsic Si-X bond strength since no promotion energy is required. As shown in Table 6, the BDE_{298} of Si-Cl, Si-Br, and Si-CH$_3$ in **X-P1** is larger than ΔH^{s-t}_{298} but the BDE_{298} of Si-I is only slightly larger. Therefore, in **A**, where a promotion of 60.3 kcal/mol is required, the 2c-2e bond enthalpy of 65 kcal/mol is barely enough to form a 2c-2e bond in **I-A**. Indeed, the Si-I bond strength in **X-A** is only 20.1 kcal/mol and is characterized by a much longer Si-I bond than found in **I-P1** and a much higher spin density on iodine (Table 2). Both properties indicate that the Si-I bond in **I-A** may have significant 2c-3e character.

In the series X=Cl, Br, I, the Si-X bond enthalpies in **X-A** (52.5 > 37.8 > 20.1 kcal/mol) and **X-P1** (103.1 > 86.3 > 65.9 kcal/mol) follow similar trends. The former bond enthalpies (**X-A**) are 50.6, 48.5, and 45.8 kcal/mol smaller than the latter (**X-P1**) for X=Cl, Br, I, respectively, due to the required promotion energy in **A** (estimated from the singlet-triplet splitting as 60.3 kcal/mol) which must take place before a 2c-2e Si-X bond can form. On the other hand, the 2c-2e Si-X bond in **X-P1** can form without any additional promotion energy.

In the currently proposed mechanism,[23] the first step in the reaction of XCH$_3$ with **A** is the concerted oxidative addition of XCH$_3$ (eq 1a). The monomer product, **X-P1** would follow immediately when X=I. The dimer product, **X-P2**, follows from the insertion of **A** into the X-Si

bond of **X-P1** (eq 1b). An alternative mechanism involving a dimer of **A** cannot occur because the dimer is not stable.[6]

The calculations below support a radical mechanism (eq 2-5). Free energy profiles in kcal/mol at 298K are given in Figure 2-4 for X=Cl, Br, and I. The profile is divided into three sections, the initiation step (eq 2), the common propagation step (eq 3), and the competition between the two propagation steps (eq 4 and 5) which lead to **X-P1** and **X-P2**, respectively.

(1a)

(1b)
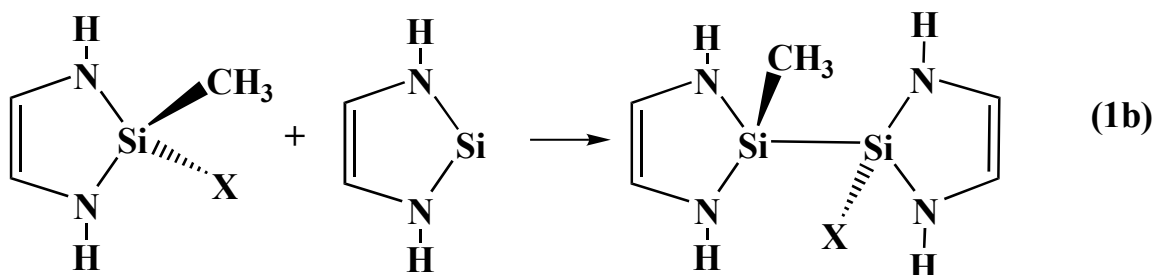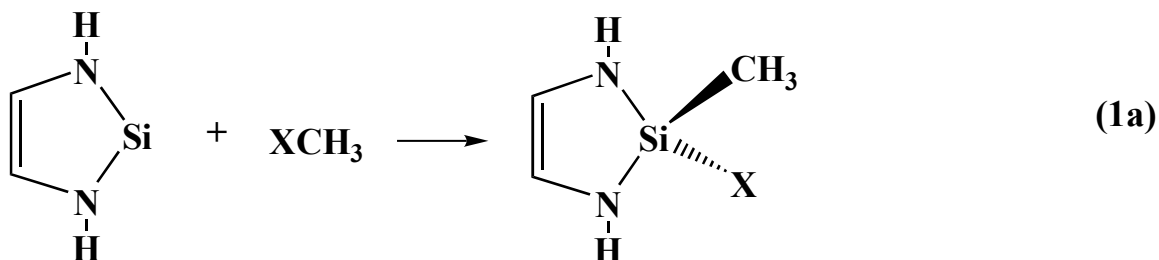
The concerted oxidative-addition barriers are compared with the lower-energy halogen-abstraction barriers in Table 7. The concerted transition states (**X-TS1** and **X-TS2**) have significantly higher free energies of activation than the halogen abstraction (**X-TS3**) free energy barrier. The latter barriers are 22.9, 16.0, and 22.8 kcal/mol lower in free energy than the concerted processes for X=Cl, Br, and I, respectively. In the case of iodine, a transition state for iodine abstraction could not be found. When X=Cl, Br, the activation free energy for halogen abstraction decreases (Table 8) while the reaction free energy increases. For X=I, the two trends meet, which explains why there is no transition state.

From the NBO analysis, there are three important donor-acceptor interactions in **X-TS1** and **X-TS2** (Table 9 and Figure 5). These are labeled **1**, **2**, and **3** and correspond to electron donation from the silicon lone pair (LP$_{Si}$) to the antibonding X-C orbital (σ^{*}_{X-C}), to electron

$$\text{(2)}$$

$$\text{(3)}$$

$$\text{(4)}$$

$$\text{(5a)}$$

$$\text{(5b)}$$
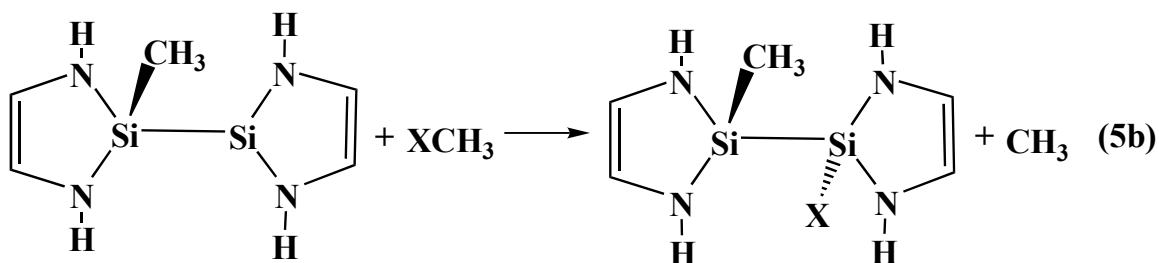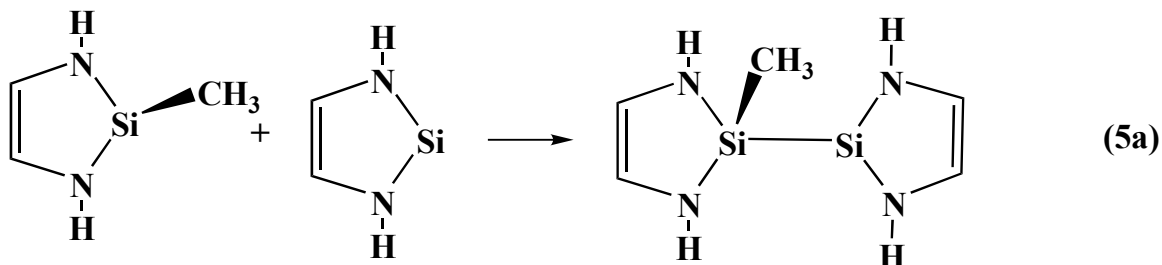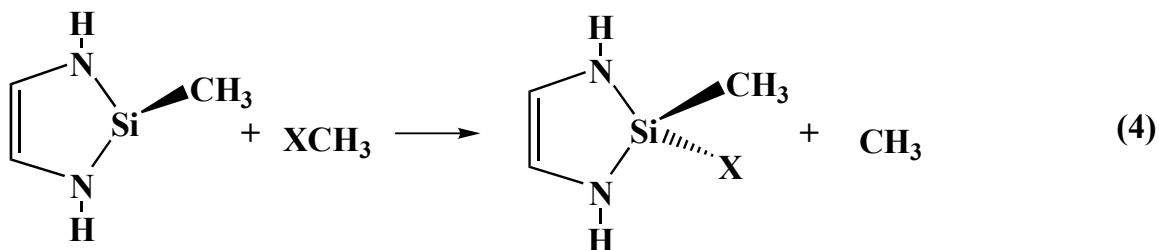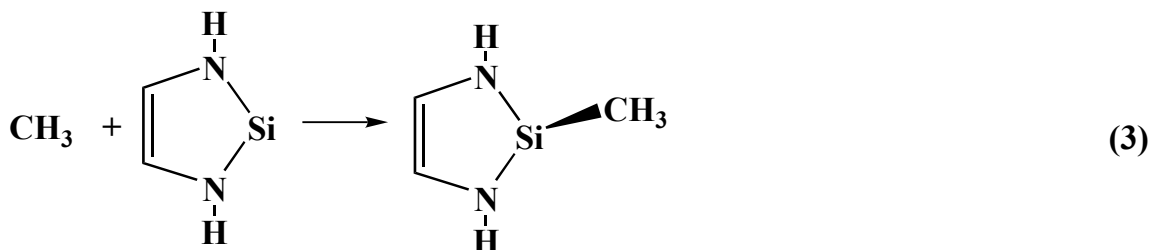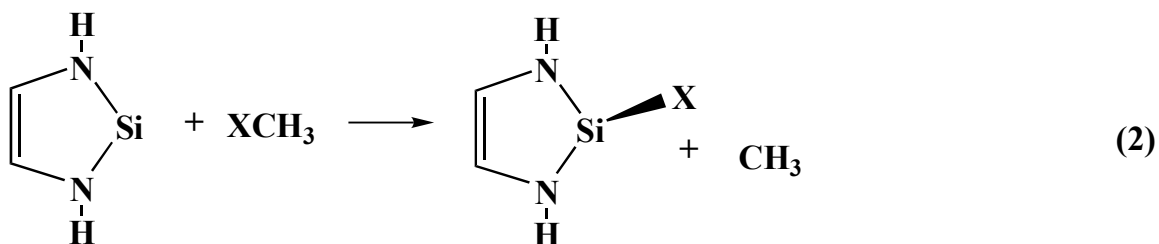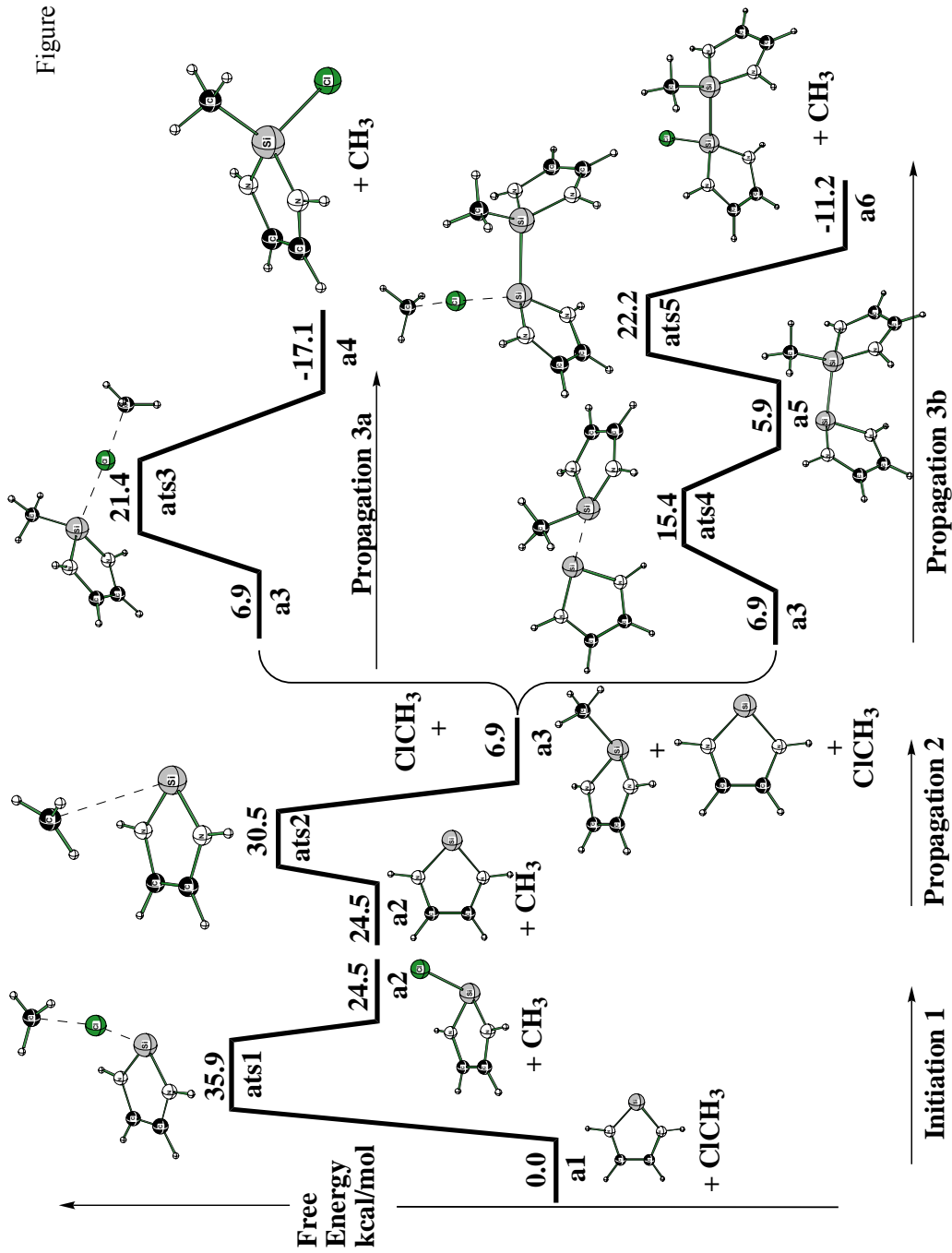
Figure 2. Schematic reaction free energy profile is presented for the reaction of **A** with ClCH$_3$ at the B3LYP/LBS//B3LYP/SBS level. The figure is divided into an initiation step (1), a common propagation step (2), and two competing propagation steps (3a and 3b). The initiation step produces a CH$_3$ radical which, in turn, adds to another bis(amino)silylene. The free energy of **Cl-A** + CH$_3$ and CH$_3$ + **Me-A** are shown at the same free energy so that free energies over the entire reaction can be compared. The entire list of species represented by the label (e.g. **a2**) is given in Table 3.

106
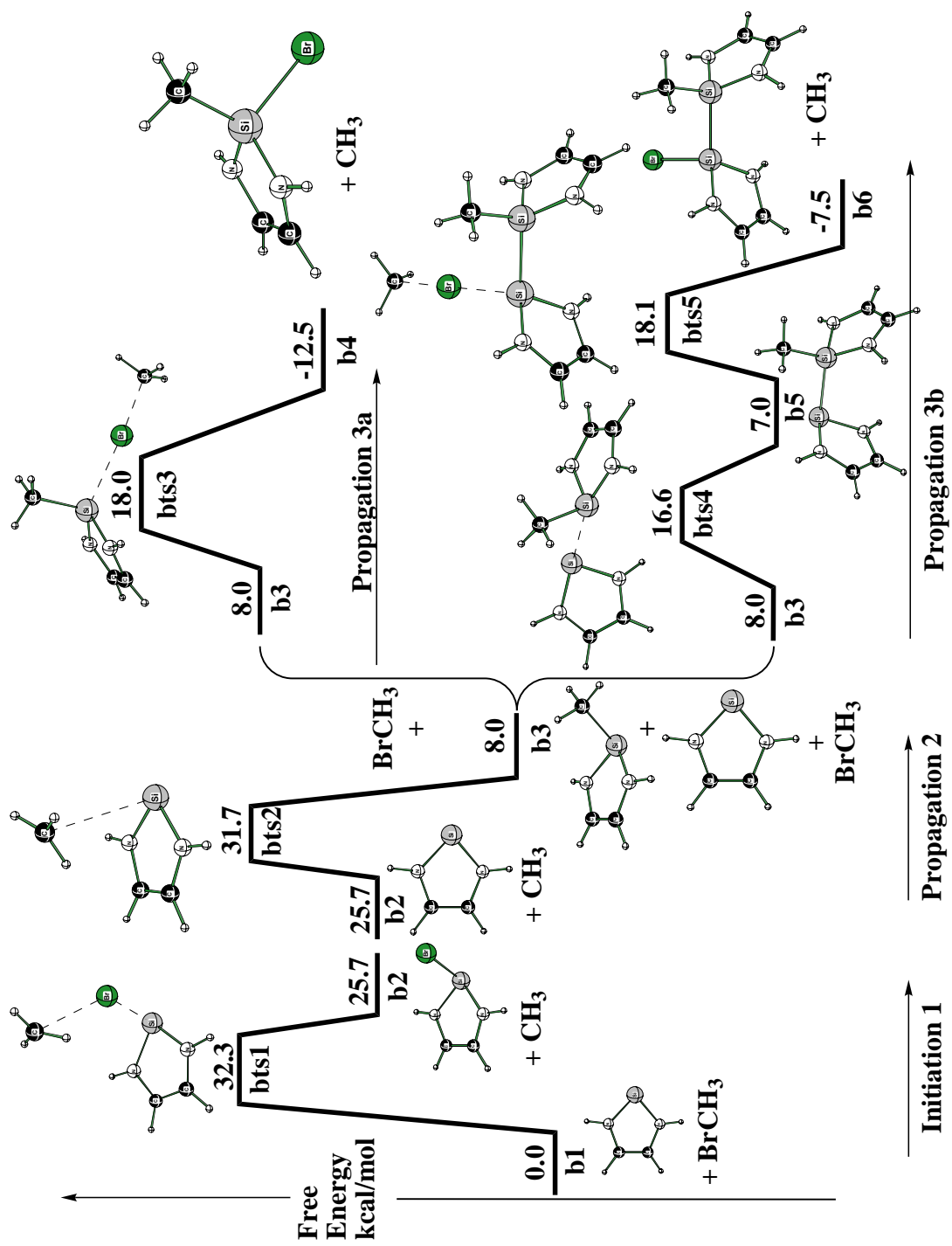
Figure 3.   Schematic reaction free energy profile is presented for the reaction of A with BrCH$_3$ at the B3LYP/LBS//B3LYP/SBS level.

107
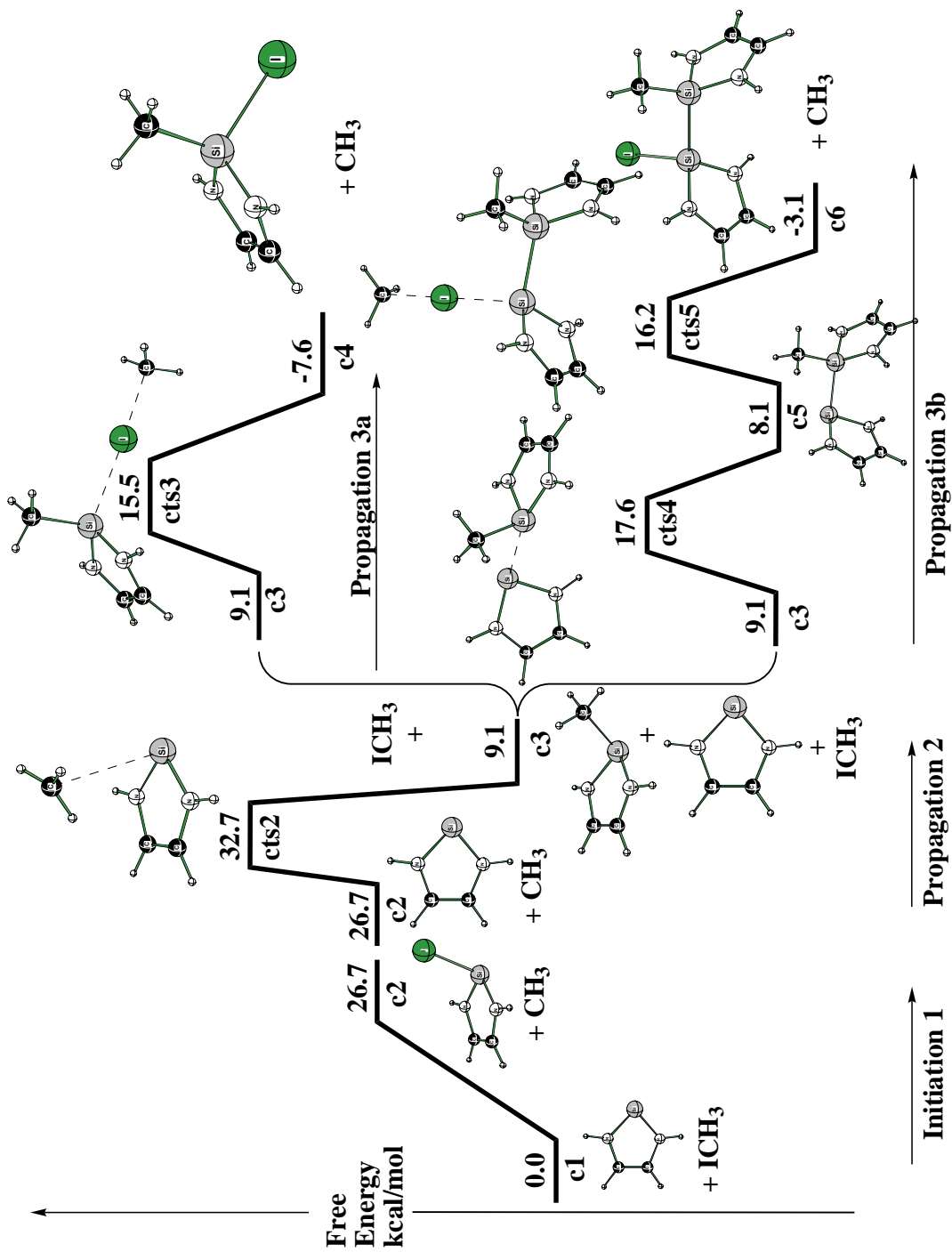
Figure 4.   Schematic reaction free energy profile is presented for the reaction of A with ICH_3 at the B3LYP/LBS//B3LYP/SBS level. The initiation step of A + ICH_3 does not have a transition state.

Table 6.   Bond Dissociation Energies (BDE), Bond Dissociation Enthalpies at 0K (BDE_0) and at 298K (BDE_{298}) Calculated at the B3LYP/LBS//B3LYP/SBS Level (kcal/mol)

Bond	BDE	BDE_0	BDE_{298}	Ref.[c]
Cl-CH_3	82.0	76.9	78.5	84.1[d]
Br-CH_3	68.2	63.5	65.0	70.0[d]
I—CH_3	51.5	47.1	48.5	56.6[d]
H_3C-Si[a]	29.6	26.1	26.9	
Cl-Si[a]	52.6	52.3	52.5	
Br-Si[a]	37.8	37.7	37.8	
I-Si[a]	20.2	20.1	20.1	
Si-Cl[b]	104.4	102.6	103.1	117.1 ± 2[e], 98.9[f]
Si-Br[b]	87.4	85.8	86.3	101.6 ± 2[e], 82.1[f]
Si-I[b]	67.0	65.5	65.9	82.2 ± 2[e], 62.7[f]
ClSi-CH_3[b]	81.4	76.4	77.6	
BrSi-CH_3[b]	79.2	74.3	75.5	94.2 ± 1[e], 70.5[f]
ISi-CH_3[b]	76.3	71.5	72.7	

a) From **Me-A** and **X-A** (X=Cl, Br, I) radical species.

b) From **X-P1** (X=Cl, Br, I).

c) Literature values for BDE_{298}.

d) Reference 33.

e) BDE of Me_3Si-X (X=CH_3, Cl, Br, I), from reference 34.

f) Bond energy terms of Si-X (X=C, Cl, Br, I) derived from least squares method. Reference 35.

Table 7.   Comparison of Free Energies of Activation (kcal/mol) for Concerted Oxidative Addition with Halogen Abstraction Reaction for **A** + XCH_3

	X=Cl	X=Br	X=I
X-TS1[a]	60.0	57.0	63.1
X-TS2[a]	58.8	48.3	49.5
X-TS3[b]	35.9	32.3	26.7[c]

a) Oxidative addition.

b) Halogen abstraction.

c) There is no transition state for halogen atom abstraction by **A** from ICH_3. The free energy of **I-A** plus CH_3 is 26.7 kcal/mol.

Table 8.   Predicted Differences in Free Energies of Activation ($\Delta\Delta G_{298}$, kcal/mol) for

Formation of CH_3 and **I-Si** Radical from $ClCH_3$ and $BrCH_3$ at

B3LYP/LBS//B3LYP/SBS Level

X	X=Cl	X=Br	X=I
X-TS3	35.9	32.3	---
CH_3 + **X-A**	24.5	25.7	26.7
$\Delta(\Delta G_{298})$	11.4	6.6	~0.0

X-TS1   **X-TS2**
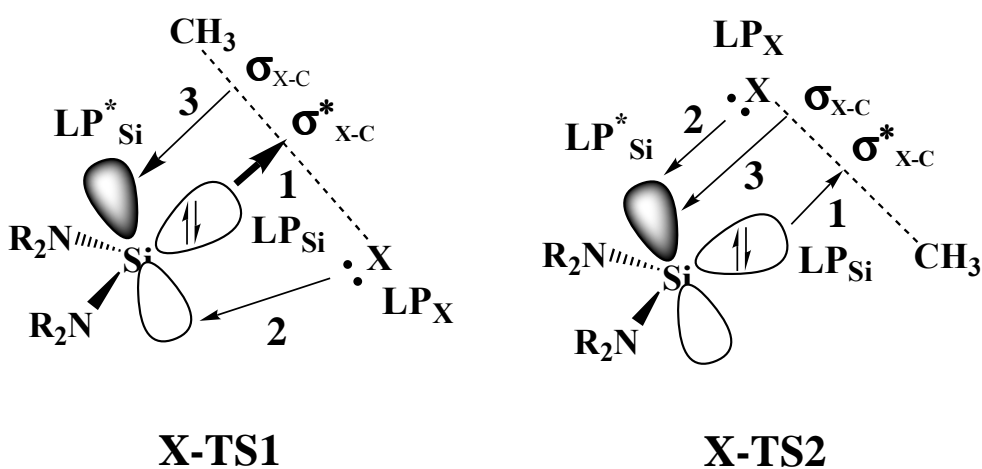
Figure 5.   Orbital interactions are depicted that are analyzed by NBO in Table 9.

Table 9.   Orbital Interaction Energies (kcal/mol) from Second Order Perturbation Theory

Analysis in NBO Analysis at the HF/LBS Level

	Orbital Interaction		Cl-TS1	Cl-TS2	Br-TS1	Br-TS2	I-TS1	I-TS2
	Donor	Acceptor						
1[a]	LP_{Si}	$\sigma^*_{X\text{-}C}$[b]	42.4	58.1	31.6	13.0	25.1	40.1
2[a]	LP_X	LP^*_{Si}	0.4	62.6	0.4	43.1	0.3	21.1
3[a]	$\sigma_{X\text{-}C}$[b]	LP^*_{Si}	10.3	22.4	12.3	51.8	14.9	35.4

a)   For depiction of orbital interactions see Figure 5.

b)   The σ and σ^* X-CH_3 bonds were defined by using CHOOSE and DEL keywords within

the NBO analysis program.

donation from the lone pair orbital on X (LP_X) to the empty orbital on silicon (LP^*_{si}), and to

electron donation from the X-C bonding orbital (σ_{X-C}) to the empty orbital on silicon (LP^*_{si}),

respectively (Table 9). In **X-TS1**, the stable bis(amino)silylene is acting as the Lewis base, where

interaction **1** is larger than **2**+**3**. The decrease of interaction **1** in **X-TS1** as **X** is changed from Cl

to I (Cl 42.4 kcal/mol; Br 31.6 kcal/mol; I 25.1 kcal/mol) can be attributed to the destabilization

of the X-C σ^* orbital which reduces its acceptor ability. On the other hand, the stable

bis(amino)silylene is acting as a Lewis acid in **X-TS2** as shown by the combined interactions of **2**

and **3** in which the acceptor orbital is LP^*_{si}. The largest interaction (**2**+**3**) occurs for X=Br (94.9

kcal/mol), followed by X=Cl (85.0 kcal/mol) and X=I (56.9 kcal/mol). Indeed, the lowest

concerted free energy barrier for oxidative addition of XCH_3 to **A** occurs via **Br-TS2**. There has

been extensive discussion in the literature about the increased Lewis basicity of **A** relative to

dialkylsilylenes. However, in the concerted oxidative addition of XCH_3 to the stable

bisaminosilylene **A**, it appears that the silylene is still acting as the Lewis acid. It is interesting

that the Lewis acid-Lewis base character of **A** can be captured by the two concerted transition

states **X-TS1** and **X-TS2**. For X=Cl, the two transition states are separated by only 1.2 kcal/mol

in free energy. This difference increases to 8.7 kcal/mol for X=Br and 13.6 kcal/mol for X=I.

The increased separation between the two transition states (**X-TS1** and **X-TS2**) for X=I is likely

due to the soft-soft acid-base character between iodine (soft base) and **A** (soft acid) in **I-TS2**. It

must be emphasized that, while interesting from a pedagogical point of view, the concerted

oxidative transition states, **X-TS1** and **X-TS2**, do not play a role in the reaction mechanism. For

all three reactions, X=Cl, Br, and I, the halogen abstraction reaction, **X-TS3** is lower in free

energy than the concerted oxidative addition (Table 7).

It has been reported that bis(amino)silylenes are electronically similar to trivalent

phosphorus compounds (eq 6,7),[17,37] because of strong π-conjugation. We suggest that a better

analogy might be disilene, $R_2Si=SiR_2$ (Scheme 3). Kira has characterized the reaction of

$$X_3P : + \; Y \cdot \longrightarrow \; X_3\overset{\cdot}{P}—Y \qquad\qquad (6)$$

$$(7)$$
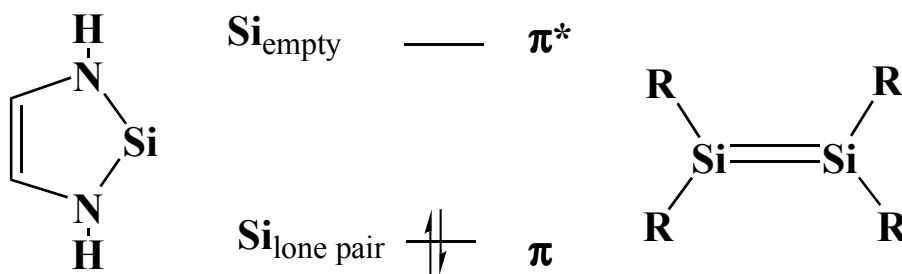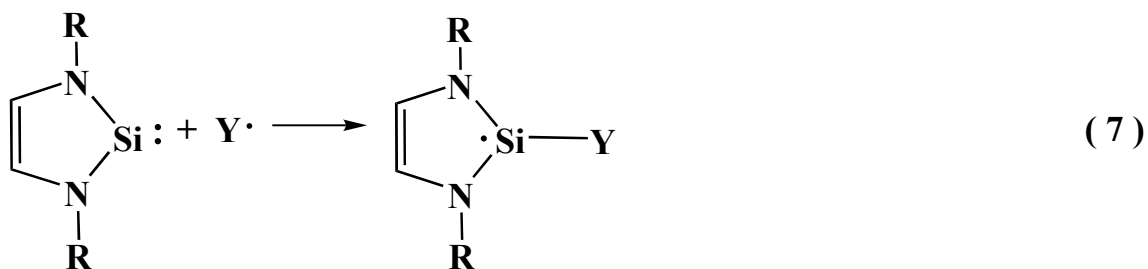
Scheme 3

$R_2Si=SiR_2$ with R'X as proceeding through a "bimolecular abstraction mechanism".[13] In fact, in the reaction of $(i\text{-}Pr_3Si)_2Si=Si(i\text{-}Pr_3Si)_2$ with t-BuCl, the radical product is stable and has been identified by ESR.[38]

More supportive evidence for the analogue between bis(amino)silyene and disilene can be found from the nature of the transition state for halogen atom abstraction by both compounds. By comparing rate constants and exothermicities for the reactions of disilene with a series of chlorine- and bromine-containing molecules, it was concluded[13,38] that the transition states are "late" (silicon-halogen bond formation and halogen-carbon bond cleavage are well-advanced). In the reaction of bis(amino)silyene with halomethanes, the transition states (**X-TS3**) are also "late" as judged by short forming Si-X and long breaking X-C bonds (Figure 1d,e). In contrast to the reactions of **A** (bis(amino)silyene) with XCH$_3$ which are "late", the reactions of **Me-A** with XCH$_3$

are "early" as judged by the long forming Si-X bonds and the short breaking X-C bonds in the transition states **XMeA-TS** (Figure 1d). Thus, the addition of the methyl substituent to **A** (**A** + CH$_3$ → **Me-A**) makes the halogen abstraction reactions much more exothermic and changes the transition states from "late" to "early".

The free energy barrier for halogen abstraction (forming two radical products) is clearly lower than the concerted oxidative addition barriers as illustrated in Table 7 for the three halomethanes considered, ClCH$_3$, BrCH$_3$, and ICH$_3$. In Figures 2-4, we present the free energies for the radical mechanism to **X-P1** and **X-P2**, X=Cl, Br, I.

In the initiation step, a halogen atom is abstracted by bis(amino)silylene (**A**), leaving behind a methyl radical. The methyl radical can react with another methyl radical to form ethane (chain terminating), react with the solvent (hexane or benzene) to form side products, react with XCH$_3$ in a degenerate reaction (CH$_3$ + X-CH$_3$ → CH$_3$-X + CH$_3$), or (much more likely) react with **A**. Reaction with **A** (labeled "Propagation 2"), a common step for all halomethanes, has a free energy barrier of 6.0 kcal/mol. The product, **Me-A**, can react with X-CH$_3$ ("Propagation 3a") or with another **A** ("Propagation 3b"). The competition between 3a and 3b will determine which products are formed. In the reaction of ClCH$_3$ with **A**, the two relevant free energies are "**ats3**" and "**ats5**", 21.4 and 22.2 kcal/mol. The calculation would predict a mixture of **Cl-P1** and **Cl-P2** since the free energy barriers are very similar.

In the chain mechanism, we depict the **Me-D** radical reacting with ClCH$_3$ to form **Cl-P2** plus CH$_3$ (Propagation 3b). In reality, there is the possibility that **Me-D** can react with another **A** to form **Me-T** ("**T**" for trimer). The free energy barrier for the **Me-D** + **A** → **Me-T** reaction is lower than for the **Me-D** + ClCH$_3$ → **Cl-P2** reaction (9.6 versus 16.3 kcal/mol), but the reaction is nonspontaneous by 5.9 kcal/mol.[39] When we consider that the experiments involve **1** with bulky *t*-butyl groups on nitrogen rather than **A**, the possibility for forming the trimer adduct is even less likely.

This prediction agrees with the experimental result where reaction of **1** with CCl$_4$ afforded a mixture of products.[14b] However, the only reported product of the reaction of **1** (not **A**) with CH$_2$Cl$_2$ or CHCl$_3$ (not ClCH$_3$) is the disilane product (**Cl-P2**). It should be noted that solvation effects in hexane or benzene (which have not been included in the present study) are expected to be small but could be large enough to affect the outcome of the reaction. Of course, the reaction can be "pushed" toward one product or the other by changing the initial ClCH$_3$:**A** ratio.

In the BrCH$_3$-containing pathway 3a (Figure 3, **Me-A** + BrCH$_3$), the transition state has a free energy of 18.0 kcal/mol, very similar to the free energy from pathway 3b (18.1 kcal/mol). The two pathways are expected (and found) to be competitive. In the ICH$_3$-containing pathway 3a (Figure 4, **Me-A** + ICH$_3$), the transition state has a smaller free energy than the pathway to disilane products (**I-P2**), 15.5 versus 17.6 kcal/mol. In addition, nonstatistical behavior (see below) may lead to the formation of **I-P1** by the capture of the CH$_3$ radical released in the initiation step.

It is very reasonable that the two barriers for addition of XCH$_3$ to **Me-A** or **Me-D** should be similar. In both transition states, the halogen atom is abstracted by a silicon atom in a similar chemical environment. For **Me-A** + XCH$_3$, the substituent on the trivalent silicon is methyl while in **Me-D** + XCH$_3$, the substituent is methyl-bis(amino)silylene. We also explored the fate of **X-A** which should lead to minor products, perhaps below the detection limit in the experimental studies. The reaction of **X-A** with **A** has free energy barriers of 8.3, 9.0, and 8.4 kcal/mol for X=Cl, Br, and I (for structures see: **XD-TS**, Figure 1). In analogy with **Me-D**, the most likely reaction of **Cl-D** is with ClCH$_3$ to give the dichloro version of the disilane product. The free energy barrier for this reaction is 17.5 kcal/mol (Figure 1e). The alternative reactions of **X-A** are with XCH$_3$ which have free energy barriers of 18.0, 14.4, and 12.6 kcal/mol for X=Cl, Br, and I, respectively, to form the dihalogen version of **X-P1** (Figure 1e). Thus, there may be dihalogen
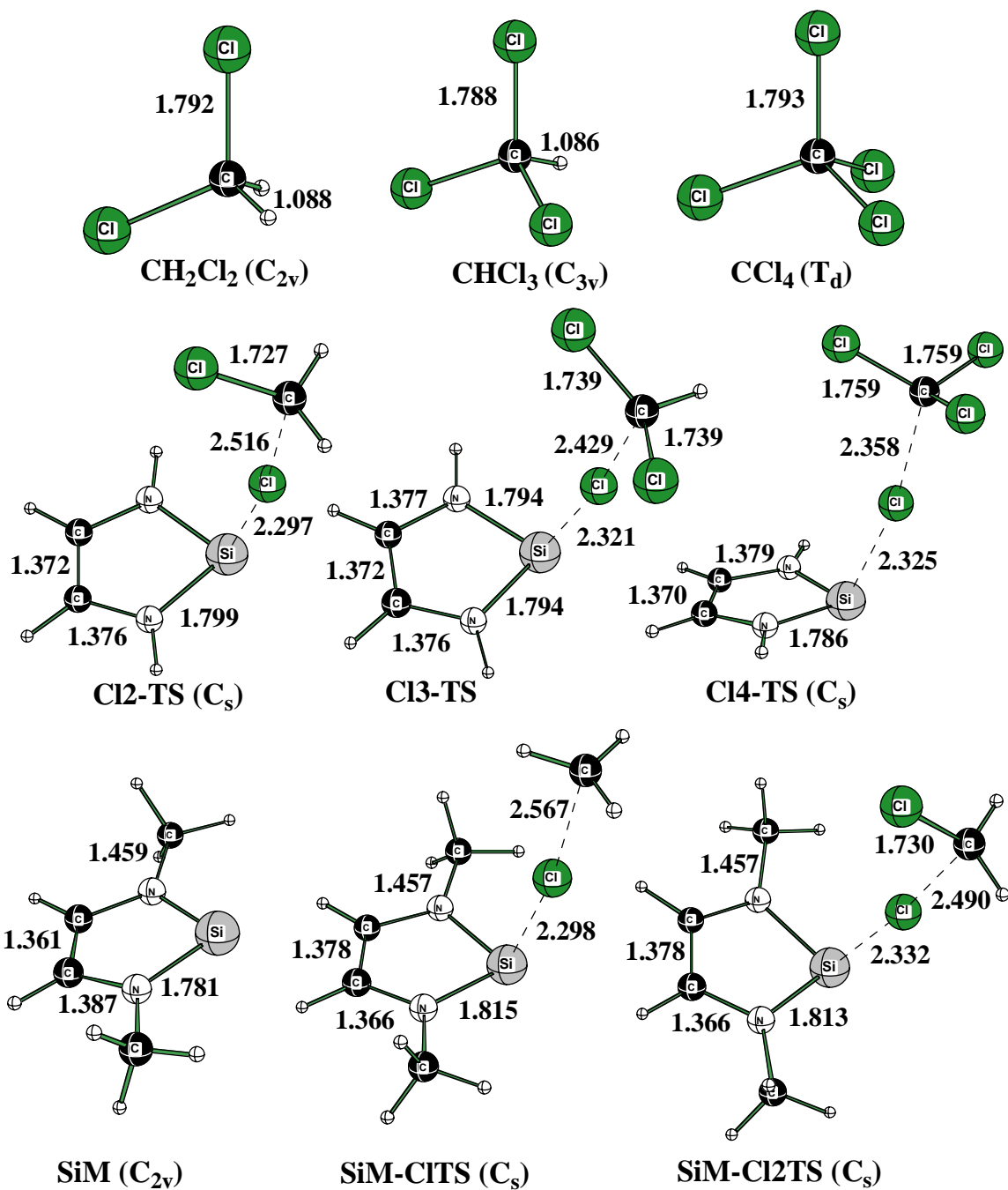
Figure 6. Geometries (B3LYP/6-31+G(d)) of reactants CH_2Cl_2, $CHCl_3$, and CCl_4 and the transition states for the initiation steps (chlorine atom abstraction by **A**) **Cl2-TS**, **Cl3-TS**, and **Cl4-TS**, and geometries of reactant **SiM** and the transition states for the initiation steps of chlorine atom abstraction by **SiM**, (**SiM-ClTS** and **SiM-Cl2TS**).

products produced (i.e. two halogens on **X-P1** and **X-P2**) in the reaction of $XCH_3 + $ **A**, but the concentrations may be low since **X-A** is only generated in the initiation step.

One shortcoming of our model is that the free energy barriers for the initiation steps are still too high to explain the experimental observation where the reactions proceed at room temperature. This can be explained by the fact that our model system is not the same as the observed reaction. Most of the reported reactions are those of stable silylene **1** with CH_2Cl_2, $CHCl_3$, and CCl_4. Therefore, the effect of additional halogen atoms on the entering methyl carbon was examined in the reaction of **A** with CH_2Cl_2, $CHCl_3$, and CCl_4, as well as the effect of additional methyl groups on the ring nitrogen atoms in the silylene (i.e. N,N'-dimethyl derivative, **SiM**) in the reaction with $ClCH_3$. In addition, to confirm the additivity of these effects, an investigation of the reaction of **SiM** with CH_2Cl_2 was also carried out. Optimized geometries of the reactants and transition states are given in Figure 6, while the calculated activation barriers are tabulated in Table 10. The additional halogens on the methyl group lower the activation free energy barrier by about 5 kcal/mol per chlorine ($CH_{4-n}Cl_n$: n=1,2,3,4; $\Delta G^{\ddagger}_{298K}$= 35.9, 31.5, 26.2, 19.9 kcal/mol, respectively). The lowering of the free energy barriers can be attributed to the stabilizing effect of the chlorine on the forming methyl radical.

Two methyl substituents on the ring nitrogen atoms cause the activation free energy barrier to be lower by about 2 kcal/mol. The electron donation from the methyl groups to the bis(amino)silylene ring enhances the electron delocalization over the five-membered ring system and stabilizes the transition state. The two effects (methyl groups on nitrogen and additional chlorine atoms on carbon) are additive, and the activation free energy barrier for the reaction of **SiM** with CH_2Cl_2 ($\Delta G^{\ddagger}_{298K}$= 29.6 kcal/mol) is 6.3 kcal/mol lower than that of the model reaction. Thus, if we consider the stable silylene **1** reacting with CH_2Cl_2, $CHCl_3$, or CCl_4, the initiation free energy barriers might be reasonable for a reaction that occurs at room temperature.

116

Table 10. Comparison of Activation Energies, Enthalpies, and Free Energies (kcal/mol) in the Initiation Steps for the Reaction of **A** with $ClCH_3$, CH_2Cl_2, $CHCl_3$ or CCl_4 and for the Reaction of **SiM** with $ClCH_3$ and CH_2Cl_2

	ΔE_e	ΔH_{0K}	ΔH_{298K}	ΔG_{298K}
Cl-TS3	31.3	28.2	29.0	35.9
Cl2-TS	25.7	23.5	24.3	31.5
Cl3-TS	19.5	18.2	19.0	26.2
Cl4-TS	12.7	12.1	12.8	19.8
SiM-ClTS	30.0	26.8	27.9	33.8
SiM-Cl2TS	24.1	21.8	22.8	29.6

Cl-TS3
231i cm^{-1}
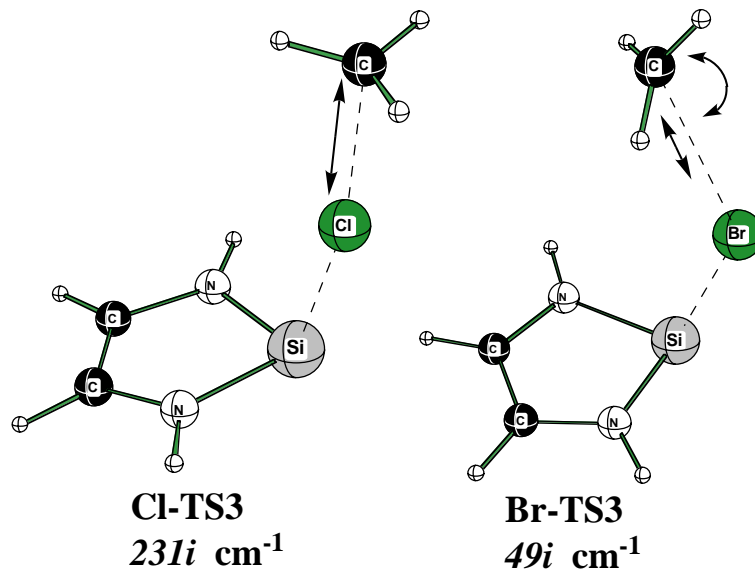
Br-TS3
49i cm^{-1}

Figure 7. Transition vectors of the two transition states (**Cl-TS3** and **Br-TS3**) which indicate the ejection of a methyl radical during halogen abstraction. A transition state does not exist in the abstraction of iodine from ICH_3 by **A**.

One experimental peculiarity of the RCl + **A** reaction is that R=*t*-Bu and R=$CHCl_2$ lead to different products. While $CHCl_3$ leads to **Cl-P2** (with a $CHCl_2$ substituent rather than CH_3), *t*-BuCl leads to the corresponding **Cl-P1** product, the same product observed with ICH_3. We

think the answer to this riddle may come from nonstatistical kinetic models.[40] In the transition

state for the initiation step, the transition vector ($231i$ cm^{-1}) is a Cl-CH$_3$ bond stretch (Figure 7).

The radical products are 3.0 kcal/mol lower in enthalpy (Table 1) than the transition state and the

excess energy will become kinetic energies of two separating species such that the methyl radical

will leave the vicinity of the **Cl-A** radical. If the reaction of *t*-BuCl follows a similar path, the 3.0

kcal/mol of enthalpy may be absorbed by vibrations of the *t*-Bu group such that the *t*-Bu group

may not depart the vicinity of **Cl-A** and be captured to form the corresponding **Cl-P1** product.

Another reason why R=*t*-Bu leads to the monomer is due to steric congestion in the

transition state for formation of the dimer. In the case of *t*-BuCl reacting with **1**, there are five *t*-

Bu groups in the transition state (**MeD-TS**) with significant crowding between the two units. In

this case, there is an advantage of propagation step 3a over 3b.

4.4 Conclusion

The present calculations on the reaction of bis(amino)silylene with halomethane indicate

a radical reaction mechanism rather than a concerted oxidative addition of the halomethane. The

free energies of activation for the radical mechanism are 16 to 23 kcal/mol lower than for the

concerted pathway. The chain pathway includes the initiation step, which produces a halogen-

addition product and a methyl radical and propagation steps which consume one methyl radical

and produce one methyl radical. The monomer and dimer products from the halomethane

addition arise from the competition between two propagation steps. In one pathway, the

halomethane adds to the methyl-bis(amino)silylene radical (**Me-A**), while in the competing

pathway, the methyl-bis(amino)silylene radical first reacts with another bis(amino)silylene which,

in turns, reacts with halomethane to abstract a halogen atom. Since the competing pathways are

within a few kcal/mol of each other, secondary effects (such as solvation) may have decisive roles

in determining the outcome of the reaction.

The observation that $CHCl_3$ and t-BuCl lead to different products can be explained within the present mechanism if nonstatisical effects are important. The large manifold of vibrational modes in the t-Bu radical may couple efficiently with the transition vector allowing the t-Bu radical to be "captured" in a single reaction step. A complete understanding of the reaction mechanism may require trajectory studies of branching propagation steps. However, these studies are beyond the scope of the present work.

4.5 References

(1)   Denk, M.; Lennon, R.; Hayashi, R.; West, R.; Belyakov, A. V.; Verne, H. P.; Haaland, A.; Wagner, M.; Metzler, N. *J. Am. Chem. Soc.* **1994**, *116*, 2691.

(2)   (a) Heinemann, C.; Müller, T.; Apeloig, Y.; Schwarz, H. *J. Am. Chem. Soc.* **1996**, *118*, 2023. (b) Veszprémi, T.; Nyulászi, L; Jajgató, B.; Heinicke, J. *THEOCHEM*, **1998**, *431*, 1.

(3)   (a) Boehme, C.; Frenking, G. *J. Am. Chem. Soc.* **1996**, *118*, 2039. (b) Boehme, C.; Frenking, G. *Organometallics* **1998**, *17*, 5801.

(4)   Heinemann, C.; Herrmann, W. A.; Thiel, W. *J. Organomet. Chem.* **1994**, *475*, 73.

(5)   West, R.; Buffy, J. J.; Haaf, M.; Müller, T.; Gehrhus, B.; Lappert, M. F.; Apeloig, Y. *J. Am. Chem. Soc.* **1998**, *120*, 1639.

(6)   Oláh, J.; Veszprémi, T. *J. Organomet. Chem.* **2003**, *686*, 112.

(7)   (a) Apeloig, Y.; Karni, M. In *The Chemistry of Organic Silicon Compounds*; Rappoport, Z., Apeloig, Y., Eds, Wiley: New York, 1998; Vol. 2. Part 1, p 1. (b) Tokitoh, N. *Acc. Chem. Res.* **2004**, *37*,86.

(8)   (a) Arduengo, A. J., III; Bock, H.; Chen, H.; Denk, M.; Dixon, D. A.; Green, J. C.; Herrmann, W. A.; Jones, N. L.; Wagner, M.; West, R. *J. Am. Chem. Soc.* **1994**, *116*, 6641. (b) Denk, M.; Green, J. C.; Metzler, N.; Wagner, M. *J. Chem. Soc. Dalton Trans.* **1994**, 2405. (c) Blakeman, P.; Gehrhus, B.; Green, J. C.; Heinicke, J.; Lappert, M. F.; Kindermann, M.; Veszprémi, T. *J. Chem. Soc. Dalton Trans.* **1996**, 1475. (d) Pause, L.; Robert, M.; Heinicke, J.; Kühl, O. *J. Chem. Soc. Perkin Trans. 2* **2001**, 1383. (e) Dhiman, A.; Müller, T.; West, R.; Becker, J. Y. *Organometallics* **2004**, *23*, 5689.

(9)   Urquhart, S. G.; Hitchcock, A. P.; Lehmann, J. F.; Denk, M. *Organometallics* **1998**, *17*, 2352.

(10)   (a) Lehmann, J. F.; Urquhart, S. G.; Ennis, L. E.; Hitchcock, A. P.; Hatano, K.; Gupta, S.; Denk, M. K. *Organometallics* **1999**, *18*, 1862. (b) Naka, A.; Hill, N. J.; West, R. *Organometallics* **2004**, *23*, 6330.

(11)   Leites, L. A.; Bukalov, S. S.; Denk, M.; West, R.; Haaf, M. *J. Mol. Struct.* **2000**, *550*, 329.

(12)   Gaspar, P. P.; West, R. In *The Chemistry of Organic Silicon Compounds*; Rappoport, Z., Apeloig, Y., Eds, Wiley: New York, 1998; Vol. 2. Part 3, p 2463.

(13)   Kira, M. *Pure Appl. Chem.* **2000**, *72*, 2333.

(14)   (a) Gehrhus, B.; Lappert, M. F. *J. Organomet. Chem.* **2001**, *617*, 209. (b) Haaf, M.; Schmedake, T. A.; West, R. *Acc. Chem. Res.* **2000**, *33*, 704. (c) Tokitoh, N.; Okazaki, R. *Coord. Chem. Rev.* **2000**, *210*, 251.

(15)   Amoroso, D.; Haaf, M.; Yap, G. P. A.; West, R.; Fogg, D. E. *Organometallics* **2002**, *21*, 534.

(16)   Avent, A. G.; Gehrhus, B.; Hitchcock, P. B.; Lappert, M. F.; Maciejewski, H. *J. Organomet. Chem.* **2003**, *686*, 321.

(17)   Schmedake, T. A.; Haaf, M.; Paradise, B. J.; Millevolte, A. J.; Powell, D. R.; West, R. *J. Organomet. Chem.* **2001**, *636*, 17.

(18)   Haaf, M.; Schmedake, T. A.; Paradise, B. J.; West, R. *Can. J. Chem.* **2000**, *78*, 1526.

(19)   (a) *Carbene Chemistry: from fleeting intermediates to powerful reagents*, Bertrand, G., Ed., Marcel Dekker: New York, 2002. (b) *Reactive Intermediate Chemistry*, Moss, R. A., Platz, M. S., Jones, M., Jr., Eds., Wiley-Interscience: Hoboken, N.J., 2004.

(20)   Ishida, S.; Iwamoto, T.; Kabuto, C.; Kira, M. *Chem. Lett.* **2001**, 1102.

(21)   Haaf, M.; Schmiedl, A.; Schmedake, T. A.; Powell, D. R.; Millevolte, A. J.; Denk, M.; West, R. *J. Am. Chem. Soc.* **1998**, *120*, 12714.

(22)   Moser, D. F.; Bosse, T.; Olson, J.; Moser, J. L.; Guzei, I. A.; West, R. *J. Am. Chem. Soc.*
         2002, *124*, 4186.

(23)   (a) Su, M.-D. *J. Am. Chem. Soc.* **2003**, *125*, 1714. (b) Su, M.-D. *Chem. Phys. Lett.* **2003**,
         374, 385.

(24)   Joo, H.; McKee, M. L. *J. Phys. Chem. A* **2005**, *109*, 3728.

(25)   (a) Koch, W.; Holthausen, M. C. *A Chemist's Guide to Density Functional Theory*,
         Wiley: New York, 2001. (b) Becke, A. D. *J. Chem. Phys.* **1993**, *98*, 5648. (c) Lee, C.;
         Yang, W.; Parr, R. G. *Phys. Rev. B* **1988**, *37*, 785. (d) Miehlich, B.; Savin, A.; Stoll, H.;
         Preuss, H. *Chem. Phys. Lett.* **1989**, *157*, 200.

(26)   *Gaussian03, (Revision B.4)*, Frisch, M. J.; Trucks, G. W.; Schlegel, H. B.; Scuseria, G.
         E.; Robb, M. A.; Cheeseman, J. R.; Montgomery, J. A. Jr.; Vreven, T.; Kudin, K. N.;
         Burant, J. C.; Millam, J. M.; Iyengar, S. S.; Tomasi, J.; Barone, V.; Mennucci, B.; Cossi,
         M.; Scalmani, G.; Rega, N.; Petersson, G. A.; Nakatsuji, H.; Hada, M.; Ehara, M.;
         Toyota, K.; Fukuda, R.; Hasegawa, J.; Ishida, M.; Nakajima, T.; Honda, Y.; Kitao, O.;
         Nakai, H.; Klene, M.; Li, X.; Knox, J. E.; Hratchian, H. P.; Cross, J. B.; Adamo, C.;
         Jaramillo, J.; Gomperts, R.; Stratmann, R. E.; Yazyev, O.; Austin, A. J.; Cammi, R.;
         Pomelli, C.; Ochterski, J. W.; Ayala, P. Y.; Morokuma, K.; Voth, G. A.; Salvador, P.;
         Dannenberg, J. J.; Zakrzewski, V. G.; Dapprich, S.; Daniels, A. D.; Strain, M. C.; Farkas,
         O.; Malick, D. K.; Rabuck, A. D.; Raghavachari, K.; Foresman, J. B.; Ortiz, J. V.; Cui,
         Q.; Baboul, A. G.; Clifford, S.; Cioslowski, J.; Stefanov, B. B.; Liu, G.; Liashenko, A.;
         Piskorz, P.; Komaromi, I.; Martin, R. L.; Fox, D. J.; Keith, T.; Al-Laham, M. A.; Peng,
         C. Y.; Nanayakkara, A.; Challacombe, M.; Gill, P. M. W.; Johnson, B.; Chen, W.; Wong,
         M. W.; Gonzalez, C.; Pople, J. A. Gaussian, Inc., Pittsburgh PA, 2003.

(27)   (a) Hay, P. J.; Wadt, W. R. *J. Chem. Phys.* **1985**, *82*, 270. (b) Wadt, W. R.; Hay, P. J. *J.
         Chem. Phys.* **1985**, *82*, 284. (c) Hay, P. J.; Wadt, W. R. *J. Chem. Phys.* **1985**, *82*, 299.

(28)   *MOLDEN,* Schaftenaar, G.; Noordik, J. H. *J. Comput.-Aided Mol. Design* **2000**, *14*, 123.

(29)   (a) Gonzalez, C.; Schlegel, H. B. *J. Chem. Phys.* **1989**, *90*, 2154. (b) Gonzalez, C.;

          Schlegel, H. B. *J. Phys. Chem.* **1990**, *94*, 5523.

(30)   Dolg, M.; Stoll, H.; Preuss, H.; Pitzer, R. M. *J. Phys. Chem.* **1993**, *97*, 5852.

(31)   Reed, A.; Curtiss, L. A.; Weinhold, F. *Chem. Rev.* **1988**, *88*, 899.

(32)   Becker, J. S.; Staples, R. J.; Gordon, R. G. *Cryst. Res. Technol.* **2004**, *39*, 85.

(33)   James, A.; Lord, M. *VNR Index of Chemical and Physical Data*; Van Nostrand Reinhold:

          New York, 1992, 485.

(34)   Becerra, R.; Walsh, R. In Rappoport, Z., Apeloig, Y., Eds. *The Chemistry of Organic*

          Silicon Compounds; Wiley: New York, 1998; Vol. 2. Part 1, p 153.

(35)   Leroy, G.; Temsamani, D. R.; Wilante, C. *THEOCHEM* **1994**, *306*, 21.

(36)   Metrangolo, P.; Resnati, G. In Atwood, J. L.; Steed, J. W., Eds. *Encyclopedia of*

          Supramolecular Chemistry; Marcel Dekker: New York 2004, 628.

(37)   Tumanskii, B.; Pine, P.; Apeloig, Y.; Hill, N. J.; West, R. *J. Am. Chem. Soc.* **2002**, *124*,

          7786.

(38)   Kira, M.; Ishima, T.; Iwamoto, T.; Ichinohe, M. *J. Am. Chem. Soc.* **2001**, *123*, 1676.

(39)   The free energy barrier for **Me-D** + **A** → **Me-T** is lower than the free energy barrier for

          Me-D + BrCH$_3$ → **Br-P2** (9.6 versus 11.1 kcal/mol) but the free energy of reaction is

          less spontaneous (5.9 versus –14.5 kcal/mol). The free energy barrier for **Me-D** + **A** →

          Me-T is higher than the free energy barrier for **Me-D** + ICH$_3$ → **I-P2** (9.6 versus 8.1

          kcal/mol) and the free energy of reaction is less spontaneous (5.9 versus –11.2 kcal/mol).

(40)   (a) Carpenter, B. K. In Moss, R. A.; Platz, M. S.; Jones, M., Jr. Eds. *Reactive ntermediate*

          Chemistry; Wiley-Interscience: New York, 2004, p 925. (b) Carpenter, B. K. *Angew.*

          Chem. Int. Ed. **1998**, *37*, 3340. (c) Nummela, J. A.; Carpenter, B. K. *J. Am. Chem. Soc.*

2002, *124*, 8512. (d) Carpenter, B. K. *J. Am. Chem. Soc.* **1995**, *117*, 6336. (e) Carpenter,

B. K. *Acc. Chem. Res.* **1992**, *25*, 520.

CHAPTER 5

COMPUTATIONAL STUDY OF CARBON ATOM (^{3}P and ^{1}D) REACTION WITH CH_2O; THEORETICAL EVALUATION OF $^1B_1$ METHYLENE PRODUCTION BY C (^{1}D)

5.1 Introduction

The chemistry of atomic carbon is central to the mechanistic and quantitative understanding of organic chemistry in that it is the ultimate case of a low-valent carbon-centered reactive intermediate that exhibits a thermodynamic drive to form a tetravalent carbon. However it is very difficult to achieve a complete understanding of C atom reactions because the reaction of C atom produces other reactive intermediates, such as carbenes, which can react to form more stable products. Hence, the experimental studies of the mechanisms of C atom reactions has been often limited, and complementary computational studies have been utilized successfully.[1]

Most reactions of C atoms are usually highly exothermic because of the extremely high heat of formation of the C atom. The ground state atomic carbon is triplet (^{3}P) with a heat of formation of ΔH_f^o=171 kcal/mol. The first and second excited states are singlet states, ^{1}D with ΔH_f^o=201 kcal/mol and ^{1}S with ΔH_f^o=233 kcal/mol, respectively.[1,2] Many of the C atom reactions involve the ^{1}D state, and this species brings an additional 30 kcal/mol of energy to its reaction. Therefore the products from C atom reactions contain a great deal of excess energy. When the initial product of a C atom reaction is another reactive intermediate such as a carbene, then very interesting reactivity can be observed due to the high exothermicity.[1,3]

When C atoms react with unsaturated hydrocarbons, abstraction of hydrogen, insertion

125

into a C-H bond, or π addition occurs.[1,4-8] In analogy with carbenes,[9] atomic carbon reacts with

alkenes by double-bond addition to give cyclopropylidenes which undergo the ring opening to

allenes. In the case of carbonyl compounds, the singlet ^{1}D state C atom can react in a similar

fashion: carbon atom addition to the C=O double bond followed by ring opening to give a

$$\begin{array}{c} R \\ \diagdown \\ R' \end{array} \!\!=\!\! O \;+\; C \;\longrightarrow\; \begin{array}{c} \ddot{C} \\ R \diagup \!\!\!\triangle\!\!\! \diagdown \\ R' \quad O \end{array} \;\longrightarrow\; \begin{array}{c} R \\ \diagdown \\ R' \end{array} \!\!=\!\! C \!\!=\!\! O \;\longrightarrow\; \begin{array}{c} R \\ \diagdown \\ R' \end{array} \!\! C\!\!:\; +\; CO \qquad (1)$$
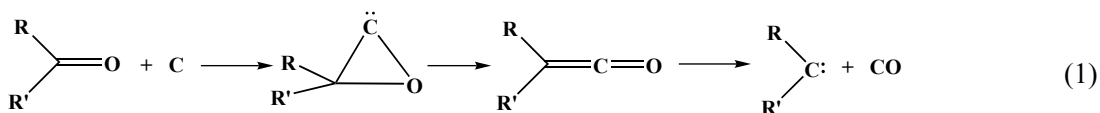
ketene as shown in eq. (1). There is also possibility of end-on attack via a lone pair of electrons

on oxygen forming a ylide-like species (R_2C-O-C). However no compelling evidence for the

end-on intermediate has been reported.[10] Although a ketene is the global minimum on the

potential energy surfaces, no ketene has been isolated. However, the existence of an intermediate

ketene was confirmed by the formation of pentanoic acid by the reaction with H_2O in the process

of the reaction of arc-generated carbon with butanal.[10] All observed products of the reaction of

arc-generated carbon with carbonyl compounds came from the carbenes which formed from

deoxygenation of the carbonyl compounds. Although C=C double bond cleavage in ketene is

highly endothermic, this reaction is still feasible because of the high exothermicity of the initial

reaction.

Now, it is well established that the deoxygenation occurs in the reaction of C (^{1}D) atoms

with ketones and aldehydes.[1,10-16] Furthermore, it has been suggested that singlet excited-state

(^{1}B$_1$) carbenes form in the C (^{1}D) atom deoxygenation of formaldehyde[13] and cyclopentanone.[16]

The C atom deoxygenation of formaldehyde was reported in 1983 by Shevlin, where the

generated carbene was allowed to react with (Z)-2-butene. By assessing the stereochemistry of

the product mixture, the formation of CH$_2$ (^{1}B$_1$) was suggested.[13] However, the excited singlet

carbene in this deoxygenation process was not observed, and it is still not clear how they can

form in this process.

126

Numerous studies on electronic states, photodissociation paths, and oxirene rearrangement of CH_2CO have been reported. [17-23] However, comprehensive studies of the potential energy surface are rare. Hereupon, we report the computational study of ground state (^3P) and first excited state (^1D) of the C atom reaction with formaldehyde. Both the triplet and singlet potential energy surfaces are constructed at the MCQDPT2//CASSCF level. The carbene-producing channels are discussed.

5.2 Computational Details

The Gaussian03 program[24] was used for the hybrid density functional PBE1PBE[25] calculations, while the GAMESS program[26] was used for Complete Active Space SCF (CASSCF),[27] and MCQDPT2[28] calculations. Geometry optimizations for minima and transition states were carried out at the (U)PBE1PBE/6-311++G(3df,p) (DFT) and CASSCF(14,13)/6-311+G(2d,p) (CAS) levels. At the DFT level, harmonic vibrational analysis was performed and the minima and transition states were characterized. Thermodynamic correction terms, zero-point vibrational energies (ZPC), heat capacity corrections and entropies were obtained at the DFT level. Transition vectors of transition states were visualized and animated by the MOLDEN program[29] and if necessary, IRC calculations were carried out to connect the transition state to the corresponding minima.

For CASSCF geometry optimization, a (14,13) active space (14 electrons in 13 orbitals) was chosen from the full (16,14) valence active space of CH_2CO. To maintain a consistent active space we included all valence electrons except for an oxygen lone pair that lies lowest in energy. For the product fragments we considered the same orbitals so that the total active space was maintained as in CH_2CO. For example, a (6,6) active space was used for CH_2 and a (8,7) active space was used for CO.

At each stationary point at the CAS level, single-point energy calculations were carried

out at the MCQDPT2/6-311+G(2d,p) (MCPT) level. Since the (14,13) active space calculations

at the MCPT level are very challenging in terms of computing resources and computing cost, a

(12,11) active space was used, where one low-lying C-H bonding orbital and its antibonding

orbital were excluded. The active space of product fragments was chosen in the same way as at

the CAS level (a (4,4) active space for CH_2 and a (8,7) active space for CO). The potential

energy surfaces were constructed at the MCPT level with zero-point energy correction, heat

capacity correction and free energy correction calculated at the DFT level. The singlet and triplet

surfaces are considered separately and possible singlet-triplet crossings are not considered in this

study. Further wavefunction analysis was carried out with CASSCF wavefunctions to examine

correlations between the reaction intermediates and the products. We will use a notation scheme

with a boldface "**S**" for singlets and "**T**" for triplets followed by one number for minima and two

numbers or one number and a character for transition states. Thus, **S12** is the singlet transition

state between **S1** and **S2** and **T5p** is the transition state between **T5** and products.

5.3 Result and Discussion

The structural isomers of CH_2CO in the singlet and triplet states at the DFT and CAS

level are given in Figures 1 and 2. The calculated electronic energies and thermodynamic

correction terms and spin-squared values are listed in Table 1. Numerous theoretical calculations

on electronic states and photodissociation paths of CH_2CO have been reported.[17-23] The obtained

geometric parameters in this study are in good agreement with those available in the literature[17-23]

which are not given in the Figures 1 and 2 for the clarification. The optimized geometries of **S2**

(${}^1A_1$), **S4** (${}^1A_1$), **T2** (${}^3A''$), and **T2p** (${}^3A''$) optimized at DFT and CAS levels show good agreement

with previous studies by East,[19(b)] Schaefer[18(b),23(a)] and Nemes.[19(c)] The C-C bond of **S2** is shorter

than a normal single-bond distance due to the electron delocalization over the C-C-O π bonding

system. On the triplet surface, **T2** is the lowest-energy structure with a normal C-C single bond

128

Table 1.   Calculated electronic energies (a.u.) at DFT, CAS and MCPT level along with ZPC (kcal/mol), H_{corr} (kcal/mol), entropy (S) (cal·K^{-1}mol^{-1}), spin squared value ($<S^2>$), reference weight of dominant configuration (c_i^2), and electronic states.

	ZPC	H_{corr}	S	$<S^2>$	c_i^2	State	DFT	CAS	MCPT
C (^{3}P)	0.0	1.5	35.6	2.00		^{3}P	-37.80321	-37.70299	-37.76948
C (^{1}D)	0.0	1.5	33.4	1.01		^{1}D	-37.78825	-37.64525	-37.71821
C (^{1}S)	0.0	1.5	33.4	0.00		^{1}S	-37.73128	-37.60755	-37.67319
CO	3.2	5.3	47.2	0.00		$^1\Sigma$	-113.22500	-112.90363	-113.09712
CH$_2$O	16.8	19.2	52.2	0.00		^{1}A$_1$	-114.41299	-114.03723	-114.25908
CH$_2$ (^{3}B$_1$)	10.9	13.3	46.6	2.01	0.97	^{3}B$_1$	-39.11334	-38.96922	-39.04985
CH$_2$ (^{1}A$_1$)	10.5	12.8	45.2	0.00	0.92	^{1}A$_1$	-39.08598	-38.95214	-39.02520
CH$_2$ (^{1}B$_1$)	10.8	13.2	45.0	0.79	0.48	^{1}B$_1$	-39.09191	-38.90222	-38.99299
CH$_2$ (c^{1}A$_1$)^a	10.6	13.0	42.0		0.49	^{1}A$_1$		-38.85490	-38.95163
CH	4.1	6.2	42.3	0.75	0.49	$^2\Pi$	-38.43636	-38.31836	-38.38820
HCO	8.3	10.6	53.6	0.75	0.94	^{2}A'	-113.76579	-113.40462	-113.62390
S1	20.4	22.9	58.3	0.00	0.90	^{1}A'	-152.37894	-151.86774	-152.15813
S2	19.9	22.7	57.7	0.00	0.90	^{1}A'	-152.48037	-151.96541	-152.26748
S2"	19.6	22.3	59.5	1.02	0.40	^{1}A"	-152.39395	-151.86882	-152.17944
S3	17.6	20.9	63.4	0.66	0.86	^{1}A	-152.35063	-151.83978	-152.13372
S4	18.7	21.6	59.5	0.00	0.88	^{1}A$_1$	-152.35261	-151.82673	-152.14154
S5	20.1	23.1	59.0	0.00	0.90	^{1}A'	-152.42108	-151.90656	-152.21047
S6^b	18.6	21.6	60.9	0.00		^{1}A'	-152.31492		
S7^c	17.5	20.4	60.1	1.01	0.46	^{1}A"	-152.29307	-151.78186	-152.06890
S12	17.5	20.3	60.7	0.55	0.12	^{1}A'	-152.34339	-151.83313	-152.13225
S13	16.8	19.3	58.6	0.00	0.88	^{1}A	-152.29228	-151.76894	-152.07458
S15	15.8	18.4	58.8	0.00	0.89	^{1}A	-152.26001	-151.74954	-152.03200
S2"2"	18.0	20.6	57.1	1.02	0.31	^{1}A$_2$	-152.36022	-151.83125	-152.14786
S23	17.2	20.0	59.8	0.64	0.89	^{1}A'	-152.35024	-151.83890	-152.13009
S25	16.0	19.1	60.6	0.00	0.83	^{1}A'	-152.32577	-151.79756	-152.12003
S34	18.4	21.0	59.2	0.00	0.84	^{1}A	-152.35046	-151.84396	-152.13308
S66	18.4	21.2	57.9	0.00	0.87	^{1}A$_1$	-152.31127	-151.79402	-152.09282
S6p^b	17.5	20.6	61.4	0.00		^{1}A'	-152.31396		
S7p^c	15.9	19.2	64.0	1.00	0.41	^{1}A'	-152.27168	-151.73690	-152.05775
Sr7^c	17.2	20.2	59.7	1.01	0.37	^{1}A$_2$	-152.26256	-151.73876	-152.03349
S$_{ci}$^{d}	19.6	22.3	59.5					-151.84950	-152.16824
T1	20.1	22.7	60.6	2.01	0.91	^{3}A"	-152.29621	-151.76542	-152.08428
T2	19.1	21.9	62.2	2.01	0.16	^{3}A"	-152.39793	-151.87873	-152.18798
T3	19.6	22.2	59.2	2.01	0.91	^{3}B	-152.32432	-151.78806	-152.10321
T4	19.0	21.7	61.9	2.03	0.90	^{3}A"	-152.36686	-151.85794	-152.15574
T5	17.9	21.0	63.5	2.01	0.06	^{3}A"	-152.29754	-151.79195	-152.07875
T6	17.1	20.1	63.5	2.01	0.90	^{3}A"	-152.24274	-151.74531	-152.02303
T7	19.0	21.8	62.0	2.01	0.84	^{3}A"	-152.31178	-151.77501	-152.10270
T12	19.6	22.0	60.5	2.13	0.03	^{3}A"	-152.26744	-151.73773	-152.06021
T13	16.3	18.9	60.8	2.01	0.89	^{3}A	-152.24172	-151.70055	-152.02343
T15	17.1	20.1	65.2	2.01	0.80	^{3}A"	-152.25769	-151.75622	-152.04323
T22	18.0	20.7	61.7	2.01	0.91	^{3}A'	-152.38049	-151.86024	-152.17257
T24	15.4	18.2	61.7	2.02	0.87	^{3}A	-152.30075	-151.77008	-152.08981
T27	15.0	17.7	61.4	2.02	0.51	^{3}A"	-152.23731	-151.71033	-152.02596
T2p	15.0	18.9	72.0	2.01	0.84	^{3}A"	-152.33779	-151.84749	-152.14815

-continue-

	ZPC	H_{corr}	S	$<S^2>$	c_i^2	State	DFT	CAS	MCPT
T34	17.6	20.2	61.2	2.01	0.74	^3A	-152.28006	-151.75141	-152.07125
T56	15.0	17.7	61.5	2.02	0.84	$^3A"$	-152.22171	-151.69994	-152.02092
T5p	15.5	18.9	66.4	2.02	0.64	$^3A"$	-152.28497	-151.77296	-152.08015
T22'	18.0	20.7	59.2	2.01	0.91	$^3A_2$	-152.36096	-151.82249	-152.14431
T55	17.3	20.2	61.3	2.02	0.64	$^3A_2$	-152.26537	-151.71934	-152.03924

(a)   Thermodynamic correction data are obtained at the CAS level, because at the DFT level we could not locate the excited c^1A_1 minimum.

(b)   At the CAS level, stationary points could not be found, and at the DFT level, after the zero-point energy correction, the relative energy order of the minimum (**S6**) and the transition state (**S6p**) becomes reversed. Therefore, **S6** will follow the dissociation path without barrier.

(c)   These three structures have an imaginary frequency that corresponds to out-of-plane distortion. We located a minimum or transition states with C_1 symmetry at the DFT level. However their distortion from planarity is very small and after the zero-point energy correction the structures with C_s symmetry are lower than C_1 structures. Hence, at the CAS level geometry optimization we used C_s symmetry.

(d)   Single point energy calculations at the CAS and MCPT levels are performed for both $^1A'$ and $^1A"$ state on the geometry obtained from conical intersection optimization at the CAS(6,6)/6-311+G(2d,p) level.   The energies reported are averaged for both states. Thermodynamic corrections of **S2"** are used for the enthalpies and free energy the correction.
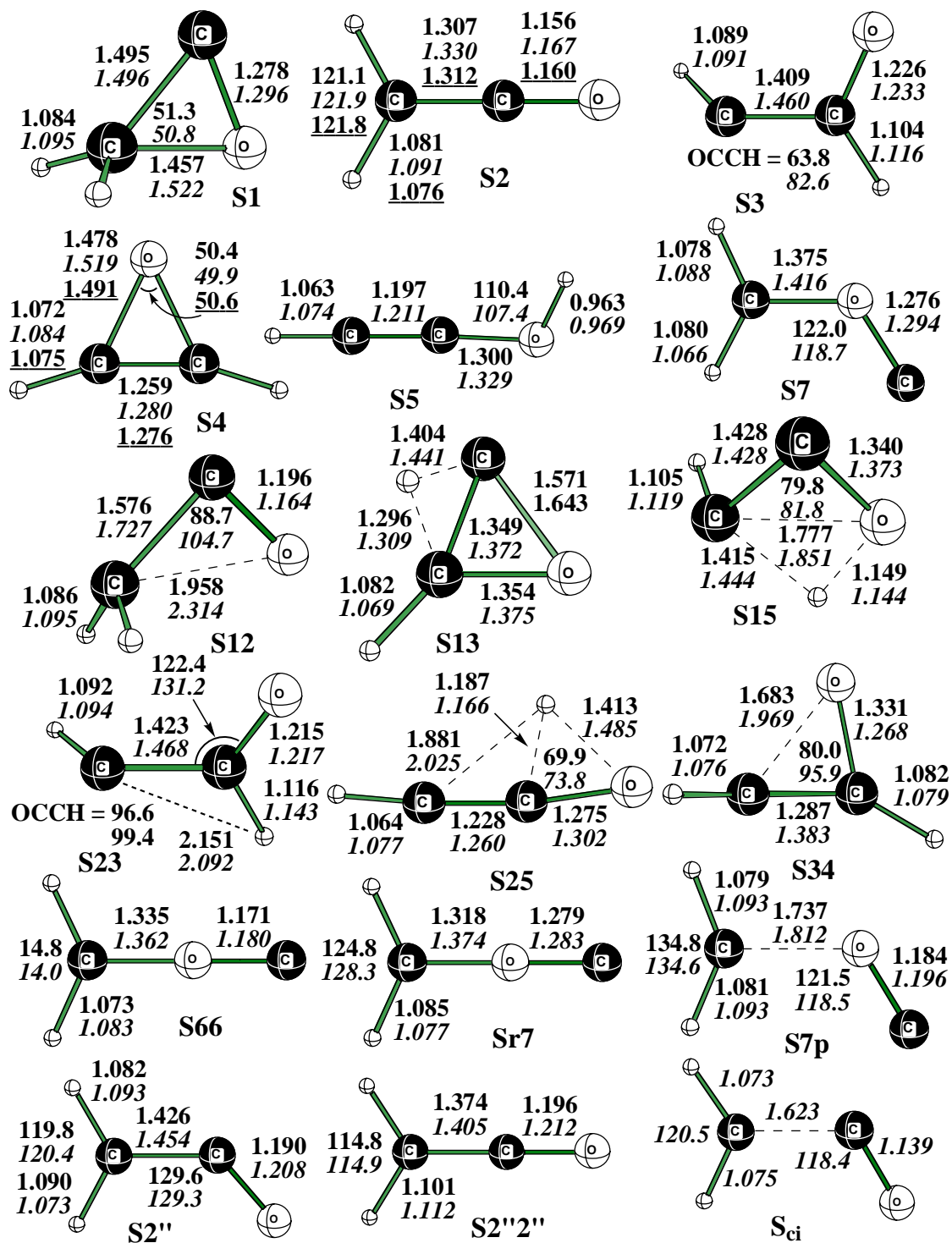
Figure 1. Optimized geometries of singlet species at the DFT and CAS (in *italic*) level. Literature values (underlined) for **S2** are from reference 19(b) and for **S4** are from 23(a). **S$_{ci}$** geometry obtained at the CASSCF(6,6)/6-311+G(2d,p) level. Bond lengths are in Å and angles are in degrees.
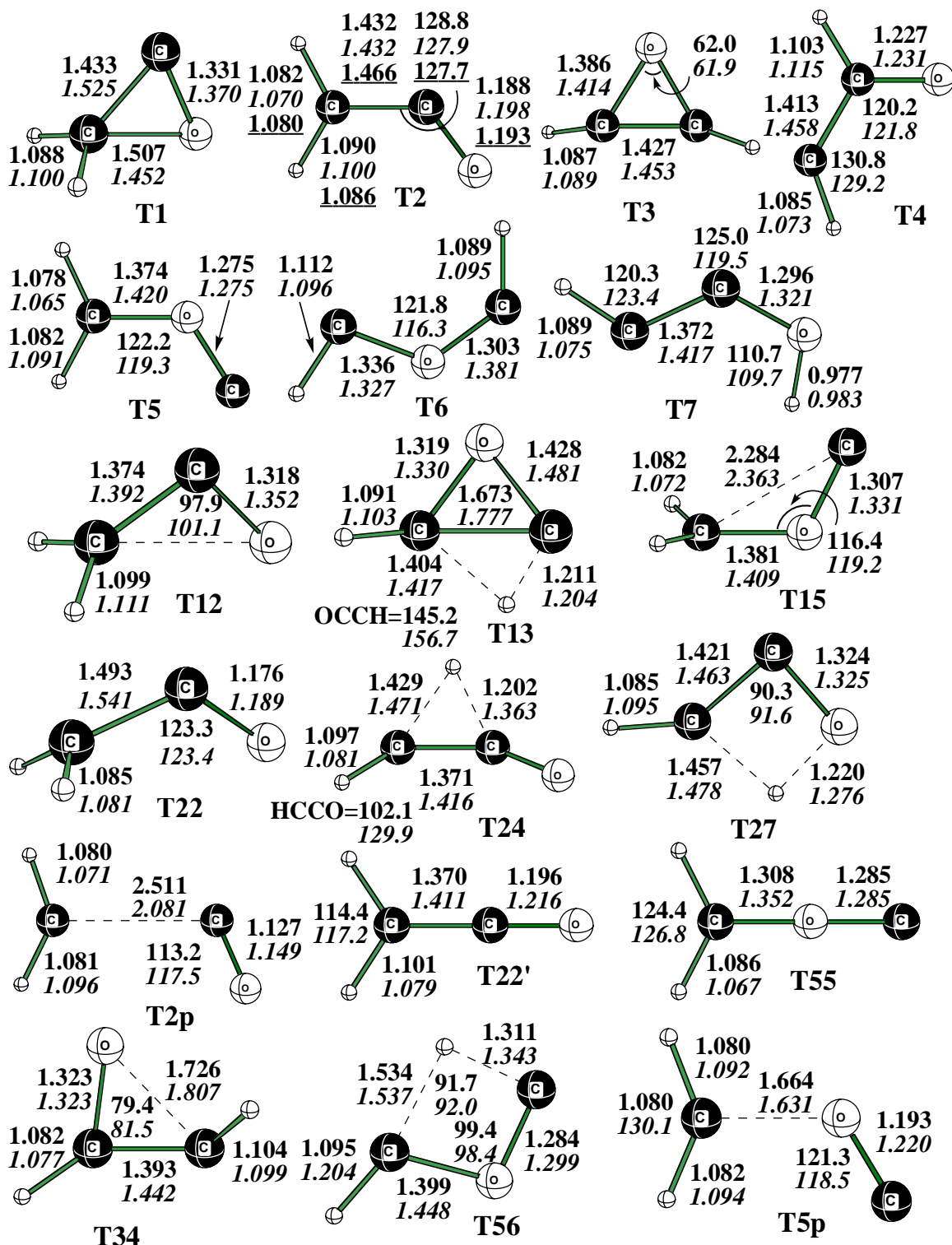
131

Figure 2. Optimized geometries of triplet species at DFT and CAS (in *italic*) level. Literature values (underlined) for **T2** from reference 18(b). Bond lengths are in Å and angles are in degrees.

distance of (1.432 Å) and C-C-O angle of 127.9°. The C-O bond length of **T2** is about 0.03 Å

longer than in **S2**.   However, the C-H distances are very similar in **S2** and **T2**. **T22'** ($^3A_2$) has the

same atomic arrangement as **S1** and its C-O and C-C bond lengths are longer than those of **S1**

(0.049 and 0.081 Å longer, respectively). The C atom end-on attack structures, **S66** ($^1A_1$), **Sr7**

($^1A_2$) and **T55** ($^3A_2$), are found to be transition states with one imaginary frequency. All of them

display distinct structural characteristics. **S66** has the shortest C-O bond length (1.180 Å) and

longest C-C bond (1.362 Å). The structures of **Sr7** and **T55** are rather similar to each other. The

C-O bond lengths are almost the same (1.283 and 1.285 Å) and the C-C distances are only 0.022

Å different. **Sr7** and **S7p** have two imaginary frequencies and **S7** has one imaginary frequency.

Distortion along the smaller imaginary frequency, which is out-of-plane bending, leads to real

transition states or minimum with lower-symmetry at the DFT level. However, the stationary

points are close to the higher-symmetry species and, after zero-point correction, the higher-

symmetry species are lower in energy. We consider the **Sr7**, **S7** and **S7p** as stationary points and

we used the higher-symmetry structure for geometry optimization at the CAS level. The singlet

and triplet carbene (**S3** and **T4**) intermediates are also characterized. Structurally both are similar

except that **S3** has an OCCH dihedral angle of 82.6° but **T4** is planar. On the singlet surface,

several carbenes similar to **S3** are identified at the DFT level; among them we chose one with

lowest free energy and closest structure to the CAS level geometry for thermodynamic correction.

We optimized the four lowest energy states of methylene structures ($^3B_1$, $^1A_1$, $^1B_1$ and c^1A_1); the

structures obtained in this study are shown in Figure 3, and they are close to those reported in the

literature.[31]

The calculated relative energies are given in Table 2 and 3 for triplet and singlet species,

respectively and the schematic potential energy surfaces for each state are given in Figure 4 and

5. In the discussion, we will use ΔG_{298} which is the MCPT electronic energy with ZPC, heat

capacity (C_p) and entropy (ΔS) corrections at the DFT level. On the triplet potential energy
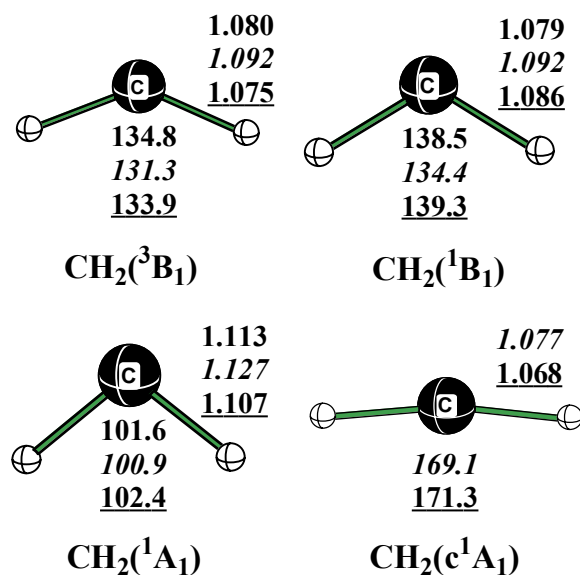
133

Figure 3. Optimized geometries of the four lowest energy states of methylenes at the DFT and CAS (in *italic*) level. Literature values (underlined) are from reference 31. Bond lengths are in Å and angles are in degrees.

surface (Figure 4), **T2** is the lowest-energy species, -91.1 kcal/mol relative to $CH_2O + C$ (^3P). The addition of a C atom to the C-O π bond initially forms a triplet oxiranylidene **T1** without barrier. **T1** can undergo H_2C-O bond breaking, C-C bond breaking or hydrogen transfer to oxygen or carbon. All four pathways were examined, but no transition state for hydrogen transfer to oxygen was found. The lowest-energy pathway leads to **T2** on the triplet surface, with a free energy barrier of 14.5 kcal/mol and a reaction free energy of -66.3 kcal/mol. There must be a valley-ridge inflection (VRI) points or a bifurcation along the H_2C-O bond breaking (**T1**→**T2**),[33] because a C-O stretching mode cannot directly connect two minima and a rotation or bending mode is also necessary. At a VRI point along the angle CCO opening coordinate, C-O stretching vector becomes zero and a rotational mode around C-C bond becomes negative. Therefore, there are two saddle points connected along the C_s symmetry coordinate. **T12** is one with C-O stretching vector and **T22'** is the other with bending mode as transition vector. **T2** can undergo two interconversions: a rotation around the C-C bond (8.5 kcal/mol free energy barrier)

Table 2.   Relative enthalpies (kcal/mol) of C_2H_2O triplet isomers at 0K (ΔH_0), 298K (ΔH_{298}) and free energies at 298K (ΔG_{298}) calculated at the MCPT level with thermodynamic corrections at the DFT level.

| | ΔH_0 | ΔH_{298} | | ΔG_{298} |
		Calc.	Exp.[a]	
CH_2O+C (^3P)	0.0	0.0	0.0	0.0
CH_2O+C (^1D)	32.2	32.2	29.1[b]	32.8
CH_2O+C (^1S)	60.4	60.4	61.9[b]	61.1
$CO+CH_2$ ($^3B_1$)	-77.0	-76.4	-76.7[c]	-78.2
$CO+CH_2$ ($^1A_1$)	-61.9	-61.3	-67.7[c]	-62.7
$CO+CH_2$ ($^1B_1$)	-41.4	-41.4	-43.8[c]	-42.3
$CO+CH_2$ (c^1A_1)	-18.8	-17.4	-16.6[c]	-15.8
CH+HCO	5.9	6.5	8.2[d]	4.1
T1	-31.6	-32.9		-24.8
T2	-97.7	-98.7		-91.1
T3	-44.0	-45.3		-36.8
T4	-77.5	-78.7		-71.0
T5	-30.4	-31.2		-23.9
T6	5.3	4.5		11.8
T7	-44.3	-45.4		-37.7
T12	-17.0	-18.5		-10.2
T13	2.8	1.4		9.5
T15	-8.9	-9.7		-3.0
T22	-89.1	-90.3		-82.6
T24	-39.8	-40.9		-33.1
T27	-0.1	-1.3		6.5
T2p	-76.8	-76.8		-72.1
T34	-25.9	-27.2		-19.3
T56	3.1	1.9		9.7
T5p	-33.6	-34.1		-27.7
T22'	-71.4	-72.6		-64.1
T55	-5.5	-6.5		0.8

a. ΔH_{298} values relative to $CH_2O + C$ (^3P).

b.   For C (^3P), 171.3 kcal/mol and for CH_2O, -27.7 kcal/mol, are used as ΔH_{298}. Relative energies are calculated by using the data from ref. 2.

c.   93.3 kcal/mol was used as ΔH_{298} of methylene from ref. 32. The energy separations $^3B_1$-$^1A_1$: 9.0 kcal/mol (ref. 31(c)), $^3B_1$-$^1B_1$: 32.9 kcal/mol (ref. 31(d)) and $^3B_1$-c^1A_1: 60.1 kcal/mol (ref. 31(b)) were used.

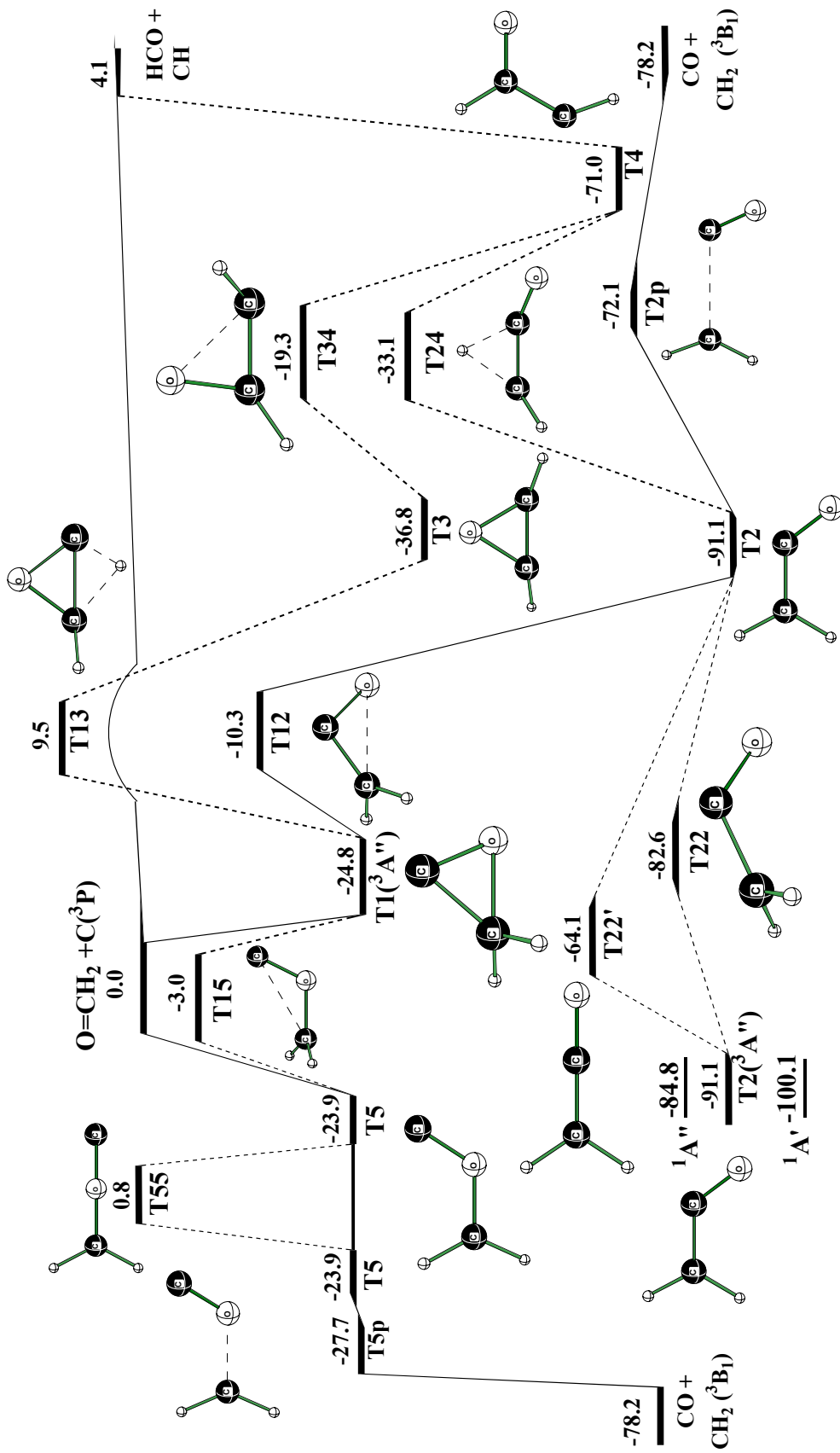d.   As ΔH_{298} of CHO, 10.0 kcal/mol was used from ref. 32.

Figure 4. Triplet potential energy surface constructed from ΔG_{298} at the MCPT level. Relative energies are given in kcal/mol.

and an inversion via a linear C-C-O structure (**T22'** 37.0 kcal/mol barrier). It is also possible to transfer a hydrogen atom to the other carbon to form a triplet carbene (**T4**), though the free energy barrier is quite unfavorable (58.0 kcal/mol). The fate of this carbene is not clear. Breaking the C-C bond to yield CH and HCO is very unfavorable (75.1 kcal/mol free energy barrier). Therefore, **T4** most likely will undergo reactions with reactants (i.e. CH_2O). The pathway we are most interested in for **T2** is breaking the C-C bond to form carbon monoxide and triplet state methylene (CH_2 $^3B_1$) with a 19.0 kcal/mol free energy barrier (reverse barrier: 6.1 kcal/mol). This result is in good agreement with those of Allen.[18b] The C-C bond dissociation energy (ΔH_0=20.7 kcal/mol, Table 2) is also close to calculated value (18.6 kcal/mol) and proposed value 22.3 kcal/mol.[18b] The enthalpy barrier (forward: 20.9 kcal/mol, reverse: 0.2 kcal/mol) is somewhat lower than their estimation (forward: 25-27 kcal/mol, reverse: 3-4 kcal/mol), and therefore, the reaction of triplet state methylene with CO to form **T2** has a very low barrier.

In **T1**, hydrogen transfer to another carbon is not likely to occur due to a 34.3 kcal/mol free energy barrier. If C atoms have large amount of kinetic energy, then this barrier can be overcome. This will lead to formation of triplet oxirene, **T3** which can transform into a carbene **T4**. If C-C bond cleavage occurs in **T1**, the bent H_2C-O-C (**T5**) isomer will form. However, **T5** will dissociate into CO and CH_2 ($^3B_1$) without a free energy barrier. **T5p** was located as a transition state at both the DFT and CAS levels, but at the MCPT level the energy is lower than **T5**. Clearly, dynamic electron correlation is important and may be underestimated at the DFT and CAS levels. A transition state **T55** was located along the interconversion of **T5**. It can also form from direct attack of a C (^3P) atom on oxygen, which is slightly uphill from reactants.

It is known experimentally that the triplet C atom abstracts hydrogen from organic compounds.[1] On this PES no evidence of the hydrogen abstraction was found. We investigated direct hydrogen abstraction pathways, but no transition state was located. The hydrogen

137

abstraction from formaldehyde by C (^{3}P) is endothermic (4.1 kcal/mol free energy) and proceeds

without reverse barrier. The hydrogen abstractions from formaldehyde by halogen atoms have

been studied theoretically; these studies revealed that this reaction is almost barrierless (at the

CCSD(T)//B3LYP/6-311++G(d,p))[34(a)] or has a very low barrier (for F, 8.5 kcal/mol and for Cl,

4.4 kcal/mol at the MP2/aug-cc-PVDZ level).[34(b)] Therefore, the C-H bond in formaldehyde is

weak and can be abstracted easily by radicals. In this context, the hydrogen abstraction from

formaldehyde by C (^{3}P) proceeds without reverse barrier. In addition, as shown in equation (2),

no electron rearrangement is necessary to produce two ground state products in this reaction.

Therefore, this reaction occurs without reverse barrier.

(2)
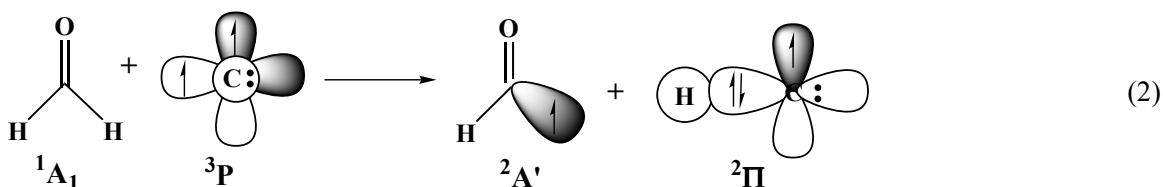
On the singlet PES (Figure 5), the most probable reaction between C (^{1}D) with

formaldehyde is also π addition to form **S1**. This reaction is 103.0 kcal/mol exothermic, and **S1**

will have enough energy to undergo interconversion. The lowest energy reaction path is to form

ground state **S2** (^{1}A$_1$) via **S12** over a 12.9 kcal/mol barrier by breaking the H$_2$C-O bond. Another

possible path is hydrogen transfer to either carbon or oxygen. Although hydrogen transfer to

carbon has a high barrier (48.7 kcal/mol), the system has enough energy to overcome it to yield

singlet carbene **S3**. The singlet carbene, **S3** can easily covert into **S2** (2.5 kcal/mol barrier). It

can also make a C-O bond to form a oxirene, **S4**. A number of studies has been performed on the

singlet oxirene rearrangement mechanism (Wolff rearrangement),[23] and we found that this result

agrees previous results very well. **S3** is lower in energy at the CAS level than **S4** but their energy

order is reversed at the MCPT level. Similar disagreement has been shown at the MP2 level,

where the singlet carbene (**S3**) is not a minimum.[23b,e] The truncation after second-order term in

perturbation theory is responsible for poor description of the singlet carbene, **S3**. In **S1**, hydrogen

Table 3.   Relative enthalpies (kcal/mol) of C_2H_2O singlet isomers at 0K (ΔH_0), 298K (ΔH_{298})
and free energies at 298K (ΔG_{298}) calculated at the MCPT level with
thermodynamic corrections at the DFT level.

	ΔH_0	ΔH_{298}		ΔG_{298}
		Calc.	Exp.[a]	
$CH_2O+C\ (^3P)$	0.0	0.0	0.0	0.0
$CH_2O+C\ (^1D)$	32.2	32.2	29.1	32.8
$CH_2O+C\ (^1S)$	60.4	60.4	61.9	61.1
$CO+CH_2\ (^3B_1)$	-77.0	-76.4	-76.7	-78.2
$CO+CH_2\ (^1A_1)$	-61.9	-61.3	-67.7	-62.7
$CO+CH_2\ (^1B_1)$	-41.4	-41.4	-43.8	-42.3
$CO+CH_2\ (c^1A_1)$	-18.8	-17.4	-16.6	-15.8
$CH\ (^2\Pi)+HCO\ (^2A')$	5.9	6.5	8.2	4.1
S1	-77.7	-79.0		-70.2
S2	-146.8	-147.9	-155.0^b	-138.9
S2"	-91.9	-93.0		-84.6
S3	-65.1	-65.7		-58.5
S4	-69.0	-69.9		-61.5
S5	-110.8	-111.7		-103.1
S7	-25.7	-26.8		-18.5
S12	-64.4	-65.4		-57.3
S13	-28.9	-30.2		-21.5
S15	-3.1	-4.4		4.2
S23	-63.2	-64.4		-56.0
S25	-58.2	-58.9		-50.8
S34	-64.0	-65.2		-56.7
S66	-38.7	-39.8		-30.8
S7p	-19.1	-19.7		-12.6
Sr7	-2.7	-3.5		4.9
S$_{ci}$	-84.8	-86.0		-77.5

a. ΔH_{298} values relative to $CH_2O + C\ (^3P)$. For the detailed explanation see Table 2.

b.   11.4 kcal/mol from ref. 32 was used for ΔH_{298} of ground state ketene (**S2**) to calculate
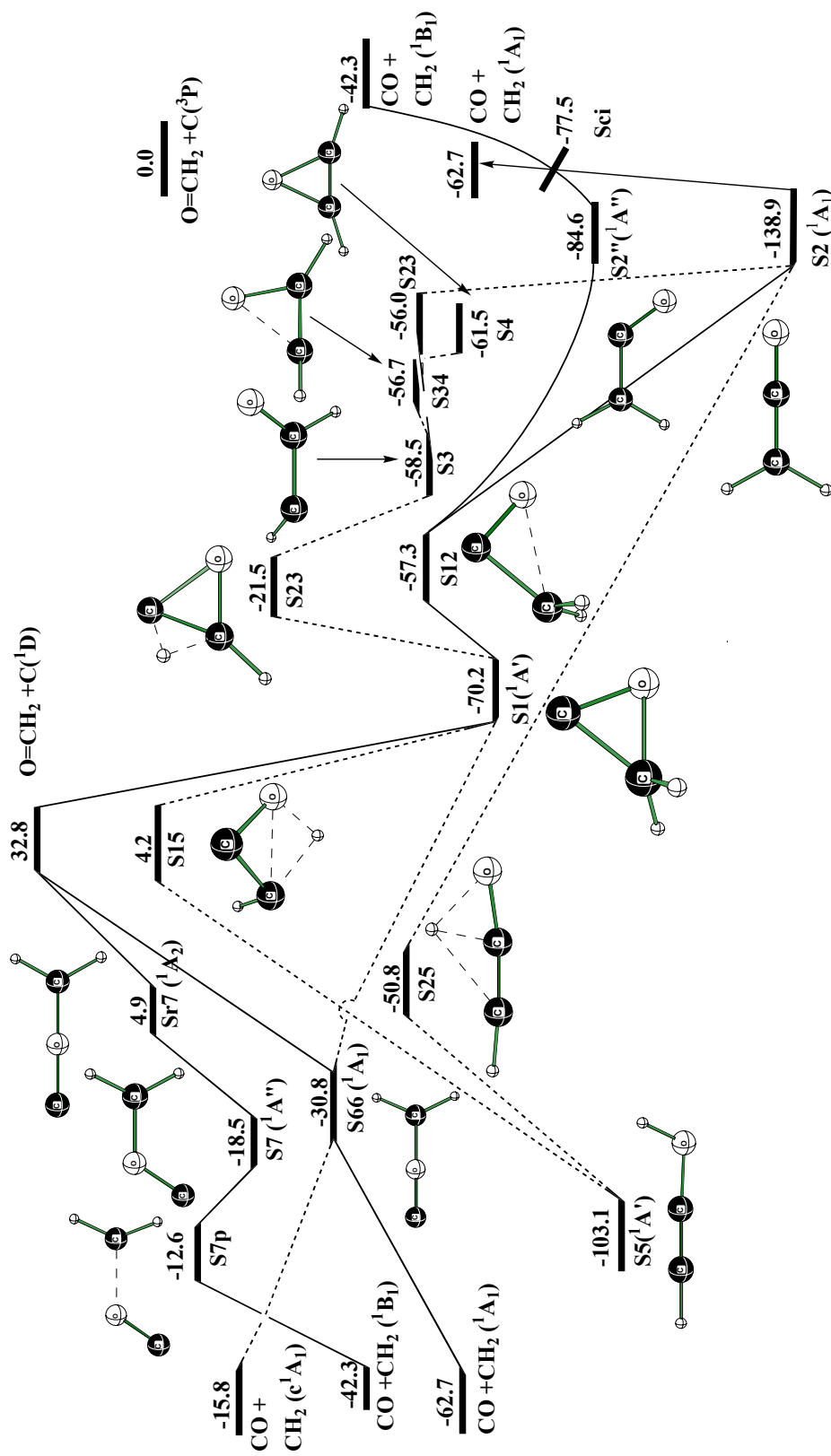relative enthalpy.

Figure 5. Singlet potential energy surface constructed from ΔG_{298} at MCPT level. Relative energies are given in kcal/mol.

140

transfer to oxygen to form **S5** has a high barrier (66.0 kcal/mol). **S5** has a co-linear H-C-C-O

arrangement and it is the second lowest species on the potential energy surface. A transition state

between **S5** and **S2** has been located. Surprisingly, a hydrogen atom jumps from oxygen to the

other end carbon directly to go from **S5** to **S2**. Thermodynamic advantage of making a C-O

double bond might be the driving force of this process.

In **S1**, the C-C bond breaking process is complicated. Opening the C-C bond will lead to

S66 ($^1A_1$) which has an out-of-plane bending mode of two hydrogen atoms as a transition vector.

At the DFT level, a minimum and a transition state were located, but after the zero-point energy

correction, the transition state has a lower energy than the minimum. At the CAS level, no

minimum was located and distortion along the transition vector led directly to dissociation of

ketene to CO + CH_2 ($^1A_1$). Another way to form **S66** is direct addition of the C atom to oxygen.

This pathway has no barrier and will lead to the $^1A_1$ carbene only.

On the singlet PES, two pathways which lead to formation of the $^1B_1$ carbene were found.

One starts from direct attack of C (^1D) on oxygen to form **Sr7** ($^1A_2$) which is a transition state of

interconversion of **S7** ($^1A''$). **S7** dissociates via a 5.9 kcal/mol free energy barrier to give CO and

singlet excited carbene ($^1B_1$). These three are biradical species on the $^1A''$ surface. In Figure 6

two singly occupied orbitals of **S7p** transition state are shown. The a'' orbital is located on the

CH_2 carbon and the other a' orbital is the H_2C-O antibonding orbital and directly correlates with

(a) a'' orbital   **(b) a' orbital**
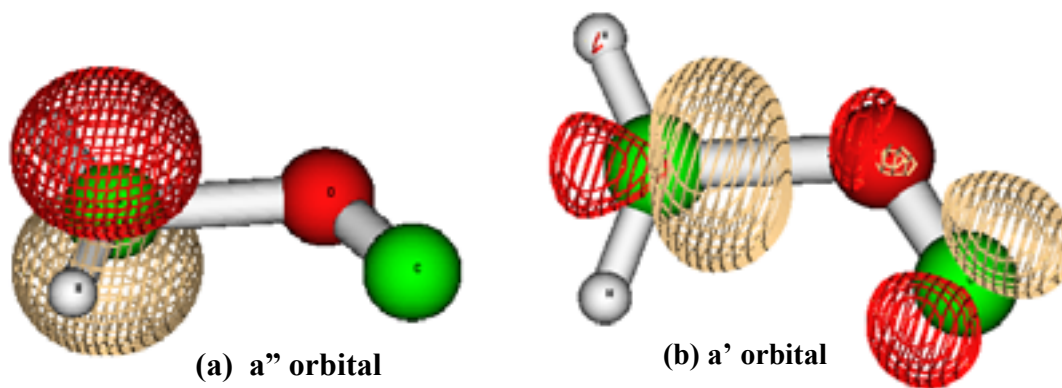
Figure 6.   Two singly occupied orbitals of **S7p**. (a) a'' orbital, (b) a' orbital.

the excited singlet carbene ($^1B_1$) plus CO. Now, the question is if it is possible for $^1B_1$ methylene to form on the $^1A''$ surface. The ^1D state has five microstates which will split into $2A_1 + A_2 + B_1 + B_2$ in C_{2v} symmetry, and into $3A' + 2A''$ in C_s symmetry. When the ^1D carbon attacks the formaldehyde oxygen atom, the microstates will split into $3\,^1A'$ and $2\,^1A''$ states and the ratio between a' and a'' will be 3 to 2. Therefore, it is possible to form the $^1A''$ state. Next question to consider is if this deoxygenation process is faster than intersystem crossing (ISC). The quantitative answer to this question is not possible from this study, but it can be answered qualitatively. The dissociation will proceed very quickly, since it has only a 5.9 kcal/mol barrier, and the system will have about 50 kcal/mol extra energy at **S7**. The ISC occurs along the seam of two potential energy surfaces if the spin-orbit coupling is large enough and geometries are similar to each other.[35-39] Generally speaking, the spin-orbit coupling is large in heavier elements, but in the first-row elements the spin-orbit coupling is very small.[36,38] However, triplet-singlet intersystem crossing rate was derived as 4×10^{12} s^{-1}.[40] In fact, the energy gap between $^1A''$ surface and $^3A''$ surface is small (**S7-T5**: 5.4 kca/mol) and so, the excited singlet species can undergo ISC to the lower $^3A''$ surface. Therefore, the formation of $^1B_1$ state methylene via $^1A''$ surface (**Sr7-S7-S7p**) may not be significant.

The other pathway involves low lying $^1A''$ surface. The transition state, **S12** is highly multireferential (reference weight of the dominant configuration is 0.12) and biradical. The H_2C-O stretching mode will lead to global minimum **S2**, while rotation around C-C bond will lead to form $^1A''$ state **S2''**. The **S2''** is lowest in free energy on the $^1A''$ surface and will lead to form $^1B_1$ methylene. However, at CAS level the analytical hessian calculation is too demanding and it is not certain that if the **S12** is a first order or second order saddle point. If it is a first order saddle point as at the DFT level, then there must be an VRI or conical intersection between **S12** and **S2''**. The existence of a conical intersection was reported by Yoshimine.[22(a)] Therefore we tried to locate the conical intersection around this part of PES at the CAS(6,6)/6-311+G(2d,p)

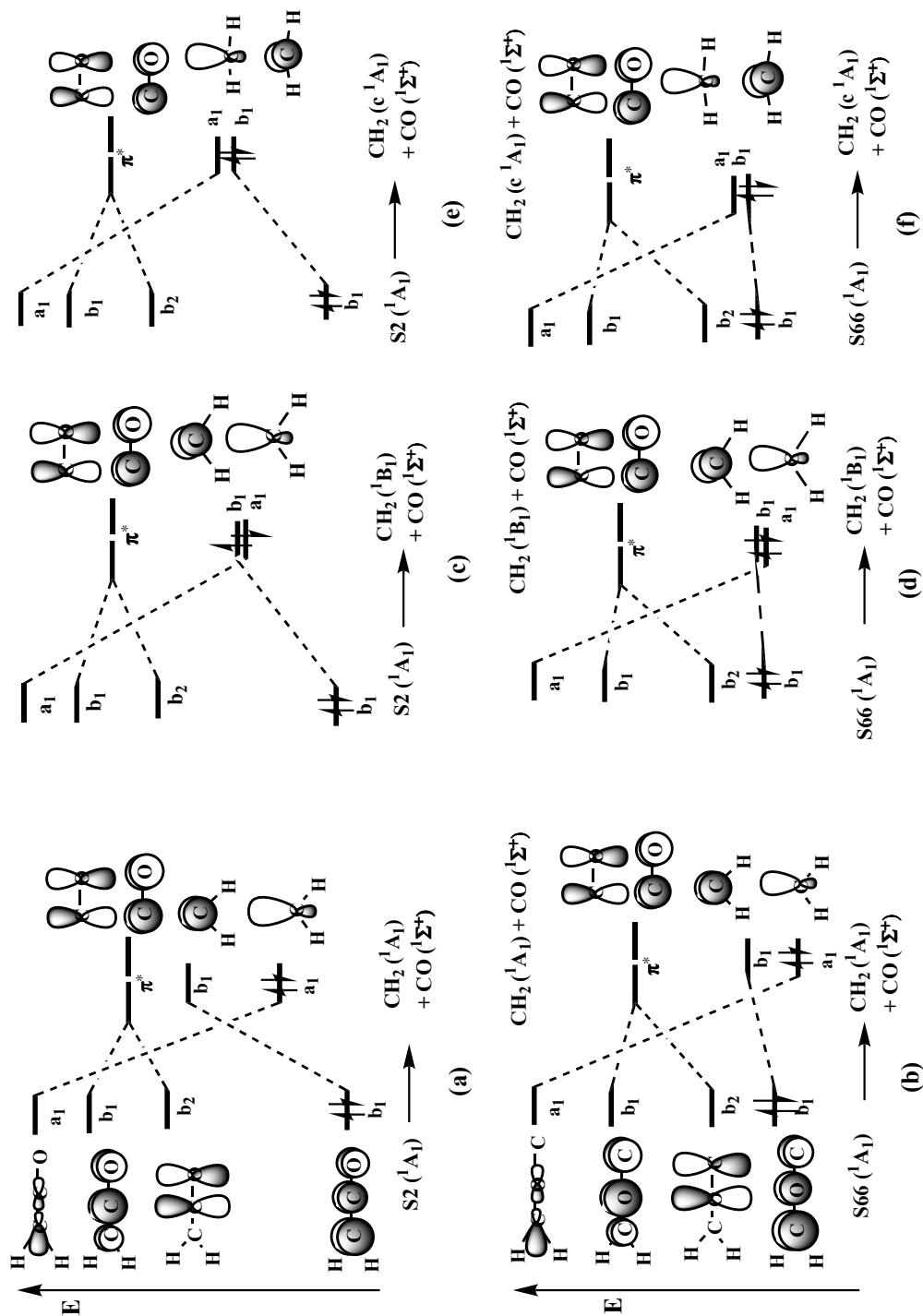Figure 7.   Orbital crossing diagram for the singlet methylene producing reactions from **S2** and **S66**.
(a) **S2** $\rightarrow$ CO + CH$_2$ (^{1}A$_1$), (b) **S66** $\rightarrow$ CO + CH$_2$ (^{1}A$_1$), (c) **S2** $\rightarrow$ CO + CH$_2$ (^{1}B$_1$),
(d) **S66** $\rightarrow$ CO + CH$_2$ (^{1}B$_1$), (e) **S2** $\rightarrow$ CO + CH$_2$ (c^{1}A$_1$), (f) **S66** $\rightarrow$ CO + CH$_2$ (c^{1}A$_1$)

143

level, but we could not obtain desirable results. Depending upon the active space size, the PES shape is very different. That is why we cannot locate the right conical intersection. The second possibility that **S12** might be a second order saddle point was also examined by optimizing the geometry at the CAS(12,11)/6-311+G(2d,p) level and by numerical vibrational analysis. The transition state, **S12** found to be second order saddle point with two distinct imaginary frequencies (a': 319.8i, a'': 163.7i) at this level. Therefore, at **S12** the PES will split into ^{1}A' and ^{1}A'' surfaces. The **S2''** can dissociate to give ^{1}B$_1$ methylene plus CO by breaking the C-C bond without reverse barrier. Along the C-C bond breaking pathway a conical intersection **S$_{ci}$** between ^{1}A' and ^{1}A'' surface was found. The conical intersection is lower in free energy by 14.8 kcal/mol than the CH$_2$ (^{1}A$_1$) plus CO. This conical intersection can be a radiationless decay channel of ^{1}A'' state ketene, **S2''** or excitation of **S2** to **S2''**. If the bond breaking process of **S2''** is fast enough to pass the conical intersection, then it is possible to form CH$_2$ (^{1}B$_1$) plus CO in accordance with Carpenter's non-statistical dynamic effect.[41]

It is still not clear if the observed products could form from other lower-energy intermediates on the singlet PES. Thus, we examined orbital correlations between ketene with C$_{2v}$ symmetry (**S2** and **S66**) and carbene products (Figure 7) and their valence electron configurations are given in Table 4. Interestingly, neither **S2** nor **S66** directly correlate to the lowest ^{1}A$_1$ state methylene plus CO, but both correlate to the third excited c^{1}A$_1$ state methylene plus CO. As the C-C (C-O) distance becomes longer in **S2 (S66)**, the C-C antibonding orbital (a$_1$) will be stabilized but the occupied b$_1$ orbital will be destabilized due to the loss of π bonding interaction. As shown in Figure 6, to correlate the ^{1}A$_1$ state ketene (**S1** or **S66**) with the ^{1}A$_1$ state methylene plus CO, the orbital crossing between b$_1$ and a$_1$ orbitals is unavoidable. The correlation diagram between the ^{1}A$_1$ state ketene with the ^{1}B$_1$ state methylene plus CO (Figure 6 (c) and (d)) also shows a crossing, but the energies of two orbitals (a$_1$ and b$_1$) are so close each other as to be pseudo-degenerate. The ^{1}A$_1$ state ketene isomers, **S2** and **S66**, correlate with the

144

Table 4.   Important valence electron configurations of four lowest electronic state methylene and four singlet species obtained at CAS level

	Configuration[a]	$|c_i|$ [b]
CH$_2$ (^{3}B$_1$)	$a_1^2 b_2^2 a_1 b_1$	0.98
CH$_2$ (^{1}A$_1$)	$a_1^2 b_2^2 a_1^2$	0.97
	$a_1^2 b_2^2 b_1^2$	0.18
CH$_2$ (^{1}B$_1$)	$a_1^2 b_2^2 a_1 \overline{b_1}$	0.70
	$a_1^2 b_2^2 \overline{a_1} b_1$	0.70
CH$_2$ (c^{1}A$_1$)	$a_1^2 b_2^2 b_1^2$	0.73
	$a_1^2 b_2^2 a_1^2$	0.67
S2 (^{1}A$_1$)	$a_1^2 a_1^2 b_2^2 a_1^2 a_1^2 b_1^2 b_2^2 b_1^2$	0.95
	$a_1^2 a_1^2 b_2^2 a_1^2 a_1^2 b_1^2 b_1^2 b_2^2$	0.12
	$a_1^2 a_1^2 b_2^2 a_1^2 a_1^2 b_1^2 b_2^2 b_1^2$	0.10
S2" (^{1}A")	$a'^2 a'^2 a'^2 a'^2 a'^2 a''^2 a'^2 \overline{a''} a'$	0.63
	$a'^2 a'^2 a'^2 a'^2 a'^2 a''^2 a'^2 \overline{a''} a'$	0.63
	$a'^2 a'^2 a'^2 a'^2 a'^2 a''^2 a'^2 \overline{a'} a''$	0.17
	$a'^2 a'^2 a'^2 a'^2 a'^2 a''^2 a'^2 a' \overline{a''}$	0.17
S66 (^{1}A$_1$)	$a_1^2 a_1^2 b_2^2 a_1^2 b_1^2 a_1^2 b_2^2 b_1^2$	0.93
	$a_1^2 a_1^2 b_2^2 a_1^2 b_1^2 a_1^2 b_2^2 b_2^2$	0.15
Sr7 (^{1}A$_2$)	$a_1^2 a_1^2 a_1^2 b_2^2 b_1^2 a_1^2 b_2^2 b_1 \overline{b_2}$	0.61
	$a_1^2 a_1^2 a_1^2 b_2^2 b_1^2 a_1^2 b_2^2 \overline{b_1} b_2$	0.61
	$a_1^2 a_1^2 a_1^2 b_2^2 b_1^2 a_1^2 b_2^2 b_1 \overline{b_2}$	0.29
	$a_1^2 a_1^2 a_1^2 b_2^2 b_1^2 a_1^2 b_2^2 \overline{b_1} b_2$	0.29
S7p (^{1}A")	$a'^2 a'^2 a'^2 a''^2 a'^2 a'^2 a'^2 \overline{a'} a''$	0.64
	$a'^2 a'^2 a'^2 a''^2 a'^2 a'^2 a'^2 \overline{a'} a''$	0.64
	$a'^2 a'^2 a'^2 a''^2 a'^2 a'^2 a'^2 \overline{a'} a''$	0.17
	$a'^2 a'^2 a'^2 a''^2 a'^2 a'^2 a'^2 \overline{a'} a''$	0.17

a.   For clarification core electron configurations are omitted. Singly occupied β orbitals are designated with bar over the orbital designation.

b.   Absolute value of coefficient of each configuration.

excited c^{1}A$_1$ methylene state plus CO without orbital crossing (Figure 6 (e) and (f)). In this case, there must be a transition state in the dissociation pathway of ketene along the C-C bond elongation.

Finally, the reaction enthalpies and free energies of oxygen abstraction reactions by

C atom obtained in this study are summarized in Table 5. Our results are in very good agreement with experimental results. The reaction, $C + CH_2O \rightarrow CO + CH_2$ is highly exothermic and the reaction free energy of excited singlet $^1B_1$ carbene producing reaction is calculated to be −75.1 kcal/mol.

Table 5.   Reaction enthalpies at 0K (ΔH_0) and 298K (ΔH_{298}) and free energies at 298K (ΔG_{298}) at MCPT level (in kcal/mol)

Reactants	Products	ΔH_0	ΔH_{298}		ΔG_{298}
		Calc.	Calc.	Exp.[a]	Calc.
C (^3P) + CH_2O	**T2** (^3A")	-97.7	-98.7	-101.2[b]	-91.1
C (^1D) + CH_2O	**S2** ($^1A_1$)	-179.0	-180.1	-184.1	-171.7
T2 (^3A")	$CO + CH_2$ ($^3B_1$)	20.7	22.3	24.5[b]	12.9
S2 ($^1A_1$)	$CO + CH_2$ ($^1A_1$)	84.9	86.6	87.3	76.2
S2 ($^1A_1$)	$CO + CH_2$ ($^1B_1$)	105.4	107.1	112.2	97.0
S2 ($^1A_1$)	$CO + CH_2$ (c^1A_1)	128.0	130.5	138.4	123.1
C (^3P) + CH_2O	$CO + CH_2$ ($^3B_1$)	-77.0	-76.4	-76.7	-78.2
C (^1D) + CH_2O	$CO + CH_2$ ($^1A_1$)	-94.1	-93.5	-96.8	-95.5
C (^1D) + CH_2O	$CO + CH_2$ ($^1B_1$)	-73.6	-73.0	-72.9	-75.1
C (^1D) + CH_2O	$CO + CH_2$ (c^1A_1)	-51.1	-49.6	-45.7	-48.6

a. ΔH_{298} values are given. For detailed information about the experimental values, see Table 2.

b.   **T2** energies are calculated from **S2** ($^1A_1$) - **T 2** (^3A") separation 54.8 kcal/mol (T_0) reported by Schaefer in ref. 20 with heat capacity correction obtained in this study.

5.4 Conclusion

The reactions of triplet (^3P) and singlet (^1D) atomic carbon with formaldehyde were studied computationally. **S2** ($^1A_1$) is the global minimum on the entire ketene (CH_2CO) potential energy surface. On the triplet PES, a C atom adds to the C-O double bond to form cyclic **T1** which undergoes intramolecular rearrangement. The bent H_2C-C-O linkage isomer (**T2**) is lowest on the triplet PES, and it dissociates to give CO and the ground state methylene (CH_2 $^3B_1$). On

the triplet surface, linear C-C-O or C-O-C isomers (**T22'** and **T55**) were found to be transition

states for the interconversion of corresponding bent isomers (**T2** and **T5**). Hydrogen abstraction

from formaldehyde by C (^{3}P) is nonspontaneous (4.1 kcal/mol) and can proceed without a reverse

free energy barrier. On the singlet surface, the C (^{1}D) addition to the C-O double bond also

occurs without barrier to form **S1** with a free energy change of -103.0 kcal/mol. **S1** can also

undergo various isomerization reactions to form the global minimum **S2**, or **S5** which is the

second lowest species on both potential energy surfaces. On both surface intermediate carbenes

are identified (**T4** and **S3**). The triplet carbene (**T4**) may survive long enough to react with

another reagents in the reaction mixture but singlet carbene (**S3**) probably will not.

The possible pathways to form excited singlet methylene (^{1}B$_1$) were found. One is along

the reaction path **Sr7** (^{1}A$_2$)-**S7** (^{1}A")-**S7p** (^{1}A") which leads to the ^{1}B$_1$ carbene directly. The other

possible pathway is by way of **S2"** which is lowest on the ^{1}A" surface, if the C-C bond

dissociation in **S2"** occurs very fast. Interestingly the ground state **S2** (^{1}A$_1$) correlates better with

the third excited singlet state methylene (c^{1}A$_1$) than the first excited singlet methylene (^{1}A$_1$).

However, this level of theory is not enough to explain the dynamic behavior of molecule, and we

are preparing ab initio molecular dynamics calculations on the basis of our constructed potential

energy surfaces.

5.5 References

(1)   Shevlin, P. B. In *Reactive Intermediate Chemistry*, Moss, R. A.; Platz, M. S.; Jones, M., Jr. Ed. Wiley: New York, 2004, p 463.

(2)   Chase, M. W., Jr. *NIST-JANAF Thermochemical Tables, 4th Ed.; J. Phys. Chem. Ref. Data* **1998**, Monograph 9.

(3)   (a) Wolf, A. P. *Adv. Phys. Org. Chem.* **1964**, *2*, 201, (b) Wolfgang, R. *Prog. React. Kinet.* **1965**, *3*, 97 (c) Wolfgang, R. *Adv. High Temp. Chem.* **1971**, *4*, 43, (d) Skell, P. S.; Havel, J.; McGlinchey, M. J. *Acc. Chem. Res.* **1973**, *6*, 97 (e) Shevlin, P. B. In *Reactive Intermediates*, Vol. I, Abramovitch, R. A. Ed. Plenum Press: New York, 1980, p 1.

(4)   Kaiser, R. I.; Mebel, A. M. *Int. Rev. Phys. Chem.* **2002**, *21*, 207.

(5)   Loison, J.-C.; Bergeat, A. *Phys. Chem. Chem. Phys.* **2004**, *6*, 5396.

(6)   Clary, D. C.; Buonomo, E.; Sims, I. R.; Smith, I. W. M.; Geppert, W. D.; Naulin, C.; Costes, M.; Cartechini, L.; Casavecchia, P. *J. Phys. Chem. A* **2002**, *106*, 5541.

(7)   Su, H.-F.; Kaiser, R. I.; Chang, A. H. H. *J. Chem. Phys.* **2005**, *122*, 074320.

(8)   Geise, C. M.; Hadad, C. M.; Zheng, F.; Shevlin, P. B. *J. Am. Chem. Soc.* **2002**, *124*, 355.

(9)   *Carbene Chemistry: From Fleeting Intermediates to Powerful Reagents*, Bertrand, G. Ed. Marcel Dekker: New York, 2002.

(10)   Dewar, M. J. S.; Nelson, D. J.; Shevlin, P. B.; Biesiada, K. *J. Am. Chem. Soc.* **1981**, *103*, 2802.

(11)   Skell, P. S.; Plonka, J. H. *J. Am. Chem. Soc.* **1970**, *92*, 836.

(12)   Skell, P. S.; Plonka, J. H. *J. Am. Chem. Soc.* **1970**, *92*, 2160.

(13)   Ahmed, S. N.; Shevlin, P. B. *J. Am. Chem. Soc.* **1983**, *105*, 6488.

(14)   Fox, J. M.; Gillen, J. E.; Jones, K. G. H.; Jones, M., Jr.; Shevlin, P. B.; Armstrong, B.; Sztyrbicka, R. *Tetrahedron Lett.* **1992**, *33*, 5021.

(15)   Armstrong B. M.; McKee, M. L.; Shevlin, P. B. *J. Am. Chem. Soc.* **1995**, *117*, 3685.

(16)   Xu, G.; Chang, T.-M.; Zhou, J.; McKee, M. L.; Shevlin, P. B. *J. Am. Chem. Soc.* **1999**, *121*, 7150.

(17)   (a) Basch, H. *Theor. Chim. Acta* **1973**, *28*, 151. (b) Pendergast, P.; Fink, W. H. *J. Am. Chem. Soc.* **1976**, *98*, 648.

(18)   (a) Yamabe, S.; Morokuma, K. *J. Am. Chem. Soc.* **1978**, *100*, 7551. (b) Allen, W. D.; Schaefer, H. F. III, *J. Chem. Phys.* **1988**, *89*, 329. (c) Klippenstein S. J.; East, A. L. L.; Allen, W. D. *J. Chem. Phys.* **1996**, *102*, 8506.

(19)   (a) Allen, W. D.; Schaefer, H. F. III, *J. Chem. Phys.* **1986**, *84*, 2212. (b) East, A. L. L.; Allen, W. D.; Klippenstein S. J. *J. Chem. Phys.* **1995**, *102*, 8506. (c) Szalay, P. G.; Császár, A. G.; Nemes, L. *J. Chem. Phys.* **1996**, *105*, 1034.

(20)   Bouma, W. J.; Nobes, R. H.; Radom, L.; Woodward, C. E. *J. Org. Chem.* **1982**, *47*, 1869.

(21)   Takeshita, K. *J. Chem. Phys.* **1992**, *96*, 1199.

(22)   (a) Yoshimine, M. *J. Chem. Phys.* **1989**, *90*, 378. (b) Maier, G.; Reisenauer, H. P.; Cibulka, M. *Angew. Chem. Int. Ed.* **1999**, *38*, 105. (c) Delamere, C.; Jakins, C.; Lewars, E. *THEOCHEM*, **2002**, *593*, 79.

(23)   (a) Scott, A. P.; Nobes, R. H.; Schaefer, H. F., III; Radom, L. *J. Am. Chem. Soc.* **1994**, *116*, 10159. (b) Delamere, C.; Jakins, C.; Lewars, E. *Can. J. Chem.* **2002**, *80*, 94. (c) Wilson, P. J.; Tozer, D. J. *Chem. Phys. Lett.* **2002**, *352*, 540. (d) Mawhinney, R. C. Goddard, J. D. *THEOCHEM*, **2003**, *629*, 263. (e) Girard, Y.; Chaquin, P. *J. Phys. Chem. A* **2003**, *107*, 10462. (f) Zeller, K.-P.; Blocher, A.; Haiss, P. *Mini-Rev. Org. Chem.* **2004**, *1*, 291.

(24)   *Gaussian03, (Revision B.4)*, Frisch, M. J.; Trucks, G. W.; Schlegel, H. B.; Scuseria, G. E.; Robb, M. A.; Cheeseman, J. R.; Montgomery, J. A. Jr.; Vreven, T.; Kudin, K. N.; Burant, J. C.; Millam, J. M.; Iyengar, S. S.; Tomasi, J.; Barone, V.; Mennucci, B.; Cossi, M.; Scalmani, G.; Rega, N.; Petersson, G. A.; Nakatsuji, H.; Hada, M.; Ehara, M.; Toyota, K.;

Fukuda, R.; Hasegawa, J.; Ishida, M.; Nakajima, T.; Honda, Y.; Kitao, O.; Nakai, H.;

Klene, M.; Li, X.; Knox, J. E.; Hratchian, H. P.; Cross, J. B.; Adamo, C.; Jaramillo, J.;

Gomperts, R.; Stratmann, R. E.; Yazyev, O.; Austin, A. J.; Cammi, R.; Pomelli, C.;

Ochterski, J. W.; Ayala, P. Y.; Morokuma, K.; Voth, G. A.; Salvador, P.; Dannenberg, J. J.;

Zakrzewski, V. G.; Dapprich, S.; Daniels, A. D.; Strain, M. C.; Farkas, O.; Malick, D. K.;

Rabuck, A. D.; Raghavachari, K.; Foresman, J. B.; Ortiz, J. V.; Cui, Q.; Baboul, A. G.;

Clifford, S.; Cioslowski, J.; Stefanov, B. B.; Liu, G.; Liashenko, A.; Piskorz, P.;

Komaromi, I.; Martin, R. L.; Fox, D. J.; Keith, T.; Al-Laham, M. A.; Peng, C. Y.;

Nanayakkara, A.; Challacombe, M.; Gill, P. M. W.; Johnson, B.; Chen, W.; Wong, M. W.;

Gonzalez, C.; and Pople, J. A. Gaussian, Inc., Pittsburgh PA, 2003.

(25)   (a) Perdew, J. P.; Burke, K.; Ernzerhof, M. *Phys. Rev. Lett.* **1996**, *77*, 3865. (b) Perdew, J.

P.; Burke, K.; Ernzerhof, M. *Phys. Rev. Lett.* **1997**, *78*, 1396.

(26)   *GAMESS,* Schmidt, M. W.; Baldridge, K. K.; Boatz, J. A.; Elbert, S. T.; Gordon, M. S.;

Jensen, J. J.; Koseki, S.; Matsunaga, N.; Nguyen, K. A.; Su, S.; Windus, T. L.; Dupuis,

M.; Montgomery, J. A. *J. Comput. Chem.* **1993**, *14*, 1347.

(27)   (a) Roos, B. O. "The complete active space self-consistent field method and its

applications in electronic structure calculations" In: Lawley, K. P., Ed. *Advances in

Chemical Physics; Ab Initio Methods in Quantum Chemistry-II*; John Wiley & Sons:

Chichester, UK, 1987. (b) Schmidt, M. W.; Gordon, M. S. *Ann. Rev. Phys. Chem.* **1998**,

49, 233.

(28)   (a) Nakano, H. *J. Chem. Phys.* **1993**, *99*, 7983. (b) Nakano, H. *Chem. Phys. Lett.* **1993**,

207, 372.

(29)   *MOLDEN,* Schaftenaar, G.; Noordik, J. H. *J. Comput.-Aided Mol. Design*, **2000**, *14*, 123.

(30)   Duncan, J. L.; Munro, B. *J. Mol. Struct.* **1987**, *161*, 311.

(31)   (a) Petek, H.; Nesbitt, D. J.; Darwin, D. C.; Ogilby, P. R.; Moore, C. B. *J. Chem. Phys.*

1989, *91*, 6566. (b) Yamaguchi, Y. Sherrill, C. D.; Schaefer, H. F. III, *J. Phys. Chem.*

1996, *100*, 7911. (c) Yamaguchi, Y.; Schaefer, H. F. III, *Chem. Phys*. **1997**, *225*, 23. (d)

Jensen, P.; Bunker, P. R. *J. Chem. Phys.* **1998**, *89*, 1327. (e) Szabados, Á.; Hargittai, M. *J.*

Phys. Chem. A **2003**, *107*, 4314. (f) Kalemos, A.; Dunning, T. H., Jr.; Mavridis, A.;

Harrison, J. F. *Can. J. Chem.* **2004**, *82*, 684.

(32)   Computational Chemistry Comparison and Benchmark Database (CCCBDB) at

http://srdata.nist.gov/cccbdb/default.htm.

(33)   (a) Castaño, O.; Frutos, L.-M.; Palmeiroi, R.; Notario, R.; Andrés, J. L.; Gomperts, R.;

Blancafort, L.; Robb, M. A. *Angew. Chem. Int. Ed.* **2000**, *39*, 2095. (b) Basilevsky, M. V.

Chem. Phys. **1977**, *24*, 81. (c) Valtazanos, P.; Ruedenberg, K. *Theor. Chem. Acta* **1986**,

69, 281.

(34)   (a) Dong, Feng; Qu, Zhengwang,; Zhang, Q.; Kong, F. *Chem. Phys. Lett.* **2003**, *371*, 29.

(b) Beukes, J. A.; D'Anna, B.; Nielsen, C. J. *Phys. Chem. Chem. Phys.* **2000**, *2*, 4049.

(35)   Turo, N. J.; Cha, Y.; Gould, I. R. *J. Am. Chem. Soc.* **1987**, *209*, 2101.

(36)   Hoffmann, M. R.; Schatz, G. C. *J. Chem. Phys.* **2000**, *113*, 9456.

(37)   Biczók, L.; Bérces, T.; Yatsuhashi, T.; Tachibana, H.; Inoue, H. *Phys. Chem. Chem. Phys.*

2001, *3*, 980.

(38)   Byeon, C. C.; Mekerns, Sun, S.; Gray, G. M. *Appl. Phys. Lett.* **2004**, *84*, 5174.

(39)   Blitz, M. A.; Pilling, M. J.; Seakins, P. W. *Phys. Chem. Chem. Phys.* **2001**, *3*, 2241.

(40)   Nguyen, T. L.; Dils, B.; Carl, S. A.; Vereecken, L.; Peeters, J. *J. Phys. Chem. A.* **2005**,

109, ASAP

(41)   (a) Carpenter, B. K. *Angew. Chem., Int. Ed.* **1998**, *37*, 3340. (b) Carpenter, B. K. In Moss,

R. A.; Platz, M. S.; Jones, M., Jr. Eds. *Reactive Intermediate Chemistry*; Wiley-

Interscience: New York, 2004, p 925. (c) Carpenter, B. K. *Annu. Rev. Phys. Chem.* **2005**,

56, 57.